

On the
conductivity of
PEDOT:PSS
thin films

Alexandre Mantovani Nardes
Eindhoven, 2007

On the conductivity of PEDOT:PSS thin films

PROEFSCHRIFT

ter verkrijging van de graad van doctor aan de Technische Universiteit Eindhoven, op gezag van de Rector Magnificus, prof.dr.ir. C.J. van Duijn, voor een commissie aangewezen door het College voor Promoties in het openbaar te verdedigen op dinsdag 18 december 2007 om 14.00 uur

door

Alexandre Mantovani Nardes

geboren te São Paulo, Brazilië

Dit proefschrift is goedgekeurd door de promotoren:

prof.dr.ir. R.A.J. Janssen
en
prof.dr. A.M. de Andrade

Copromotor:
dr.ir. M. Kemerink

The work described in this thesis has been carried out at the Electronic System Engineering Department of the Polytechnic School of the University of São Paulo, São Paulo, Brazil and at the department of Applied Physics of the Eindhoven University of Technology, in Eindhoven, the Netherlands. In Brazil, this research was financially supported by FAPESP (# 02/11941-6), “*The State of Sao Paulo Research Foundation*”, whilst in the Netherlands by an European Union program, the Programme Alþan, “*América Latina Bolsas de Alto Nível*” (ID# E03D19439BR) and partially by the Molecular Materials and Nanosystems (M2N) group.

Cover: “Drops of PEDOT:PSS solution” (E. Roeling and A. M. Nardes)

CIP-DATA LIBRARY TECHNISCHE UNIVERSITEIT EINDHOVEN

Nardes, Alexandre Mantovani

On the conductivity of PEDOT:PSS thin films / by Alexandre Mantovani Nardes.
– Eindhoven : Technische Universiteit Eindhoven, 2007. - Proefschrift.

ISBN 978-90-386-1178-5

NUR 926

Trefwoorden: organische elektronica / geleidende polymeren / elektrische geleiding / anisotropie / rastertunnelmicroscopie / atomaire krachtmicroscopie / licht-emitterende diodes / inkapseling / chemische damp depositie
Subject headings: organic electronics / conducting polymers / electrical conductivity / anisotropy / hopping conduction / scanning tunneling microscopy / atomic force microscopy / light-emitting diodes / encapsulation / chemical vapor deposition

“The vocation, it is to have as a work its passion”

*Marie-Henri Beyle
(pen name Stendhal)*

Contents

SUMMARY	I
SAMENVATTING	V
RESUMO	IX
LIST OF FIGURES	XIII
LIST OF TABLES	XVII
LIST OF SYMBOLS, ACRONYMS AND ABBREVIATIONS	XIX
1 INTRODUCTION	1 -
1.1 ORGANIC ELECTRONICS – THE FUTURE IS FLEXIBLE!	- 3 -
1.2 ELECTRONIC PROPERTIES OF CONDUCTING POLYMERS	- 4 -
1.3 POLY(3,4-ETHYLENEDIOXYTHIOPHENE):POLY(STYRENESULFONIC ACID) (PEDOT:PSS).....	- 8 -
1.4 CHARGE TRANSPORT IN DISORDERED MATERIALS	- 9 -
1.5 SCANNING PROBE MICROSCOPY (SPM)	- 12 -
1.6 DEVICE LIFETIME – POLYMER LIGHT-EMITTING DIODES (PLEDs)	- 17 -
1.7 OBJECTIVES AND SCOPE	- 20 -
1.8 REFERENCES AND NOTES	- 22 -
2 BARRIER COATING FOR POLYMER LIGHT-EMITTING DIODES USING CARBON NITRIDE THIN FILMS DEPOSITED AT LOW TEMPERATURE BY PECVD TECHNIQUE	25 -
2.1 INTRODUCTION	- 27 -
2.2 EXPERIMENTAL	- 28 -
2.3 RESULTS AND DISCUSSIONS	- 30 -
2.4 CONCLUSIONS	- 34 -
2.5 REFERENCES	- 35 -
3 MICROSCOPIC UNDERSTANDING OF THE ANISOTROPIC CONDUCTIVITY OF PEDOT:PSS THIN FILMS: A QUALITATIVE STUDY	37 -
3.1 INTRODUCTION	- 39 -
3.2 EXPERIMENTAL	- 40 -
3.3 RESULTS AND DISCUSSIONS	- 42 -
3.3.1 <i>Temperature dependence of the electrical conductivity</i>	- 43 -
3.3.2 <i>Morphology</i>	- 45 -
3.3.3 <i>In-plane anisotropy</i>	- 47 -
3.4 CONCLUSIONS	- 50 -
3.5 REFERENCES AND NOTES	- 51 -
4 ANISOTROPIC HOPPING CONDUCTION IN SPIN-COATED PEDOT:PSS THIN FILMS: A QUANTITATIVE STUDY	53 -
4.1 INTRODUCTION	- 55 -
4.2 EXPERIMENTAL	- 58 -
4.3 RESULTS	- 58 -
4.3.1 <i>Temperature dependence</i>	- 58 -
4.3.2 <i>Electric field dependence</i>	- 60 -
4.3.2.1 Normal direction	- 60 -
4.3.2.2 Lateral direction.....	- 62 -
4.4 DISCUSSION	- 64 -
4.5 CONCLUSIONS	- 67 -
4.6 REFERENCES AND NOTES	- 68 -

5	CONDUCTIVITY AND ENVIRONMENTAL STABILITY OF PEDOT:PSS THIN FILMS TREATED WITH SORBITOL.....	- 71 -
5.1	INTRODUCTION	- 73 -
5.2	EXPERIMENTAL	- 74 -
5.3	RESULTS	- 76 -
5.3.1	<i>Effect of thermal annealing</i>	- 76 -
5.3.2	<i>Effect of humidity</i>	- 79 -
5.3.3	<i>Water uptake</i>	- 82 -
5.3.4	<i>Temperature dependence</i>	- 83 -
5.4	DISCUSSION	- 85 -
5.5	CONCLUSIONS	- 86 -
5.6	REFERENCES AND NOTES	- 87 -
6	SURFACE POTENTIAL OF PEDOT:PSS THIN FILMS STUDIED BY SCANNING KELVIN PROBE MICROSCOPY	- 89 -
6.1	INTRODUCTION	- 91 -
6.2	EXPERIMENTAL	- 92 -
6.3	RESULTS AND DISCUSSION	- 93 -
6.3.1	<i>Conductivity enhancement</i>	- 93 -
6.3.2	<i>Surface potential analysis</i>	- 95 -
6.4	CONCLUSIONS	- 98 -
6.5	REFERENCES AND NOTES	- 99 -
7	A MORPHOLOGICAL MODEL FOR SOLVENT-INDUCED CONDUCTIVITY ENHANCEMENT IN PEDOT:PSS THIN FILMS.....	- 101 -
7.1	INTRODUCTION	- 103 -
7.2	EXPERIMENTAL	- 105 -
7.3	RESULTS	- 106 -
7.3.1	<i>Charge transport</i>	- 106 -
7.3.2	<i>Morphology</i>	- 111 -
7.4	DISCUSSIONS	- 113 -
7.5	CONCLUSIONS	- 115 -
7.6	REFERENCES AND NOTES	- 116 -

APPENDICES:

A.	MODULATED-DIFFERENTIAL SCANNING CALORIMETRY AND DIRECT INSERT PROBE MASS SPECTROMETRY	- 119 -
A1.1	INTRODUCTION: MODULATED-DIFFERENTIAL SCANNING CALORIMETRY (MDSC)	- 121 -
A1.2	EXPERIMENTAL	- 121 -
A1.3	RESULTS AND DISCUSSIONS	- 121 -
A1.4	CONCLUSIONS	- 122 -
A2.1	INTRODUCTION: DIRECT INSERT PROBE MASS SPECTROMETRY (DIP-MS)	- 123 -
A2.2	EXPERIMENTAL	- 123 -
A2.3	RESULTS AND DISCUSSIONS	- 123 -
A2.4	CONCLUSIONS	- 125 -
B.	CURRICULUM VITAE	- 127 -
C.	ACKNOWLEDGMENTS	- 129 -

Summary

Employing the unique mechanical, electronic, and optical properties of the conjugated organic and polymer materials several technological and commercial applications have been developed, such as sensors, memories, solar cells and light-emitting diodes (LEDs). In this respect, the central theme of this thesis is the electrical conductivity and mechanisms of charge transport in PEDOT:PSS, a polymer blend that consists of a conducting poly(3,4-ethylenedioxythiophene) polycation (PEDOT) and a poly(styrenesulfonate) polyanion (PSS). PEDOT:PSS is omnipresent as electrode material in ‘plastic electronics’ applications mentioned above. Although the conductivity of PEDOT:PSS can vary by several orders of magnitude, depending on the method by which it is processed into a thin film, the reason for this behavior is essentially unknown. This thesis describes a detailed study of the anisotropic charge transport of PEDOT:PSS and its correlation with the morphology, the shape, and the dimension of the phase separation between the two components, PEDOT and PSS.

Before addressing the properties of PEDOT:PSS, a new barrier layer is described in Chapter 2 that enhances the lifetime of organic devices. An important degradation mechanism in polymer LEDs is photo-oxidation of the active layer. Hence, isolating the active layer from water and oxygen is crucial to the lifetime. Plasma-enhanced chemical vapor deposition (PECVD) is used to deposit a thin layer of carbon nitride at low deposition temperatures, below 100 °C, on a polymer LED that uses poly[2-methoxy-5-(2'-ethylhexyloxy)-1,4-phenylene vinylene] (MEH-PPV) as active layer. A thin layer of carbon nitride acts as barrier for humidity, but is still sufficiently bendable to be used in flexible polymer LEDs. The characteristics of carbon nitride and MEH-PPV films have been investigated using optical spectroscopy, with particular emphasis on the degradation process of MEH-PPV under illumination. The measurements show that the carbon nitride coating indeed protects the polymer film and diminishes the photo-oxidation considerably. To study the effect of the encapsulation in real devices, polymer LEDs were made and their current-voltage characteristics confirm the enhanced lifetime in the presence of a carbon nitride barrier layer.

However, the target, a lifetime of more than 10,000 hours for commercial applications, was not achieved.

The remaining chapters of this thesis describe the investigations of PEDOT:PSS. PEDOT:PSS is widely used in organic electronics. So far, relatively little attention has, been paid to the mechanisms of charge transport in this material and the correlation of those properties to the morphology. In Chapter 3, scanning probe microscopy (SPM) and macroscopic conductivity measurements are used to obtain a full 3D morphological model that explains, qualitatively, the observed anisotropic conductivity of spin coated PEDOT:PSS thin films. Topographic scanning probe microscopy (STM) and cross-sectional atomic force microscopy images (X-AFM) reveal that the thin film is organized in horizontal layers of flattened PEDOT-rich particles that are separated by quasi-continuous PSS lamella. In the vertical direction, the horizontal PSS insulator lamellas lead to a reduced conductivity and impose nearest-neighbor hopping (nn-H) transport. In the lateral direction, 3D variable-range hopping (3D-VRH) transport takes place between PEDOT-rich clusters which are separated by much thinner barriers, leading to an enhanced conductivity in this direction.

This discussion is extended in Chapter 4, where a quantitative description of the length scales of the predominant transport is obtained. Particularly, it is demonstrated that the hopping process takes place between PEDOT-rich islands and not between single PEDOT segments or dopants in the lateral direction, whilst in the vertical direction the current limiting hopping transport occurs between dilute states inside the quasi-insulating PSS lamellas.

By a post-treatment it is possible to modify PEDOT:PSS to raise its conductivity, by orders of magnitude. Typically, the addition of sorbitol to the aqueous dispersion of PEDOT:PSS that is used to deposit thin films via spin coating leads to an enhancement of the conductivity after thermal annealing. The causes and consequences of such behavior were investigated in detail. Chapter 5 describes the various properties of the highly conductive sorbitol-treated PEDOT:PSS, such as the conductivity itself, and the effects of thermal annealing and exposure to moisture. It is found that the conductivity enhancement upon addition of sorbitol is accompanied by a better environmental stability. Surprisingly, the electrical conductivity of PEDOT:PSS thin films without sorbitol treatment is increased by more than one order of magnitude in an environment with more than 30-35 % relative humidity. This effect is attributed to an ionic

contribution to the overall conductivity. Thermal gravimetric analysis (TGA), direct insert probe-mass spectrometry (DIP-MS) and modulation differential scanning calorimetry (MDSC) were used as additional tools to demonstrate that, after thermal treatment, the concentration of sorbitol in the final PEDOT:PSS layer is negligibly small.

In Chapter 6, scanning Kelvin probe microscopy (SKPM) is employed to measure the surface potential and work function of this PEDOT:PSS films that were deposited from water with different sorbitol concentrations. It is shown that work function of PEDOT:PSS is reduced with increasing sorbitol concentration. This shift can be explained by –and is in agreement with– a reduction in the surface enrichment with PSS of the film.

To study the charge transport properties of the highly conductive sorbitol-treated PEDOT:PSS films, temperature dependent and electric field dependent measurements are correlated with morphological analysis by STM in Chapter 7. It is found that by sorbitol treatment the hopping transport changes from 3D-VRH to 1D-VRH. This transition is explained by a sorbitol-induced self-organization of the PEDOT-rich grains into 1D aggregates that are aligned within micrometer sized domains, as observed in STM images.

Samenvatting

Gebruikmakend van de unieke mechanische, elektronische, en optische eigenschappen van geconjugeerde organische en polymere materialen zijn diverse technologische en commerciële toepassingen daarvan ontwikkeld, zoals sensoren, geheugens, zonnecellen en lichtemitterende diodes (LEDs). In dit verband, is het centrale thema van dit proefschrift de elektrische geleiding en het mechanisme van ladingstransport in PEDOT:PSS, een polymereemengsel dat bestaat uit een geleidend poly(3,4-ethyleendioxythiofeen) polykation (PEDOT) en een poly(styrensulfonaat) polyanion (PSS). PEDOT:PSS wordt algemeen gebruikt als elektrodemateriaal in genoemde ‘plastic elektronica’ toepassingen. Ofschoon het geleidingsvermogen van PEDOT:PSS vele grootteordes kan variëren, afhankelijk van de wijze waarop het verwerkt tot dunne film, is de reden daarvan nagenoeg onbekend. In dit proefschrift wordt het anisotrope ladingstransport van PEDOT:PSS in detail bestudeerd en gecorreleerd met de morfologie, de vorm en de dimensie van de fasescheiding tussen de twee componenten, PEDOT en PSS.

Vooruitlopend op het onderzoek aan PEDOT:PSS, wordt in Hoofdstuk 2 een nieuwe barriërelaag beschreven die de levensduur van organische devices kan verlengen. Een belangrijk degradatiemechanisme in polymere LEDs is foto-oxidatie van de actieve laag. Het isoleren van de actieve laag van water en zuurstof is daarom essentieel voor de levensduur. Plasmageïnduceerde chemische damp depositie (PECVD) is gebruikt om een dunne laag van koolstofnitride bij lage temperatuur, lager dan 100 °C, te deponeren op een polymere LED gebaseerd op poly[2-methoxy-5-(2'-ethylhexyloxy)-1,4-fenyleen vinyleen] (MEH-PPV) als actieve laag. Een dunne laag koolstofnitride fungeert als barrière voor vocht maar is tevens voldoende buigbaar voor toepassing in flexibele LEDs. De kenmerken van koolstofnitride en MEH-PPV films zijn onderzocht met optische spectroscopie, met nadruk op het degradatieprocédé van MEH-PPV onder belichting. De metingen tonen aan dat de koolstofnitride barriërelaag de polymeerfilm inderdaad beschermt en de foto-oxidatie aanzienlijk vermindert. Om het effect van de inkapseling in echte devices te bestuderen zijn polymere LEDs gemaakt en de gemeten stroom-spanningskarakteristieken bevestigen de langere

levensduur in aanwezigheid van een koolstofnitride barrièrelaag. De doelstelling, een levensduur langer dan 10.000 uur die nodig is voor commerciële toepassingen, is niet bereikt.

De resterende hoofdstukken van dit proefschrift beschrijven het onderzoek aan PEDOT:PSS. PEDOT:PSS wordt alom gebruikt in de organische elektronica. Tot dusver is betrekkelijk weinig aandacht besteed aan het mechanisme van ladingstransport in dit materiaal en aan de correlatie van die elektrische transporteigenschappen eigenschappen met de morfologie. In Hoofdstuk 3 worden raster sondemicroscopie (SPM) en macroscopische geleidingsmetingen gebruikt om tot een volledig drie dimensionaal (3D) morfologisch model te komen dat kwalitatief het waargenomen anisotrope geleidingsvermogen van gespincoate PEDOT:PSS films verklaart. Topografische rastertunnelmicroscopie (STM) afbeeldingen en atomaire krachtmicroscopie (X-AFM) dwarsdoorsneden tonen aan dat de film georganiseerd is in horizontale lagen van afgevlakte PEDOT-rijke deeltjes die door quasi-ononderbroken PSS lamellen worden gescheiden. In de verticale richting leiden de horizontale, isolerende PSS lamellen tot een sterk verminderd geleidingsvermogen en veroorzaken zij het 'dichtste-nabuur hopping' (nn-h) geleidingsmechanisme. In de laterale richting vindt 3D 'variabele-afstand hopping' (3D-VRH) ladingstransport plaats tussen PEDOT-rijke clusters die door veel dunnere PSS lagen worden gescheiden, wat tot een verbeterd geleidingsvermogen in deze richting leidt.

Deze bespreking wordt uitgebreid in Hoofdstuk 4, waar een kwantitatieve beschrijving van de lengteschalen van het overheersende ladingstransport wordt verkregen. In het bijzonder wordt aangetoond dat laterale hopping plaatsvindt tussen PEDOT-rijke clusters en niet tussen individuele PEDOT segmenten of additieven, terwijl in de verticale richting de stroom beperkt wordt door 'hops' tussen toestanden binnen de quasi-isolerende PSS lamellen.

Door nabehandeling is het mogelijk om het geleidingsvermogen van PEDOT:PSS significant, grootteorden, te verhogen. De toevoeging van sorbitol aan de watergedragen dispersie van PEDOT:PSS die gebruikt wordt voor depositie door spincoaten leidt, na een thermische behandeling, tot een verhoging van het geleidingsvermogen. De oorzaken en de gevolgen van dergelijk gedrag zijn in detail onderzocht. Hoofdstuk 5 beschrijft de diverse eigenschappen van hooggeleidende sorbitolbehandelde PEDOT:PSS films, zoals het geleidingsvermogen zelf, de gevolgen van de thermische behandeling en het effect

van de blootstelling aan vochtigheid. Aangetoond is dat de verhoging van het geleidingsvermogen door toevoeging van sorbitol, vergezeld wordt door een betere omgevingsstabiliteit. Verrassend is dat het geleidingsvermogen van dunne PEDOT:PSS films zonder sorbitol behandeling met meer dan één grootteorde wordt verhoogd in een omgeving van meer dan 30-35% relatieve luchtvochtigheid. Dit effect wordt toegeschreven aan een ionische bijdrage aan het geleidingsvermogen. Thermische gravimetrische analyse (TGA), massaspectrometrie met een directe insert monstersonde (DIP-MS) en gemoduleerde differentiële scanning calorimetrie (MDSC) zijn gebruikt voor aanvullende studies om aan te tonen dat, na thermische behandeling, de concentratie sorbitol in de uiteindelijke PEDOT:PSS laag verwaarloosbaar klein is.

In Hoofdstuk 6 is raster Kelvin microscopie (SKPM) aangewend om de oppervlaktepotentiaal en werkfunctie van dunne PEDOT:PSS films te meten die uit water met verschillende sorbitolconcentratie zijn gedeponerd. Het blijkt dat de werkfunctie van PEDOT:PSS lager wordt bij toenemende sorbitolconcentratie. Deze verschuiving kan verklaard worden door -en komt overeen met- een vermindering van de oppervlakteverrijking aan PSS van de film.

Om de geleidingseigenschappen van hooggeleidende sorbitolbehandelde PEDOT:PSS films te bestuderen, worden in Hoofdstuk 7 temperatuurafhankelijke en elektrisch-veld-afhankelijke metingen gecorreleerd met een morfologische analyse met STM. Door sorbitolbehandeling blijkt het hoppingtransport van 3D-VRH naar 1D-VRH te veranderen. Deze overgang wordt verklaard door een sorbitol veroorzaakte zelforganisatie van de PEDOT-rijke clusters in 1D aggregaten die binnen micrometergrote domeinen georiënteerd zijn, zoals in STM beelden wordt waargenomen.

Resumo

As interessantes propriedades eletrônicas, mecânicas e óticas dos materiais orgânicos conjugados fizeram emergir diversas aplicações tecnológicas e comerciais em dispositivos baseados nesses materiais, tais como sensores, memórias, células solares e diodos emissores de luz poliméricos (LEDs). Neste sentido, o tema central desta tese é o estudo das propriedades elétricas e morfológicas e os mecanismos de transporte eletrônico de cargas no PEDOT:PSS, uma blenda polimérica que consiste de um polycation condutivo, o poli(3,4-etilenodioxitiofeno) (PEDOT) e do poliânion poli(estirenosulfonado) (PSS). PEDOT:PSS é amplamente usado como material de eletrodo em aplicações na área de 'eletrônica plástica', como mencionado anteriormente. Apesar da condutividade elétrica dos filmes finos de PEDOT:PSS possa variar várias ordens de grandeza, dependendo do método pela qual é processado e transformado em filme fino, as razões para este comportamento é essencialmente desconhecido. Esta tese descreve um estudo detalhado do transporte eletrônico de cargas anisotrópico e sua correlação com a morfologia, as condições e as dimensões da separação de fase entre os dois materiais, PEDOT e PSS.

Antes de abordar as propriedades do PEDOT:PSS, uma camada de filme fino inorgânica usada para aumentar o tempo de vida de dispositivos orgânicos é descrita no Capítulo 2. Um importante mecanismo de degradação em LEDs poliméricos é a fotooxidação da camada ativa. Assim, isolar a camada ativa da água, oxigênio e luz, torna-se crucial para o aumento do tempo de vida. Um sistema de deposição química a partir da fase de vapor estimulada por plasma (PECVD) é usado para depositar filmes finos de nitreto de carbono em baixas temperaturas, menores que 100 °C, sobre PLEDs com a intenção de aumentar o tempo de vida destes dispositivos e diminuir a fotodegradação do poli[2-metoxi-5-(2-etil-hexiloxi)-p-fenileno vinileno] (MEH-PPV) em ambiente atmosférico. O filme fino de nitreto de carbono possui as características de um material que pode bloquear a umidade e que tem espessura e flexibilidade adequados para a nova geração de PLEDs flexíveis. As características dos filmes finos de nitreto de carbono e MEH-PPV foram investigadas usando-se técnicas de

espectroscopia ótica, com particular ênfase no processo de degradação do MEH-PPV sob iluminação. Os resultados mostraram que o filme fino de nitreto de carbono protege o filme polimérico e diminui consideravelmente a fotooxidação. Para avaliar o efeito do encapsulamento em dispositivos reais, LEDs poliméricos foram fabricados e pelas curvas de corrente-tensão um aumento no tempo de vida é confirmado quando a camada de nitreto de carbono é presente. O tempo de vida desejado, maior que 10.000 horas, para aplicações comerciais não foi atingido, entretanto, o encapsulamento pode ser melhorado otimizando as propriedades da camada de nitreto de carbono e combinando-as com camadas de outros materiais orgânicos e inorgânicos.

Os capítulos seguintes deste trabalho aborda os estudos realizados com o PEDOT:PSS, uma vez que é amplamente usado em eletrônica orgânica, mas relativamente tem recebido pouca atenção com respeito ao transporte eletrônico de cargas, bem como sua correlação com a morfologia. No Capítulo 3, experimentos com microscopia de varredura por sonda (SPM, 'Scanning Probe Microscopy') e medidas de condutividade macroscópica são utilizados para estudar e obter um modelo 3D morfológico completo que explica, qualitativamente, a condutividade anisotrópica observada nos filmes finos de PEDOT:PSS depositados pela técnica de 'spin coating'. Imagens topográficas de microscopia de varredura por tunelamento (STM) e imagens da seção transversal observadas com o microscópio de força atômica (X-AFM) revelaram que o filme fino polimérico é organizado em camadas horizontais de partículas planas ricas em PEDOT, separadas por lamelas quasi-contínuas de PSS. Na direção vertical, lamelas horizontais do isolante PSS reduzem a condutividade e impõe o transporte eletrônico a ser realizado por saltos em sítios vizinhos próximos (nn-H, 'nearest-neighbor hopping') nas lamellas de PSS. Na direção lateral, o transporte eletrônico via saltos 3D em sítios a longas distâncias (3D-VRH, 'variable range hopping') ocorre entre as ilhas ricas em PEDOT que são separadas por barreiras muito mais finas de PSS, causando um aumento da condutividade nesta direção. Esta discussão é estendida ao Capítulo 4 com uma descrição quantitativa do transporte eletrônico de cargas predominantes. Particularmente, é demonstrado que o transporte de cargas via saltos 3D em sítios a longas distâncias ocorre entre ilhas ricas em PEDOT e não entre segmentos isolados de PEDOT ou dopantes na direção lateral, enquanto que na direção vertical o transporte de

cargas via saltos em sítios vizinhos próximos ocorre dentro das lamelas do quasi-isolante PSS.

Em algumas aplicações, faz-se necessário usar PEDOT:PSS com alta condutividade elétrica. Isso pode ser feito adicionando-se sorbitol à solução aquosa de PEDOT:PSS. Após um tratamento térmico, e dependendo da quantidade de sorbitol adicionado, a condutividade aumenta várias ordens de grandeza e as causas e consequências de tal comportamento foram investigadas neste trabalho. O Capítulo 5 investiga as várias propriedades tecnológicas do PEDOT:PSS altamente condutivo tratado com sorbitol, tais como a própria condutividade, os efeitos dos tratamentos térmicos e exposição à umidade. É observado que o aumento da condutividade elétrica, devido à adição de sorbitol na solução aquosa, é acompanhado por uma melhoria na estabilidade da condutividade elétrica em condições atmosféricas. Surpreendentemente, a condutividade elétrica do PEDOT:PSS, sem tratamento com sorbitol ($\sim 10^{-3}$ S/cm), aumenta mais de uma ordem de grandeza sob ambiente úmido de 30-35 % umidade relativa. Este efeito é atribuído a uma contribuição iônica à condutividade total. Análise Termogravimétrica (TGA), espectrometria de massa com sonda de inserção direta (DIP-MS) e análise calorimétrica diferencial-modulada (MDSC) foram usadas como técnicas adicionais para o entendimento dos estudos deste Capítulo.

No Capítulo 6, microscopia de varredura por sonda-Kelvin (SKPM) foi empregada para medir o potencial de superfície dos filmes finos de PEDOT:PSS tratados com diferentes concentrações de sorbitol. Mostra-se que a mudança no potencial de superfície é consistente com uma redução de PSS na superfície do filme fino.

Para estudar o transporte eletrônico nos filmes finos de PEDOT:PSS altamente condutivos tratados com sorbitol, o Capítulo 7 usa medidas de temperatura e campo elétrico em função da condutividade correlacionados com análises morfológicas realizadas por STM. É observado que o transporte eletrônico por saltos, na direção lateral, muda de 3D-VRH para 1D-VRH quando o PEDOT:PSS é tratado com sorbitol. Esta transição é explicada por uma auto-organização das ilhas ricas em PEDOT em agregados 1D, devido ao tratamento com sorbitol, tornando-se alinhadas em domínios micrométricos, como observado pelas imagens de STM.

List of Figures

- Figure 1.1: Chemical structure of few π -conjugated polymers and their band gap energy [8]. ... - 5 -
- Figure 1.2: Bonding in conducting conjugated polymers. The sp^2 hybrid orbitals are shown in light gray, and the unhybridized p_z orbitals in white. Electrons are represented by the dots. The two sp^2 hybrid orbitals on the side extend in and out of the plane of the page. - 6 -
- Figure 1.3: Left: cartoon representing the top view of the morphology of a thin film of PEDOT:PSS particles, surrounded by a thin PSS-rich surface layer. PEDOT chains are displayed as short bars. Right: chemical structure of the species present in the film (reproduced from M. M de Kok *et al.* [20]). - 8 -
- Figure 1.4: Schematic representation of a carrier hop from a site with energy E_i to an empty site with energy E_j by absorption of a phonon. $e^{-L/\xi}$ is the tunneling decay, where L is the hopping distance and ξ the localization length. The conductivity of the entire system is determined by the optimal network of hopping sites. The optimal hopping distance decreases with increasing temperature, therefore this mechanism is referred to as variable-range hopping (VRH). - 10 -
- Figure 1.5: Schematic representation of the main components of a scanning tunneling microscope (STM). The tunneling current between a conductive tip and sample is exponentially dependent on their separation, d (c is a numerical factor). A feedback loop is used to maintain a constant tunneling current during scanning by vertically moving the scanner at each (x,y) data point until a setpoint current is reached. (reproduced from [25]). - 12 -
- Figure 1.6: (a) Topographic and (b) current STM images of a 100 nm-thick film of PEDOT:PSS treated with 10 wt-% of sorbitol acquired on $1 \times 1 \mu\text{m}^2$. Vertical scales are 20 nm and 1 pA, respectively, for (a) and (b). A first scan at 3 V probes a surface of “badly” conductive material, resulting in the “cloudy” image on the lower half of the images. At somewhat lower bias, 1 V, the better conducting bulk of PEDOT:PSS is reached, as seen in the upper half of the images. The tunneling current was set at 1 pA for both low and high bias scans. - 13 -
- Figure 1.7: Scanner head of a Veeco (previously Digital Instruments) MultiMode AFM: 1 - laser, 2 - mirror, 3 - cantilever (the tip is on the bottom side), 4 - tilt mirror, 5 - photodetector (reproduced from [24]). - 15 -
- Figure 1.8: Phase imaging of a surface. The difference between the applied (dashed line) and the detected (full line) oscillation is a measured of the mechanical properties of the sample. For example, a hard surface results in a small difference, whereas a softer region produces a large phase shift. The right side images illustrate the difference in the phase across the surface of a triblock copolymer (PS-b-PB-b-PS) thin film. A virtually flat topographic surface shows more pronounced structure in the phase image, where the stiffer PS lamellae appear bright in the phase image. For more details see [28] - 16 -
- Figure 1.9: Schematic of AFM and “lift mode” operation for surface potential (V_{sp}) determination (adapted from [24]). - 17 -
- Figure 1.10: (a) The most simple structure of a P/OLED; (b) band structure of an OLED operating in forward bias: (1) charge carrier injection, (2) charge carrier transport, (3) exciton formation, (4) radiative exciton decay (reproduced from [34]). - 18 -
- Figure 1.11: OLED encapsulation structures: (a) traditional glass or metal lid; (b) laminated barrier-coated lid; (c) thin film (reproduced from [42]). - 19 -

-
- Figure 2.1: Configuration of the polymer light-emitting diode (PLED)..... - 28 -
- Figure 2.2: Schematic illustration of the illumination system with ELH-type lamp, white light, used for degradation experiments. ELH lamp illumination at 100 mW/cm^2 - 29 -
- Figure 2.3: FTIR spectra of $0.7 \mu\text{m}$ thick CN_x films. - 30 -
- Figure 2.4: UV-Visible measurements for the structures: (a) non-protected (glass/MEH-PPV) in air and dark, (b) non-protected sample (glass/MEH-PPV) under illumination and (c) protected sample (glass/MEH-PPV/carbon nitride) under illumination..... - 32 -
- Figure 2.5: Degradation ratio normalized at 500 nm for polymeric layers in the dark and in air, protected with carbon nitride and non-protected. - 33 -
- Figure 2.6: Current vs. applied voltage plots for encapsulated PLED as fabricated and at various times after fabrication with the device stored under ambient conditions..... - 34 -
- Figure 3.1: Temperature dependence of the dc conductivity of spin-coated PEDOT:PSS thin films of Baytron P and low- Na^+ PEDOT:PSS. Points are experimental data and lines are fits to Eq 3.1. (a) The electric field is applied parallel (\parallel) to the substrate, $\alpha_{\parallel} = 1/4$ and T_0 values are $4.3 \times 10^6 \text{ K}$ and $9.4 \times 10^6 \text{ K}$ for Baytron P and low- Na^+ PEDOT:PSS, respectively. (b) The electric field is applied perpendicular (\perp) to the substrate $\alpha_{\perp} = 1$ and E_3 is about 14 meV for both polymers. Note the different exponents on the horizontal axis, see main text for further explanation. - 43 -
- Figure 3.2: (a) $200 \text{ nm} \times 200 \text{ nm}$ topographic STM image of PEDOT:PSS on indium tin oxide (ITO) at 2.3 V, tunneling current 10 pA, and vertical scale 15 nm, the inset shows a line section. (b) $200 \text{ nm} \times 200 \text{ nm}$ cross-sectional AFM phase image of cleaved PEDOT:PSS on glass, vertical scale is 8° . The glass substrate is on the bottom side of the image, as shown by the inset of $530 \text{ nm} \times 580 \text{ nm}$ and vertical scale 70° . A pancake-like particle is highlighted by the ellipse. - 46 -
- Figure 3.3: Cross-sectional view of the schematic morphological model for PEDOT:PSS thin films derived from combined STM and X-AFM measurements. PEDOT-rich clusters (dark) are separated by lamellas of PSS (bright). The PEDOT-rich lamella is composed of several pancake-like particles as pictured by the dotted lines. The typical diameter d of the particles is about 20–25 nm and the height h is about 5–6 nm. - 47 -
- Figure 3.4: Topographic STM images of low- Na^+ PEDOT:PSS on ITO. (a) $1 \mu\text{m} \times 1 \mu\text{m}$; (b) $500 \text{ nm} \times 500 \text{ nm}$, (c) as for (b), for Baytron P. For all images, the tunneling current was 10 pA, bias 2.3 V, and vertical scale 10 nm. - 48 -
- Figure 3.5: (a) Layout of the shadow mask used to evaporate Cr/Au electrodes for in-plane electrical measurements (top) and schematic side view of the samples (bottom). Samples are labeled A–I from top left to right bottom. (b) Typical conductivity of eight pieces of a $3 \text{ cm} \times 3 \text{ cm}$ PEDOT:PSS sample, measured in air (piece D was left out). Capital letters indicate the piece, and the small letters indicate the pair of electrodes used in the 2-point measurements. 4-point measurements yielded identical results. The average conductivity is $(8.5 \pm 0.7) \times 10^{-5} \text{ S/cm}$ - 49 -
- Figure 4.1: Schematic representation of the morphological model for PEDOT:PSS, side view. Quasi-metallic PEDOT-rich clusters (hatched regions) are separated by lamellas of insulating PSS (gray background)..... - 57 -
- Figure 4.2: Symbols represent conductivity vs (a) $T^{3/4}$, and (b) T^{-1} for PEDOT:PSS samples measured in lateral (\parallel) and vertical directions (\perp), respectively. Straight lines are fits to Eq 4.1. The insets show the used devices. The bottom gold layer in the vertical device shunts the ITO underneath, which has a much higher resistivity. Electrical contacts are made to both gold pads, which have a lateral separation of less than 1 mm. . - 58 -
-

- Figure 4.3: Correlation coefficients of the measured and fitted (using eq. 4.1) conductivity versus exponent α for PEDOT:PSS samples measured in lateral (\parallel) and vertical directions (\perp) over 77 K – 300 K. - 59 -
- Figure 4.4: (a) Conductivity vs. F/T for PEDOT:PSS thin film measured in vertical (\perp) direction with respect to the film plane at different temperatures. Solid lines are fits to Eq 4.3; (b) Temperature dependence of the characteristic hopping length L_{\perp} for the same sample. $L_{\perp} = (1.4 \pm 0.4)$ nm. - 61 -
- Figure 4.5: (a) Conductivity vs. F/T for PEDOT:PSS thin film measured in lateral (\parallel) direction with respect to the film plane at different temperatures. Solid lines are fits to Eq. 4.5. (b) Temperature dependence of the characteristic hopping length L_{\parallel} for the same sample. - 63 -
- Figure 4.6: Conductivity vs. F/T for a PEDOT:PSS film measured in lateral (\parallel) direction with respect to the film plane at different temperatures. Solid lines are fits to Eq. 4.4, considering the presence of reverse hops, or *returns* in the optimal percolation pathway. The insets show the same conductivity vs. F/T plots for sample at 83 K, 100 K, and 123 K restricted to low electric fields. - 66 -
- Figure 5.1: Chemical structure of PEDOT (bottom) and PSS (top). - 74 -
- Figure 5.2: Variation of the conductivity with temperature during process 2, i.e. heating up to 200 °C, constant at 200 °C for 2 min, and subsequent cooling of PEDOT:PSS thin films with (a) 0 wt-% (pristine film) and (b) 2.5 to 10 wt-% of sorbitol concentrations. Measurements were performed under N_2 environment. The insets show the evolution of the conductivity as a function of time during the annealing process. The conductivities of process 1 in (a) were measured for sample right after spin coating, i.e. prior to annealing, (open pentagons) and after quick annealing + forced cooling down (open stars). All the other arrows indicate the thermal cycling direction during process 2. - 77 -
- Figure 5.3: Conductivity versus relative humidity (RH) for samples with different sorbitol concentrations under medium (up to 30 % of relative humidity, open stars) and high (up to 50 % of relative humidity, open circles) moisture levels: (a) 10 wt-%, (b) 5 wt-%, (c) 2.5 wt-% and (d) 0 wt-%. Samples were kept at maximum moisture levels, i.e. about 30 % and 50 %, during 1.5 to 2 hours and annealed afterwards (closed symbols). The arrows indicate the moisture cycling, RH(%) up (green symbols), constant (red symbols) and down (blue symbols) and where the conductivity ended up after a second annealing procedure at 200 °C for 2 min (closed red dot and stars for annealing after the RH sweeps up to 30 % and 50 %, respectively). - 80 -
- Figure 5.4: TGA of pristine PEDOT:PSS (\square) and PEDOT:PSS mixed with 10 wt-% of sorbitol (\circ) under a moisturized atmosphere. W_0 , W_w and W_d are the weights of the fresh, wet and dry samples, respectively. The inset shows the absorbed mass of the pristine film measured with QMB when a moisturized atmosphere of 49 % RH is introduced (at $t = 6$ min.) and removed (at $t = 16$ min.). - 82 -
- Figure 5.5: Temperature dependence of the conductivity for PEDOT:PSS thin films before any treatment (\circ), after annealing (\triangle), and after exposure to humidity (\square). Lines are fits to Mott's 3D-VRH expression, see text. - 84 -
- Figure 6.1: Conductivity versus (a) annealing temperature and (b) annealing time for PEDOT:PSS thin films mixed with 2.5, 5, and 10 wt-% sorbitol. For comparison, the pristine film (0 wt-%) is also shown. - 93 -
- Figure 6.2: $2 \times 2 \mu\text{m}^2$ topographic AFM images of PEDOT:PSS thin films processed from an aqueous dispersion containing sorbitol in different concentrations: (a) 0 wt-% (pristine); (b) 2.5 wt-%; (c) 5 wt-%; (d) 10 wt-%. The rms-roughness is 1.05, 1.38, 1.76, and 2.36 nm, respectively. The vertical scale is 5 nm for all images. - 95 -

- Figure 6.3: (a) Work function of PEDOT:PSS thin films spin cast from solutions with different sorbitol concentrations. The work function of ITO is shown for comparison. (b+c) Schematic representation of the band diagrams during SKPM on PEDOT:PSS thin films. (b) pristine PEDOT:PSS with a PSS-rich surface layer and (c) sorbitol-treated PEDOT:PSS without PSS surface layer. χ_s^0 , χ_s and χ_{tip} , are respectively the work functions of 'bulk' PEDOT:PSS, sorbitol-treated PEDOT:PSS thin film, and the tip. Δ is the surface dipole due to the PSS-rich surface layer, which effectively enhances the film work function to $\chi_s^0 + \Delta$ - 96 -
- Figure 6.4: 500 × 500 nm² TM-AFM phase images of PEDOT:PSS thin films: (a) first image acquired at $t = 0$ for a PEDOT:PSS thin film processed from an aqueous dispersion containing 10 wt-% sorbitol; (b) same as (a) for $t \sim 7$ hours; (c) same as (a) for $t \sim 14$ hours. Vertical scale is 15 ° for all images - 97 -
- Figure 7.1: Temperature dependence of the conductivity for PEDOT:PSS samples with (Δ) 2.5 wt-%, (O) 5 wt-% and (\square) 10 wt-% of sorbitol concentration added to the aqueous dispersion used for spin coating of the films. Straight lines are fits to Eq. 7.1. Upper right inset: analysis of the exponent α for the whole temperature range, i.e. the correlation coefficient R of the fit of Eq. 7.1 to the data in the main panel plotted versus α . The vertical dashed line represents $\alpha = 1/2$. Lower left inset: evolution of T_0 and σ at 300 K as a function of sorbitol concentration, the dashed lines serves to guide the eye. The values of these parameters are also shown in Table 7.I..... - 106 -
- Figure 7.2: Conductivity as a function of F/T for PEDOT:PSS thin films with 2.5 wt-% and 10 wt-% of sorbitol added to the aqueous dispersion used for spin coating of the films at different temperatures. Solid lines are fits to Eq. 7.3. - 108 -
- Figure 7.3: Temperature dependence of the characteristic hopping length for PEDOT:PSS thin films with (O) 2.5 wt-% and (\square) 10 wt-% of sorbitol added to the aqueous dispersion used for depositing the layers. The dashed lines connect the data points, the solid lines are fits to Eq. 7.4. The inset shows the analysis of the power exponent α in Eq. 7.1 for temperatures below T_{C1} , i.e. the correlation coefficient R to the fit of Eq. 7.1 is plotted versus α . A vertical dashed line at $\alpha = 1/2$, clearly shows the shift of the best-fitting value of α to lower values, in this case $\alpha_{2.5 \text{ wt-\%}} = 0.40 \pm 0.02$ and $\alpha_{10 \text{ wt-\%}} = 0.39 \pm 0.03$ - 110 -
- Figure 7.4. Topographic STM images of PEDOT:PSS spin coated on ITO with different sorbitol concentration in the aqueous dispersion: (a) 0 wt-% (pristine) [bias: 2.3 V; $I_{\text{tunneling}}$: 20 pA], (b) 2.5 wt-% [bias: 0.1 V; $I_{\text{tunneling}}$: 10 pA], and (c) 10 wt-% [bias: 0.5V; $I_{\text{tunneling}}$: 0.5 pA]. All images were captured in areas of 500 × 500 nm² and vertical scale of 10 nm. The 20-40 nm sized bright objects and the thin depressions are interpreted as PEDOT-rich particles and separating PSS barriers, respectively [38]. - 113 -
- Figure 7.5: 250 × 250 nm² cross-sectional AFM phase image of cleaved PEDOT:PSS deposited on glass from an aqueous dispersion containing 2.5 wt-% sorbitol. Vertical scale is 30 °. Bright and dark areas in the PEDOT:PSS film are interpreted as PSS lamellas and PEDOT-rich particles, respectively [38]..... - 114 -
- Figure A1: MDSC on (a) pristine PEDOT:PSS and PEDOT:PSS mixed with 5 wt-% of sorbitol. Full and dashed are the 1st and 2nd heating steps, respectively..... - 122 -
- Figure A2: First run of DIP-MS: temperature and relative total ion current (TIC) signal as a function of time for PEDOT:PSS samples with (a) different sorbitol concentration, 2.5, 5 and 10 wt-%; (b) 0 wt-%, pure sorbitol and a blank sample; (c) Absolute m/z 103 ion current ("sugar" fragment) versus temperature. The temperature profile follows a ramp of 10 °C/min up to 200 °C, at 200 °C temperature is kept constant for 2 min and then allowed to cool down. - 124 -

List of Tables

Table 2.I: Deposition parameters for carbon nitride films prepared by PECVD.....	- 29 -
Table 4.I: Parameters describing the electrical conduction in Baytron P PEDOT:PSS thin films. See text for further discussion.	- 64 -
Table 7.I: Parameters describing the electrical conduction in sorbitol-enhanced PEDOT:PSS thin films.	- 107 -

List of Symbols, Acronyms and Abbreviations

<i>HOMO</i>	Highest occupied molecular orbital
<i>LUMO</i>	Lowest unoccupied molecular orbital
<i>PEDOT:PSS</i>	Poly(3,4-ethylenedioxythiophene):poly(styrenesulfonic acid)
<i>OLED</i>	Organic light-emitting diode
<i>MEH-PPV</i>	(poly[2-methoxy-5-(2-ethylhexyloxy)-1,4-phenylene-vinylene])
<i>ITO</i>	Indium tin oxide
<i>Al</i>	Aluminum
<i>Au</i>	Gold
<i>Cr</i>	Chromium
<i>CH₄</i>	Methane
<i>He</i>	Helium
<i>N₂</i>	Nitrogen
<i>VRH</i>	Variable range hopping
<i>nn-H</i>	Nearest-neighbor hopping
<i>SPM</i>	Scanning probe microscopy
<i>STM</i>	Scanning tunneling microscopy
<i>AFM</i>	Atomic force microscopy
<i>TM-AFM</i>	Tapping mode - AFM
<i>X-AFM</i>	cross-sectional - AFM
<i>SKPM</i>	Scanning Kelvin probe microscopy
<i>FTIR</i>	Fourier Transform infra red spectroscopy
<i>UV-Vis/IR</i>	Ultraviolet-visible near infra-red spectroscopy
<i>PECVD</i>	Plasma enhanced chemical vapor deposition
<i>QMB</i>	quartz crystal microbalance
<i>TGA</i>	thermal gravimetric analysis
<i>DIP-MS</i>	Direct insert probe – mass spectrometry
<i>MDSC</i>	Modulated-differential scanning calorimetry
<i>RH</i>	Relative humidity
<i>CN</i>	Carbon nitride
<i>I</i>	Current
<i>J × V</i>	Current density versus voltage
<i>J</i>	Current density
<i>F</i>	Electric field
<i>ELH</i>	ANSI code designation for tungsten-halogen filament lamp

q, e	Elementary charge
V_{sp}	Surface potential
χ_{tip}	SKPM-tip work function
χ_{sample}, χ_s	Sample work function
χ_s^0	work function of 'bulk' PEDOT:PSS
Δ	Surface dipole
ac	Alternating current
dc	Direct current
\parallel	Perpendicular to the surface normal, lateral, in-plane
\perp	Parallel to the surface normal, vertical, out-of-the plane
σ	Conductivity
T	Temperature
E	Energy
L	Hopping distance
P	Hopping probability
ξ	Localization length
ξ'	Effective localization length
a	Average inter-site distance
D	Dimensionality (or number of dimensions)
α	Exponent in VRH expression related to D
$N(E_F)$	Density of states at the Fermi level
N_0	number of sites per unit volume
T_0	Characteristic temperature
σ_0	Conductivity prefactor
β	Numerical factor
δ	Coulomb gap
c	prefactor
k_B	Boltzmann constant
E_3	Activation energy (for nearest neighbor hopping)
d	Particle diameter
s	Particle distance/separation
R	correlation coefficient
W_0	Initial weight
W_w	Weight of the wet sample
W_d	Weight of the dry sample

Introduction

This Chapter introduces the basic concepts of π -conjugated polymers with an emphasis on the interrogated material, the conducting polymer blend PEDOT:PSS. Moreover, variable-range hopping theory, which is extensively used in this thesis to explain temperature and electric field dependent conductivity measurements, and scanning probe microscopy, the most used tool for morphological analysis, are briefly explained. A short overview about the operation and degradation of organic light-emitting diodes is also discussed. Lastly, the motivations and scope of the thesis are presented.

1.1 Organic Electronics – the future is flexible!

Organic electronics, or plastic electronics, is a relatively new multidisciplinary field of research that involves a series of conceptual, experimental, and modeling challenges regarding electronic devices made with carbon-based materials, such as (semi)conducting π -conjugated polymers and small organic molecules. It is different from conventional electronics that use inorganic materials, like silicon or gallium arsenide, in many aspects; for example due to disorder, the polaronic nature of the carriers and the dielectric constant creating, e.g. a large exciton binding energy. The first two cause the hopping transport in (almost) all practical materials, in contrast to band transport in inorganics, and hence, the low mobility/conductivity.

In the scientific and technological revolution of the last few years the study of high-performance materials has been steadily increasing including the study of carbon-based materials. The development of organic devices allows the creation of new architectures for electronic components. The quest for more powerful and smaller/thinner/flexible electronic devices requires materials with new and improved characteristics and new fabrication processes. Conducting polymers have special properties that are interesting for this new technology [1,2]. They have the electronic properties of a semiconductor, but the mechanical flexibility and ease of production of plastics. Moreover, conjugated polymers are good materials to be employed in the fabrication of electronic devices because their properties, such as disorder, can also be tuned by external parameters during chemical synthesis, within a certain band width. The charge transport in conjugated polymers is a fundamental part of this technological search.

Another important motivation for the interest in organic (semi)conductors is the expected low cost of the end product. The intrinsic flexibility of the polymers enables new and low-cost manufacturing techniques of flexible roll-up displays, RFID tags, flexible sensors, large photovoltaic arrays and many others. In fact, the manufacturing processes that will eventually be chosen for making organic electronics products are unknown. However, it appears that the economics of organic electronics will be much more attractive than silicon manufacturing. There is no need to build complex and expensive manufacturing plants, which requires cleanrooms, lithography, and implantation and so on.

Instead, new technologies are developed in which electronic circuits are printed using ink-jet technologies, stamping or other relatively cheap processes. This means that, depending on the particular technique, organic electronics products may be produced economically in relatively short runs and even customized to the needs to low-volume customers.

From the above, it is clear that in case of organic electronics the future is, indeed, literally and metaphorically flexible!

1.2 Electronic properties of conducting polymers

The basis of the field of organic electronics was established back in the 1970s with the discovery that the conductivity of polyacetylene films could be changed over several orders of magnitude by chemical doping [3]. For their breakthrough work in this area, MacDiarmid, Heeger and Shirakawa were awarded the Nobel Prize in Chemistry in the year 2000. Good introduction to the field of organic electronics are their *Nobel lectures* [4,5,6]. Conducting and semiconducting organic materials, both electron (*n-type*) and hole transport (*p-type*) materials, can nowadays be made. Since the early work, many innovative materials for the use in electronic applications have been developed and characterized. The particular bonding arrangement of the carbon atoms in the polymer backbone is the reason for the characteristic electronic properties of tunable conductivity, electrochromism, electroluminescence and electroactivity [7].

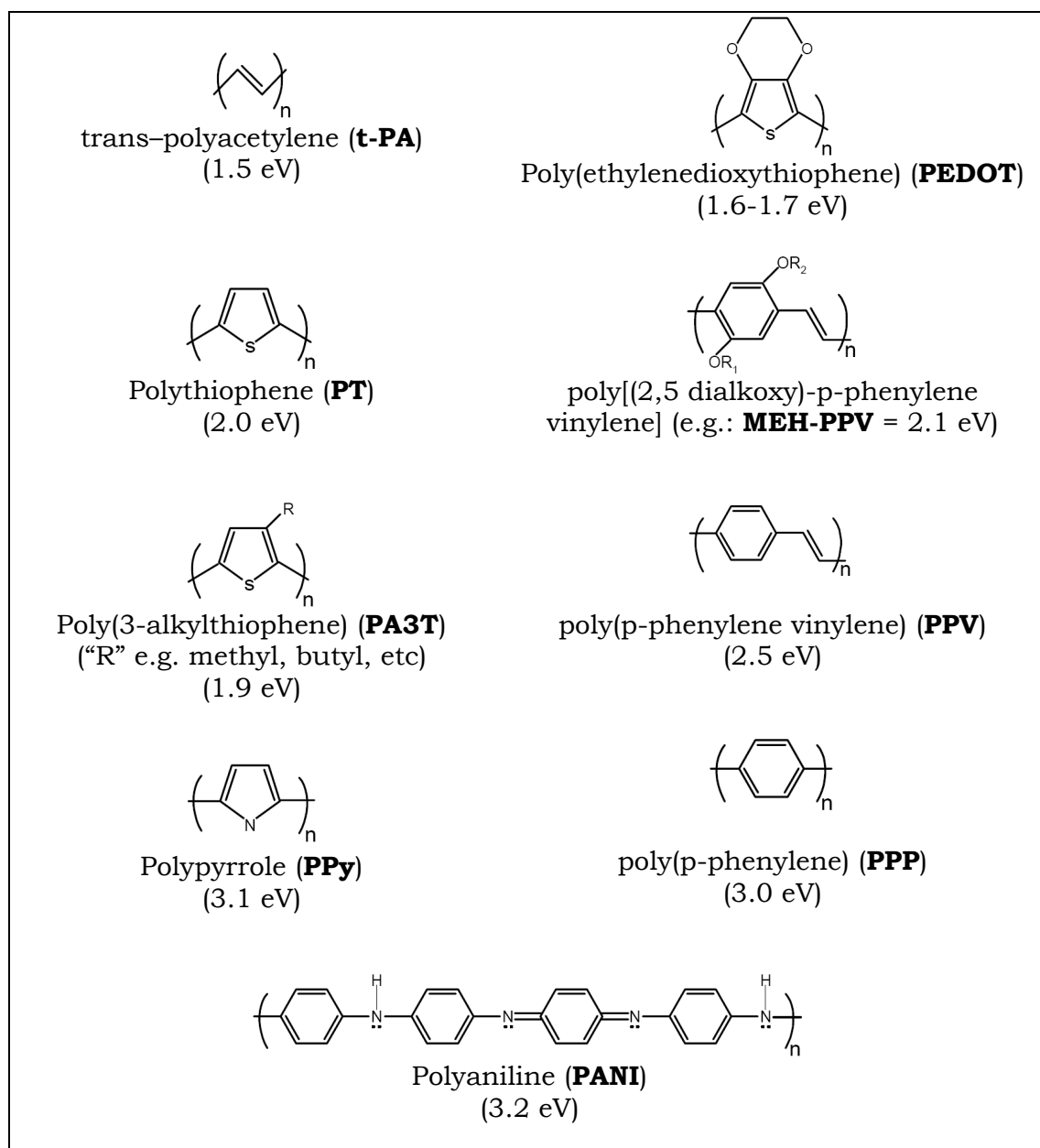


Figure 1.1: Chemical structure of few π -conjugated polymers and their band gap energy [8].

In Figure 1.1, a general characteristic is the presence of double bonds alternating with single bonds along the polymer chain, i.e. conjugated bonds. The electron configuration of the six electrons in a carbon atom (in its ground state) is $1s^2 2s^2 2p^2$. The electrons in the core orbitals do not contribute to the chemical bonding. Since the $2s$ shell is filled, this would suggest that carbon would form two bonds with its neighbors, with the unpaired $2p^2$ electrons, but we know that it forms four. The four valence electrons in the $2s^2 2p^2$ shells combine to a hybridized structure when forming covalent bonds. The s and p orbitals combine to form hybrid orbitals (sp^1 , sp^2 , and sp^3 , depending upon the number of orbitals

that is combined), which give rise to triple, double, or single bonds. In conjugated polymers, one $2s$ orbital pairs with the two $2p$ orbitals to form 3 sp^2 hybrid orbitals, leaving one p orbital unhybridized. Two of the sp^2 orbitals on each carbon atom form covalent bonds with neighboring carbons, the third generally forms a covalent bond with a hydrogen or side group. This is called a σ -bond, which is any bond with cylindrical symmetry around the internuclear axis [7]. The unhybridized p_z orbital overlaps with the unhybridized p_z orbital on the neighboring carbon. This is called a π -bond, as is any bond which arises from electrons approaching side by side, off the internuclear axis. Figure 1.2 summarizes the preceding explanation.

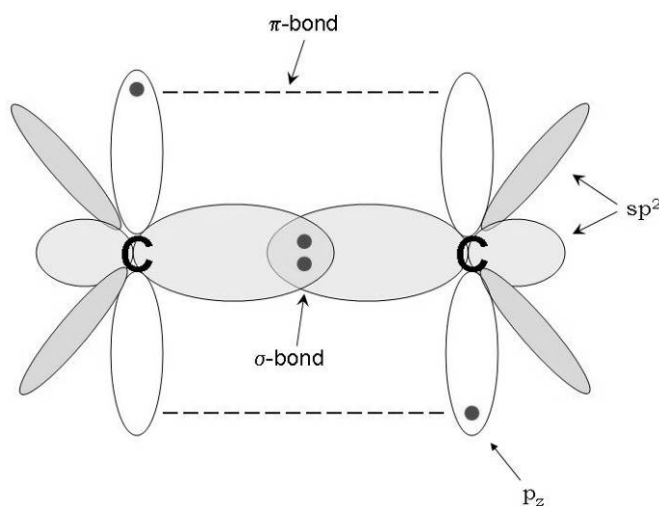


Figure 1.2: Bonding in conducting conjugated polymers. The sp^2 hybrid orbitals are shown in light gray, and the unhybridized p_z orbitals in white. Electrons are represented by the dots. The two sp^2 hybrid orbitals on the side extend in and out of the plane of the page.

The electrons in the π -bonds are weakly bound, and thus they are relatively easily delocalized. These delocalized π electrons are the conduction electrons in these materials. In summary, the sp^2 hybridization in conducting polymers is important because this leaves one p electron per atom to form its own band. Under the assumption that the single and double bonds have the same length, Bloch theory [9] tells us that solids formed from atoms or molecules with half filled shells have partially filled bands with metallic transport properties. However, the length of the single and double bonds are not identical and the Peierls instability (i.e., C-C bonds are longer than C=C bonds) [10] splits this simple band into 2 sub-bands, a completely filled valence band (highest occupied

molecular orbital or HOMO level) and an empty conduction band (lowest unoccupied molecular orbital or LUMO level), separated by an energy gap. Hence the material is a semiconductor.

Through the process of doping, the conductivity of pristine π -conjugated polymers can be changed from insulating to conducting, with the conductivity increasing as the doping level increases [7]. Both *n-type* (electron donating) and *p-type* (electron accepting) dopants have been used to induce an insulator-to-conductor transition in electronic polymers. Similar to the inorganic semiconductors, these dopants remove or add charges to the polymers, but the details are very different. Unlike substitutional doping that occurs for conventional semiconductors, the dopant atomic or molecular ions are positioned interstitially between chains in π -conjugated polymers, and donate charges to or accept charges from the polymer backbone. In this case, the counter ion is not covalently bound to the polymer, but only attracted to it by the Coulomb force. In some cases called self-doping, these dopants are covalently bound to the polymer backbone [11].

Initially added charges upon doping do not simply begin to fill the conduction band to have metallic behavior immediately. Near the doped charges the strong coupling between electrons and phonons causes distortions of the bond lengths. For the degenerate ground state polymers, e.g. trans-polyacetylene (*t-PA*), doped charges at low doping levels are stored in charged solitons [12,13,14]. For nondegenerate systems, they are stored as charged polarons or bipolarons [15]. High doping for the non-degenerate polymers results in polarons interacting to form a polaron lattice or electrically conducting partially filled energy band [16,17]. Bipolarons or the pairs of polarons are formed in less ordered regions of doped polymers [18].

The conductivity of these systems can be increased by more than 10 orders of magnitude upon doping the pristine polymer [7]. With these improvements in the electrical conductivities, many traditional signatures of metallic conductivity have been demonstrated. Some of the most highly conducting samples remain conducting even in the millikelvin range [19]. However, the conductivity of highly conducting polymers usually decreases at low temperature, which is generally taken as an indication that the material is not truly metallic. The common interpretation for this behavior is that the high density of doping-induced

conduction electrons at the Fermi level becomes spatially localized at low temperatures so only *hopping transport* remains possible [7]. The main sources of localization are structural and energetic disorder in the polymers [7].

1.3 Poly(3,4-ethylenedioxythiophene):poly(styrenesulfonic acid) (PEDOT:PSS)

The research presented in this thesis is mainly focused on understanding the effect of morphological changes on the charge transport in the conducting polymer PEDOT:PSS.

PEDOT is a relatively new member in the conducting-polymer family. It shows interesting properties, including relatively good electrochemical, ambient, and thermal stability of its electrical properties as compared with that of other polythiophenes [7]. PEDOT is built from ethylenedioxythiophene (EDOT) monomers. It is insoluble in many common solvents and unstable in its neutral state, as it oxidizes rapidly in air. To improve its processability, a polyelectrolyte solution (PSS) can be added, and this results in an aqueous dispersion of PEDOT:PSS, where PEDOT is its oxidized state. Each phenyl ring of the PSS monomer has one acidic SO_3H (sulfonate) group, see Figure 1.3.

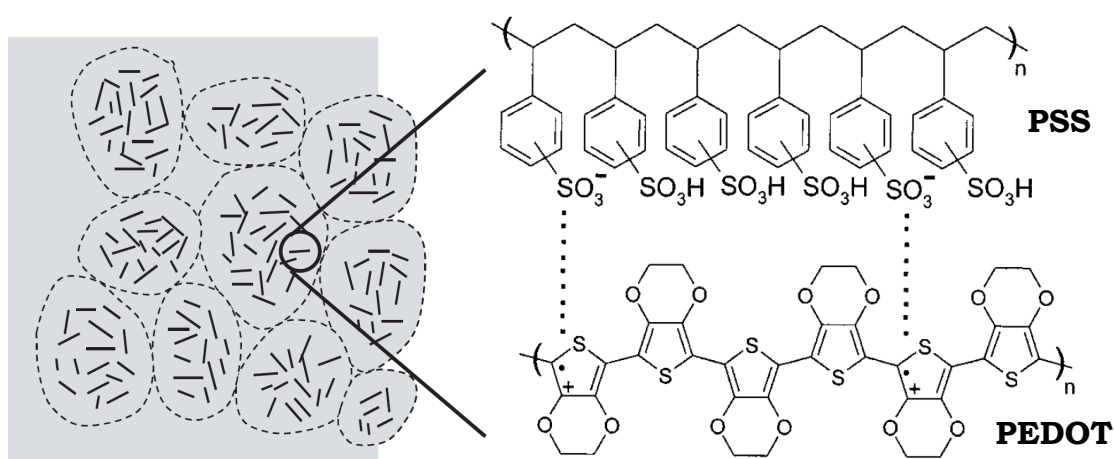


Figure 1.3: Left: cartoon representing the top view of the morphology of a thin film of PEDOT:PSS particles, surrounded by a thin PSS-rich surface layer. PEDOT chains are displayed as short bars. Right: chemical structure of the species present in the film (reproduced from M. M de Kok *et al.* [20]).

PEDOT:PSS is industrially synthesized from the EDOT monomer, and PSS as a template polymer using sodium peroxodisulfate as the oxidizing agent. This affords PEDOT in its highly conducting, cationic form [21]. The degree of polymerization of PEDOT is limited and it is assumed that PEDOT is a collection of oligomers with lengths up to ~ 20 repeating units. The role of PSS, which has a much higher molecular weight, is to act as the counter ion and to keep the PEDOT chain segments dispersed in the aqueous medium. In general PEDOT:PSS gel particles are formed that possess excellent processing characteristics to make thin, transparent, conducting films.

Aqueous dispersions of PEDOT:PSS are commercially available, for example, under the trade name Baytron P from H. C. Starck. With this material, thin, highly transparent and conductive surface coatings can be prepared by spin-casting or dip-coating on almost any hydrophilic surface. H. C. Starck offers a variety of dispersions for different applications. Depending on solid content, doping concentration, particle size and additives, films with different properties can be made. The work function of Baytron P is approximately 5.2 eV. The dispersion is acidic with a pH value between 1.5 and 2.5 at room temperature because of the PSS content [20].

In this work, the specific Baytron P VP Al 4083 OLED grade was extensively studied in Chapters 3 to 7. In the OLED grade, the PEDOT:PSS ratio is 1:6 and, which makes the material with a relative in-plane low conductivity of the order of 10^{-3} S/cm in order to avoid cross-talk between neighboring pixels.

1.4 Charge transport in disordered materials

The electric field across any material, either parallel or perpendicular to the plane, drives the charges to their respective counter electrodes, consequently, a conductivity or resistivity can be measured. In the case of conducting polymers, despite their relatively high conductivity at room temperature, it is experimentally found that they do not really behave as metals because their conductivity is not increased when they are cooled. The problem for this class of polymers is that their properties are dominated by disorder, which leads to charge localization at low temperatures. For most materials, including PEDOT:PSS, carrier localization

is dominant at all practical temperatures, i.e. temperatures that do not damage the material.

In this sense, the temperature dependence of the conductivity gives important information about the electrical conduction mechanism. Sir Nevill Francis Mott [22] developed a model to describe electron conduction in amorphous materials that is well applicable to conducting polymers. The Mott variable-range hopping (VRH) theory describes the low temperature behavior of the conductivity in strongly disordered systems, i.e. systems in which the available states are localized.

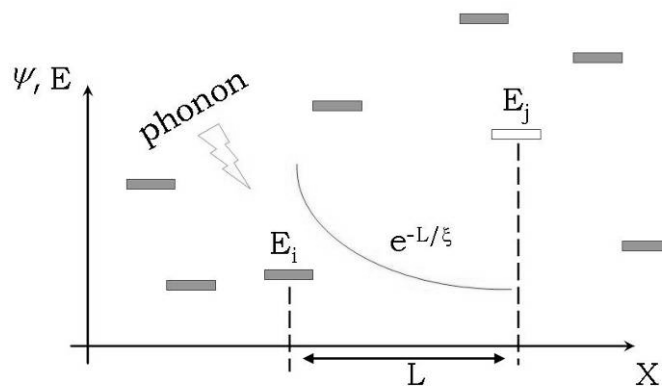


Figure 1.4: Schematic representation of a carrier hop from a site with energy E_i to an empty site with energy E_j by absorption of a phonon. $e^{-L/\xi}$ is the tunneling decay, where L is the hopping distance and ξ the localization length. The conductivity of the entire system is determined by the optimal network of hopping sites. The optimal hopping distance decreases with increasing temperature, therefore this mechanism is referred to as variable-range hopping (VRH).

In this model, charge carriers move (hop) from a localized state to a nearby localized state of different energy. Consider two states located a distance L apart in Figure 1.4. The state on the left is at energy E_i and the state on the right is at energy E_j . Suppose $\Delta E_{ij} = E_j - E_i > 0$. An electron can hop from left to right by the absorption of a phonon. In fact, there are two factors which determine an electron hopping from site i to site j . One is the tunneling factor $\exp(-L/\xi)$, where L is the hopping distance and ξ is the localization length and the other is the Boltzmann factor $\exp(-\Delta E/k_B T)$. Following Mott, the hopping probability P_{ij} for an electron to hop between two sites i and j is written as

$$P_{ij} \propto \exp\left(\frac{-2L}{\xi} - \frac{\Delta E_{ij}}{k_B T}\right) \quad \text{Eq 1.1}$$

The key ingredient in the VRH theory is that L and ΔE are connected via the density of states $N(E_F)$ as

$$L^D \Delta E N(E_F) \sim 1 \quad \text{Eq 1.2}$$

where D is the dimensionality of the system. Eq. 1.2 reflects the fact that the number of available states in a volume L^D and in an energy interval ΔE should be of the order of unity to enable percolation. Therefore, the optimum hop is the result of a competition between the two terms in the exponent in Eq. 1.1. At low temperatures, the thermal activation term tends to become large and in order to keep ΔE sufficiently small, the carrier has, according to Eq. 1.2, to hop to a site relatively far away, i.e. a non-nearest neighbor site. Optimizing P_{ij} under the condition Eq. 1.2 gives the general form of the temperature-dependent conductivity of Mott's model [22]

$$\sigma(T) = \sigma_0 \exp\left[-\left(\frac{T_0}{T}\right)^{\frac{1}{1+D}}\right] \quad \text{Eq 1.3}$$

where the parameter σ_0 is the limiting value of the conductivity at infinite temperature, and T_0 is a characteristic temperature. The exponent $1/(1+D) = \alpha$ is related to the dimensionality D of the transport process, where $D = 1, 2$ or 3 . In the conventional (3D) VRH model the characteristic temperature $T_0 (= \beta/N(E_F)\xi^3 k_B)$ is a function of the localization length ξ and the density of states $N(E_F)$.

The applicability of the VRH model is examined by plotting the experimental results in the form of $\log \sigma$ vs. $T^{-\alpha}$. In general, the least square fitted curves provide a first hand indication not only of the nature of the charge transport mechanism, but also for the dimensionality of the system.

More detailed discussions on temperature-dependent measurements and alternatives to Mott's VRH are described in detail in Chapters 3, 4, 7 and partially in Chapter 5.

1.5 Scanning Probe microscopy (SPM)

Among all characterization techniques used in this work, one of the most important was scanning probe microscopy (SPM). Several issues concerned with the electrical transport properties in the PEDOT:PSS thin films could only be elucidated by investigation and correlation with morphological properties using SPM. It is not the intention here to give all details concerned with the SPM techniques, but a basic description is given.

Scanning Tunneling Microscopy (STM)

The STM was the first SPM mode developed in 1982 by Binnig and Rohrer [23] at IBM and has since then been established as a powerful technique for the study of micro and nanoscale structures. Compared to other types of microscopy, STM has unique attributes which include: *i)* ultra-high resolution down to atomic dimensions; *ii)* 2D images with very high resolution especially in the vertical direction; *iii)* a variety of operating conditions, such as vacuum, air, and liquids; *iv)* observation range from micrometer to angstrom; and *v)* the ability to do tunneling spectroscopy. A simplified structure of a scanning tunneling microscope is shown in Figure 1.5.

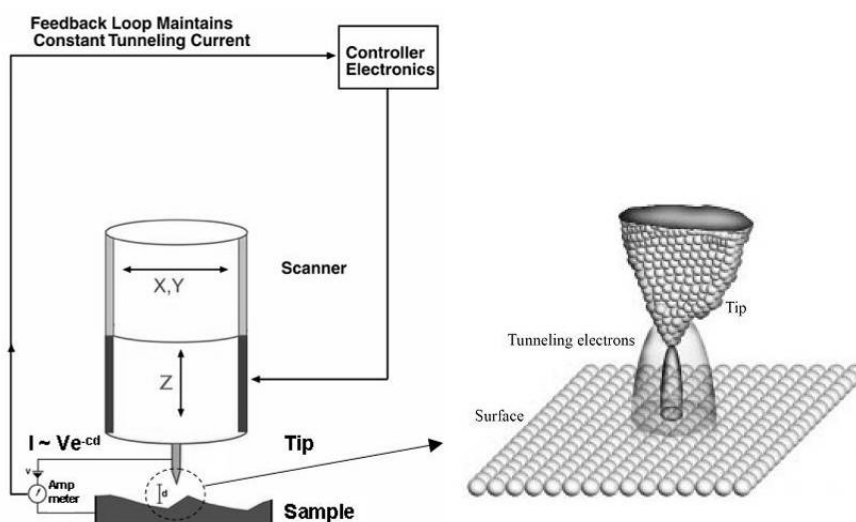


Figure 1.5: Schematic representation of the main components of a scanning tunneling microscope (STM). The tunneling current between a conductive tip and sample is exponentially dependent on their separation, d (c is a numerical factor). A feedback loop is used to maintain a constant tunneling current during scanning by vertically moving the scanner at each (x,y) data point until a setpoint current is reached. (reproduced from [24]).

The principle of STM operation is simple and is based on the electron tunneling effect. When a metal needle-like probe (tip) is brought close to a surface (1-10 Å), electrons can tunnel through the gap between the tip and the surface when an appropriate bias voltage is applied, producing a tunneling current. The tunneling current is, amongst others, a function of the bias voltage and the tip and sample materials and is extremely sensitive to the tip-sample distance. This strong distance dependence is the reason for the high vertical resolution of STM [25]. When the tip is scanned across the surface using a piezo scanner, a feedback system adjusts the height of the tip above the substrate surface to keep the tunneling current constant. This is called the *constant current mode*. It is also possible to capture the change in the tunneling current at a constant tip height in which case the STM is said to be operating in *constant height mode*.

Particularly in this work, the STM was used in constant current mode, with self-cut Pt-Ir tips. These tips were made from Pt-Ir wire of 250 μm diameter by cutting them using a simple hand tool, i.e. a cutter plier. Pt-Ir is a suitable alloy for making tips. It does not oxidize easily in air and is very hard. Other materials, for example tungsten (W), are too susceptible to oxidation to be used under ambient conditions.

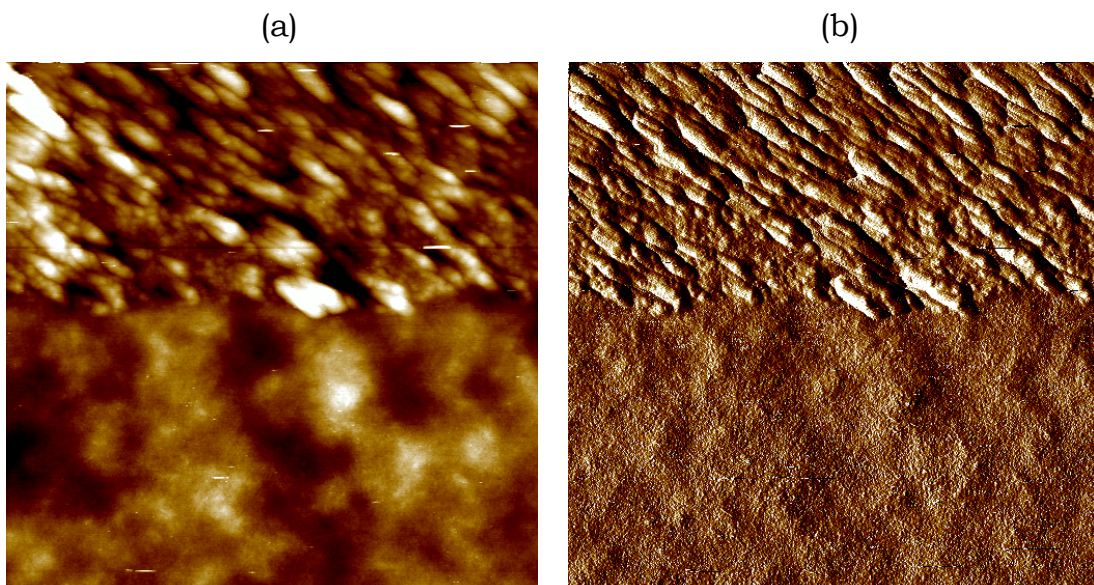


Figure 1.6: (a) Topographic and (b) current STM images of a 100 nm-thick film of PEDOT:PSS treated with 10 wt-% of sorbitol acquired on $1 \times 1 \mu\text{m}^2$. Vertical scales are 20 nm and 1 pA, respectively, for (a) and (b). A first scan at 3 V probes a surface of “badly” conductive material, resulting in the “cloudy” image on the lower half of the images. At somewhat lower bias, 1 V, the better conducting bulk of PEDOT:PSS is reached, as seen in the upper half of the images. The tunneling current was set at 1 pA for both low and high bias scans.

The resulting images of Figure 1.6 are a good example of how an STM can be used on soft organic material like PEDOT:PSS. Since setpoint current and voltage are fixed, STM images reflect a surface of constant conductance, which in low-conductivity materials does not necessarily coincide with the topographic sample surface [26]. In Figure 1.6, STM topography and current images of a PEDOT:PSS thin film treated with 10 wt-% of sorbitol is shown. A first scan at high bias setpoint, 3 V, results the lower half image. This image is identical to what is usually found by AFM (see AFM explanation below), implying that the imaged surface of constant conductance indeed reflects the ‘true’ topography. When the STM setpoint bias is lowered to 1 V the image is drastically changed. A surface of higher conductance, lying deeper in the material is probed by the STM, see upper half of the image. Chapters 3 and 7 discuss the ‘hidden’ morphology obtained by STM in this manner.

Atomic Force Microscopy (AFM)

AFM is a surface analytical technique, capable of producing images with very high resolution. It was developed 4 years after the STM, by the modification of one of the STM instruments, by Binnig *et al.* [27]. While STM is based on the quantum physical principle of electron tunneling between tip and sample, AFM operation is based on the detection of repulsive and/or attractive surface forces. The interaction between the sample surface and a tip (probe) located very close to it corresponds to the force between the atoms of the sample and those of the tip that scans the surface and the image is generated by monitoring these forces. AFM does not require a conducting sample thereby enabling the application of SPM techniques to (insulating) polymers, biological material and etc.

In the AFM systems used for the measurements in this thesis, the probing AFM tip is attached to a flexible cantilever responsible for the signal transduction. A small laser focused on the cantilever detects any bending or twisting of the cantilever. The reflection of the laser beam is focused on a segmented photodiode detector. The interaction of the sample with the tip is measured by the variation in the reflected beam’s point of incidence on the photodiode. This optics mechanism enables detection of forces between approximately 10^{-7} – and 10^{-12} N [24]. Deflection of the cantilever by interaction with features on the sample surface is monitored during scanning and translated into a 3D image of the surface.

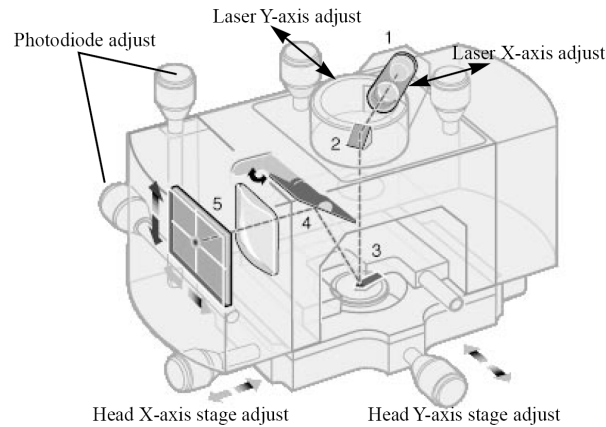


Figure 1.7: Scanner head of a Veeco (previously Digital Instruments) MultiMode AFM: 1 - laser, 2 - mirror, 3 - cantilever (the tip is on the bottom side), 4 - tilt mirror, 5 - photodetector (reproduced from [24]).

AFM can be operated in a number of different imaging modes depending on the nature of the interaction between the tip and sample surface. Earlier, in the original version of the AFM, the tip was in constant contact with the sample. This mode is known as the *contact mode*. When the tip encounters a feature higher than the current scanning level, the cantilever is bent backwards and as a result the tip applies a larger force to the surface. To avoid this, the AFM compensates by increasing the distance to the surface. The opposite takes place if the feature is lower. The height change needed for compensation is shown on the screen as the surface topography. Drawbacks, however, are a high lateral force, a strong tip wear and potential sample damage.

To avoid the problems described above, a different imaging mode was invented. This mode is known as *tapping (TM-AFM)* or *intermittent contact mode*. In this mode, the tip oscillates at its resonance frequency and is in contact with the surface only at the lower part of its oscillation. As the tip oscillates, additional information can be extracted, see Figure 1.8.

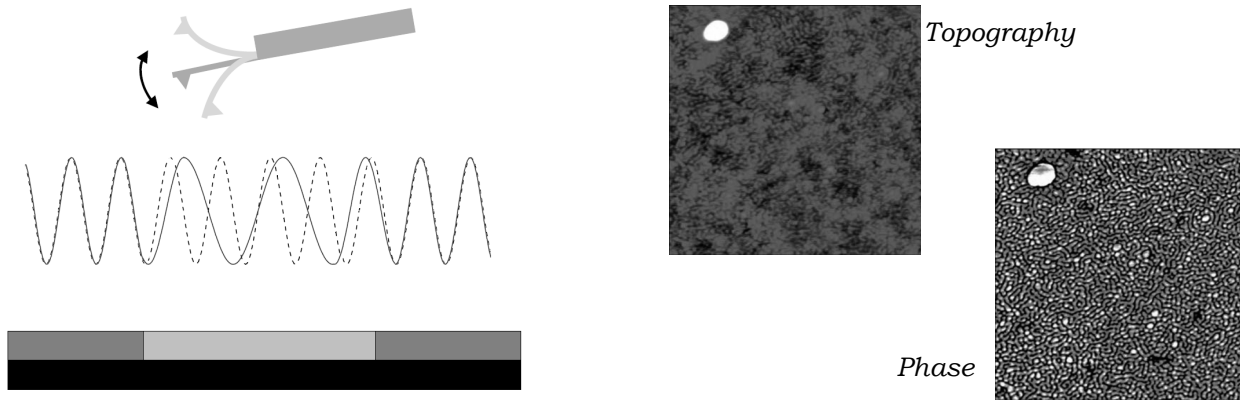


Figure 1.8: Phase imaging of a surface. The difference between the applied (dashed line) and the detected (full line) oscillation is a measured of the mechanical properties of the sample. For example, a hard surface results in a small difference, whereas a softer region produces a large phase shift. The right side images illustrate the difference in the phase across the surface of a triblock copolymer (PS-*b*-PB-*b*-PS) thin film. A virtually flat topographic surface shows more pronounced structure in the phase image, where the stiffer PS lamellae appear bright in the phase image. For more details see [28].

By comparing the difference between the applied oscillation and the actual oscillation, Figure 1.8, a phase difference can be measured. This signal is the result of the mechanical properties of the surface as well as the force interactions between the tip and the surface. The latter can be used for chemical mapping [29] and morphological structural studies [30]. Interpretation of phase-AFM images can be complex.

Scanning Kelvin Probe Microscopy (SKPM)

Following the development of SPM techniques, the electrical properties of surfaces are now being evaluated with high spatial resolution using a series of techniques derived from AFM that fall under the category of electric force microscopy (EFM). Such techniques include scanning capacitance force microscopy (SCFM) and scanning Kelvin probe force microscopy (SKPM), the latter will be explained in this sub-section. SKPM [31] is a technique that combines classical Kelvin probe with AFM and allows one to measure the local surface potential V_{sp} , which, for a metallic tip and sample with work functions χ_{tip} and χ_{sample} respectively, is given by $qV_{sp} = \chi_{tip} - \chi_{sample}$ with q the elementary charge.

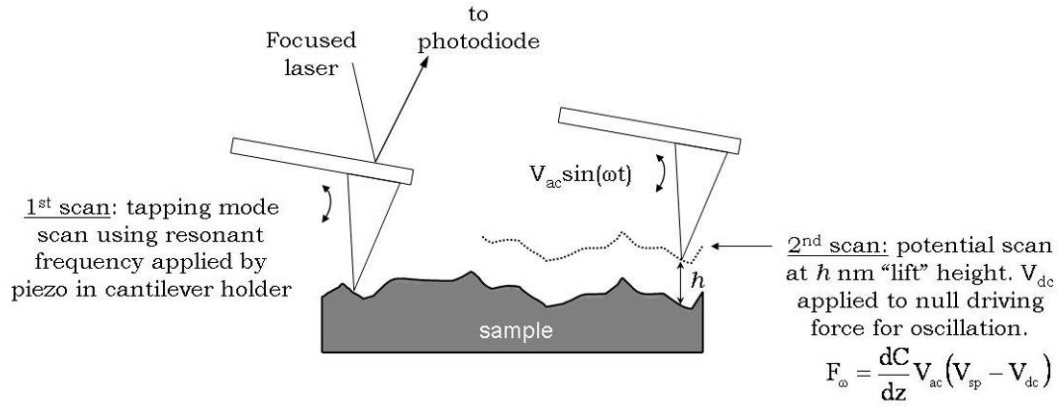


Figure 1.9: Schematic of AFM and "lift mode" operation for surface potential (V_{sp}) determination (adapted from [24]).

The Kelvin mode that is used in this work is based on the two-scan technique. In the first scan the topography is acquired using tapping mode. In the second scan this topography is retraced at a preset lift height above the sample surface during the detection of the surface potential V_{sp} . During this second scan the cantilever is no longer excited mechanically but electrically by applying the voltage (V_{tip}) to the tip. V_{tip} contains dc and ac components, $V_{tip} = V_{dc} + V_{ac}\sin(\omega t)$. The resulting capacitive force F_z along the z direction between the tip and the sample surface is $F_z = -\frac{V^2}{2} \frac{dC}{dz}$, where $V = V_{tip} - V_{sp} = V_{dc} + V_{ac}\sin(\omega t) - V_{sp}$. Combining the latter expression with the expression for F_z , the force at resonant frequency becomes $F_{\omega} = \frac{dC}{dz} V_{ac} (V_{sp} - V_{dc})$ which is used for the detection of the surface potential V_{sp} . The feedback changes the dc tip potential V_{dc} until the ω component of the cantilever movement (and accordingly F_{ω}) vanishes, i.e. V_{dc} is equal to V_{sp} . So mapping V_{dc} reflects the surface potential over the sample surface [31].

1.6 Device lifetime – Polymer Light-emitting diodes (PLEDs)

Since the development of polymeric and organic light-emitting diodes (P/OLEDs) operating at reasonably low voltages, organic electronics have attracted great interest due to the promise of lower cost and new potential niches, like large-area flat and flexible displays [32,33].

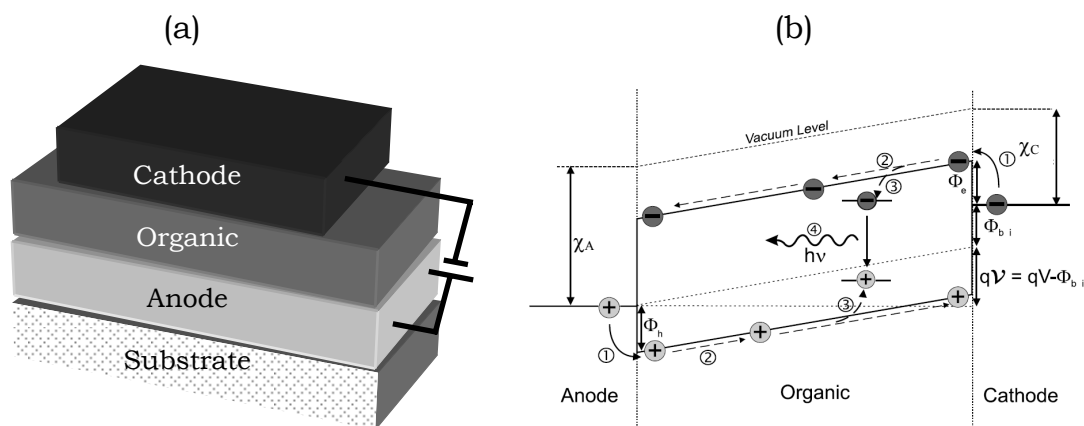


Figure 1.10: (a) The most simple structure of a P/OLED; (b) band structure of an OLED operating in forward bias: (1) charge carrier injection, (2) charge carrier transport, (3) exciton formation, (4) radiative exciton decay (reproduced from [34]).

Typically, P/OLEDs are made using thin layer(s) of organic material(s) between two electrodes. Under forward applied bias electrons and holes are injected into the organic material(s), leading to the generation of light. Figure 1.10(a) shows the structure of a P/OLED with a single organic thin layer sandwiched between the cathode (usually a metal), and the anode (usually transparent and the most used is indium tin oxide (ITO), a transparent conductive oxide material). The choice of the electrodes is an important factor in the operation of such devices because they directly control the injection of carriers into the organic layer(s). Therefore, the cathode must have a low work function, whereas the anode must have a high work function, in order to easily inject electrons and holes, respectively, into the organic material.

The color emitted by such devices depends on the HOMO-LUMO gap of the used emissive material [35] and the electroluminescence mechanism can be explained following the steps shown in Figure 1.10(b). In this scheme, positive carriers are injected by the anode and this injection depends, in first approximation, on the energy difference (ϕ_h) between the work function of the anode (χ_A) and the HOMO level of the organic material. On the other side, negative carriers are injected by the cathode and depend on the energy difference (ϕ_e) between the work function (χ_C) and the LUMO level. Once carriers are injected into the organic material they are transported by the applied electric field towards the counter electrode (2), or they relax creating a singlet exciton (3). In the case of singlet excitons, they can subsequently decay emitting light (4).

The lifetime is still a critical factor for bringing P/OLED products to the market. Many mechanisms have been proposed for the decay in luminance, but consensus exists that one of the dominant degradation mechanisms is the exposure of the organic-cathode interface to atmospheric oxygen and water [36,37]. This leads to the oxidation and delamination of the metallic cathode [38]. The steady-state photoluminescence has been seen to decrease by a factor of two after just 5 minutes in the presence of oxygen and light [39], indicating the presence of electron traps. The active organic layer itself can be also damaged due to photo-oxidation. The interaction with the oxygen breaks the organic chains or interrupts its conjugation by breaking C=C bonds, and thereby breaking the conjugation [40,41]

Thus, in order to isolate the device from atmospheric oxygen and water, encapsulation of OLEDs is a key technology, which is necessary to extend the lifetime.

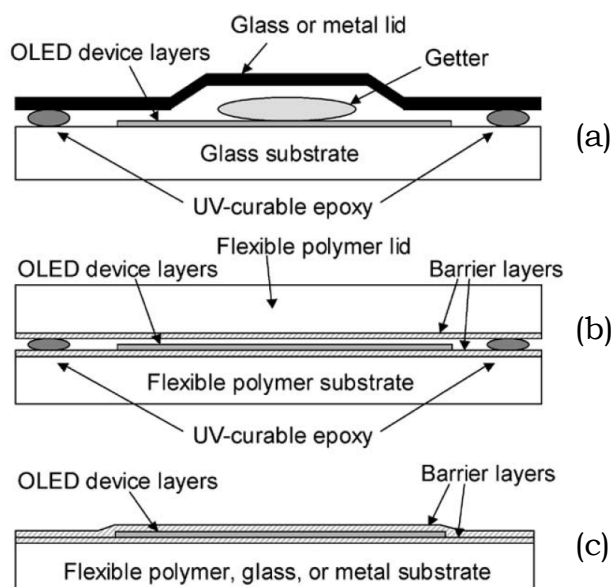


Figure 1.11: OLED encapsulation structures: (a) traditional glass or metal lid; (b) laminated barrier-coated lid; (c) thin film (reproduced from [42]).

Usually, in conventional bottom-emitting devices as shown in Figure 1.10(a), a metal lid is attached on the glass substrate as shown in Figure 1.11(a). The sealing is accomplished by applying a low-moisture-impervious adhesive resin between the lid and substrate. A getter material, such as calcium oxide or barium oxide, is often incorporate into the package to react with any byproduct of the resin cure process and any residual water incorporated in the package or

diffusing through the seal over time. However, such a packaging method may be inappropriate for new types of P/OLEDs, e.g., flexible-P/OLEDs. Furthermore, since thinner and lighter devices are always desired, direct encapsulation of P/OLEDs is a highly relevant research topic [43,44,45,46].

The second Chapter of this thesis describes the deposition of a thin film layer by PECVD technique as a protective barrier for PLEDs aiming flexible device applications.

1.7 Objectives and scope

Basically, the subjects studied in this thesis can be split into three main topics:

- (i) Encapsulation of PLEDs;
- (ii) Anisotropic transport properties of PEDOT:PSS thin films;
- (iii) Morphological and electronic properties of PEDOT:PSS treated with sorbitol.

The first topic is discussed in Chapter 2. The objective of encapsulation of PLEDs is to minimize the degradation of both polymer layers and electrodes due to the presence of oxygen and water. For this, a thin layer of carbon nitride deposited by PECVD reactor is used as encapsulation material for PLEDs. The results presented in this Chapter were a first experiment and the promising lifetime enhancement was not further explored. However, the presented results show that the high photo-oxidation rate of the active layer, studied by FTIR and UV-Vis/IR, can be prevented by the deposition of such a thin layer of carbon nitride.

The second topic discussed concerns the effects of morphology on the charge transport properties of PEDOT:PSS thin films, see Chapters 3 and 4. This study is mainly made by temperature and electric field dependent conductivity measurements and by correlating the results with film morphology as observed by AFM and STM.

The last topic deals with the morphological and electronic characteristics of PEDOT:PSS treated with sorbitol. Typically, the addition of sorbitol leads to a conductivity enhancement of the thin film and the causes and consequences of such behavior were investigated. In Chapter 5, the various technological properties of the highly conductive sorbitol-treated PEDOT:PSS thin films, such as the conductivity itself, thermal annealing, and exposure to moisture are investigated. It is found that the well-known conductivity enhancement, upon addition of sorbitol, is accompanied by a better environmental stability. Chapter 6 discusses surface potential measurements in sorbitol treated PEDOT:PSS using the SKPM technique. It is shown that a shift in the surface potential is consistent with a reduction in the surface enrichment of PSS. Finally, Chapter 7 uses the framework of Chapters 3 and 4 in order to study the transport properties of the highly conductive PEDOT:PSS thin films.

Generally, this thesis tries to explain experimental results using theoretical charge transport models with great emphasis on the correlation with the morphology.

1.8 References and notes

- [1] Time magazine recognized organic electronics as one of the 10 technologies that will eventually save the world in the 21st century, see the following link <http://www.time.com/time/2002/greencentury/entechnology.html>
- [2] S. R. Forrest, *Nature* **2004**, 428, 911.
- [3] C. K. Chiang, C. R. Fincher JR., Y. W. Park, A. J. Heeger, H. Shirakawa, E. J. Louis, S. C. Gau, A. G. MacDiarmid, *Phys. Rev. Lett.* **1977**, 39, 1098.
- [4] A. J. Heeger, *Rev. Mod. Phys.* **2001**, 73, 681.
- [5] A. G. MacDiarmid, *Rev. Mod. Phys.* **2001**, 73, 701.
- [6] H. Shirakawa, *Rev. Mod. Phys.* **2001**, 73, 713.
- [7] *Handbook of Conducting Polymers*, 3rd Ed. T.A. Skotheim, J. Reynolds (Eds.), CRC Press, **2007**.
- [8] The extraction of band gap values depend on the precision and accuracy of different methods. The values presented in Figure 1.1 are averages found in many sources, for example, see the text book in ref 7 and N.C. Greenham and R.H. Friend, *Semiconductor device physics of conjugated polymers*, in Solid State Physics, Advances in Research and Application, edited by H. Ehrenreich and F. Spaepen (Academic Press, New York, **1995**), Vol. 49, pp. 1–149.
- [9] *Introduction to Solid State Physics*, C. Kittel, Wiley: New York, **1996**.
- [10] *Quantum Theory of Solid*, R. E. Peierls, Clarendon, Oxford **1955**.
- [11] J. Yue, A. J. Epstein, *Macromolecules* 1991, 24, 4441; M. S. A. Abdou and S. Holdcraft, in *Handbook of Organic Conductive Molecules and Polymers*, edited by H. S. Nalwa (J. Wiley and Sons, Ltd., West Sussex, England, **1997**) 2, 833.
- [12] W. P. Su, J. R. Schrieffer, A. J. Heeger, *Phys. Rev. Lett.* **1979**, 42, 1698.
- [13] S. A. Brazovskii, *Sov. Phys. JETP Lett.* **1978**, 28, 606.
- [14] M. J. Rice, *Phys. Lett.* **1979**, 71A, 152.
- [15] D. K. Campbell, A. R. Bishop, *Phys. Rev. B* **1981**, 24, 4859.
- [16] A. J. Epstein, J. M. Ginder, F. Zuo, R. W. Bigelow, H.-S. Woo, D.B. Tanner, A. F. Richter, W.-S. Huang, A. G. MacDiarmid, *Synth. Met.* **1987**, 18, 303.
- [17] S. Stafstrom, J. L. Brédas, A. J. Epstein, H. S. Woo, D. B. Tanner, W. S. Huang, A. G. MacDiarmid, *Phys. Rev. Lett.* **1987**, 59, 1474.
- [18] N. J. Pinto, P. D. Shah, P. K. Kahol, B. J. McCormick, *Phys. Rev. B* **1996**, 53, 10690.
- [19] R. S. Kohlman, A. Zibold, D. B. Tanner, G. G. Ihas, Y. G. Min, A. G. MacDiarmid, A. J. Epstein, *Phys. Rev. Lett.* **1997**, 78, 3915.
- [20] M. M. de Kok, M. Buechell, S. I. E. Vulto, P. van de Weijer, E. A. Meulenkaamp, S. H. P. M. de Winter, A. J. G. Mank, H. J. M. Vorstenbosch, C. H. L. Weijtens, V. van Elsbergen, *Phys. Stat. Sol. (A)* **2004**, 201, 1342.
- [21] L. B. Groenendaal, F. Jonas, D. Freitag, H. Pielartzik, J. R. Reynold, *Adv. Mater.* **2000**, 7, 481.

- [22] N. Mott, E. A. Davis, *Electronic Processes in Non-Crystalline Materials*, Clarendon Press, Oxford, **1979**.
- [23] G. Binnig, H. Rohrer, *Rev. Mod. Phys.* **1987**, 59, 615.
- [24] (a) *Multimode™ SPM Instruction Manual*, Version 4.31ce, Digital Instruments-Veeco Metrology Group, **1999**; (b) *Scanning Probe Microscopy Training Notebook*, Version 3.0, Digital Instruments-Veeco Metrology Group, **2000**.
- [25] *Introduction to Scanning Tunneling Microscopy*, C. J. Chen, Oxford University Press, **1993**.
- [26] S. Timpanaro, M. Kemerink, F. J. Touwslager, M. M. de Kok, S. Schrader, *Chem. Phys. Lett.* **2004**, 394, 339.
- [27] G. Binnig, C. F. Quate, Ch. Gerber, *Phys. Rev. Lett.* **1986**, 56, 930.
- [28] T. Muller, Phase Imaging of Polymer Materials with DiCalibrer (AN103), *Veeco Application Notes* at <http://www.veeco.com/pdfs.php/319>
- [29] M. O. Finot, M. T. McDermott, *J. Am. Chem. Soc.* **1997**, 119, 8564.
- [30] M. Kemerink, J. K. J. van Duren, A. J. J. M. van Breemen, J. Wildeman, M. M. Wienk, P. W. M. Blom, H. F. M. Schoo, R. A. J. Janssen, *Macromolecules* **2005**, 38, 7784.
- [31] M. Nonnenmacher, M. P. O' Boyle, H. K. Wickramasinghe, *Appl. Phys. Lett.* **1991** 58, 2921.
- [32] C. W. Tang, S. A. Slyke, *Appl. Phys. Lett.* **1987**, 51, 913.
- [33] J. H. Burroughes, D. D. C. Bradley, A. R. Brown, R. N. Marks, K. Mackey, R. H. Friend, P. L. Burns, A. B. Holmes, *Nature* **1990**, 347, 539.
- [34] W. Brutting, S. Berleb, A. G. Muckl, *Org. Electron.* **2001**, 2, 1.
- [35] R. H. Friend, R. W. Gymer, A. B. Holmes, J. H. Burroughes, R. N. Marks, C. Taliani, D. D. C. Bradley, D. A. dos Santos, J. L. Brédas, M. Logdlund, R. Salaneck, *Nature* **1999**, 397, 121.
- [36] H. Aziz, Z. Popovic, C. P. Tripp, N. Hu, A. Hor, G. Xu, *Appl. Phys. Lett.* **1998**, 72, 2642.
- [37] K. K. Lin, S. J. Chua, S. F. Lim, *J. Appl. Phys.* **2001**, 90, 976.
- [38] S. Gardonio, L. Gregoratti, P. Melpignano, L. Aballe, V. Biondo, R. Zamboni, M. Murgia, S. Caria, M. Kriskinova, *Org. Electron.* **2007**, 8, 37.
- [39] L. J. Rothberg, M. Yan, F. Papadimitrakopoulos, M. E. Galvin, E. W. Kwock, T. M. Miller, *Synth. Met.* **1996**, 80, 41.
- [40] B. H. Cumpston, K. F. J. Jensen, *J. Appl. Polym. Sci.* **1998**, 69, 2451.
- [41] R. F. Bianchi, D. T. Balogh, M. Tirani, R. M. Faria, E. A. Irene, *J. Pol. Science B: Polymer Physics* **2004**, 42, 1033.
- [42] J. S. Lewis, M. S. Weaver, *IEEE Journal of Selected Topics in Quantum Electronics* **2004**, 10, 45.
- [43] G. H. Kim, J. Oh, Y. S. Yang, L. M. Do, K. S. Suh, *Polymers* **2004**, 45, 1879.
- [44] P. E. Burrows, G. L. Graff, M. E. Gross, P. M. Martin, M. K. Shi, M. Hall, E. Mast, C. Bonham, M. B. Sullivan, *Displays* **2001**, 22, 65.

- [45] K. Yamashita, T. Mori, T. Mitzutani, *J. Phys. D: Appl. Phys.* **2001**, 34, 740.
- [46] S. Kho, D. Cho, and D. Jung, *Jpn. J. Appl. Phys.* **2001**, 41, L1336.

Barrier coating for polymer light-emitting diodes using carbon nitride thin films deposited at low temperature by PECVD technique

In this chapter, a plasma-enhanced chemical vapor deposition (PECVD) system was used to deposit carbon nitride at low deposition temperature (<100 °C) to improve the lifetime of polymer light-emitting diodes (PLEDs) and to decrease photo-degradation of MEH-PPV (poly[2-methoxy-5-(2-ethylhexyloxy)-1,4-phenylenevinylene]) in air. The characteristics of the carbon nitride and MEH-PPV films are investigated with FTIR and UV-Visible spectroscopies, with particular emphasis on the degradation process of MEH-PPV under illumination. It was shown by absorbance measurements that the coating protects the polymer film since the damage caused by photo-oxidation diminishes considerably. Current vs. voltage curves for PLEDs also indicated that the protection of a carbon nitride layer enhances the device lifetime.

2.1 Introduction

Thin dielectric films are often used as hermetic seals in integrated circuits and solid-state devices [1,2,3]. Amorphous carbon-nitride alloys ($a\text{-CN}_x$) have been studied as promising candidates for a number of mechanical and electronic applications, such as protective coatings for magnetic disks [4] and electronic materials in cold cathode displays [5,6]. Interest in carbon-nitrogen compounds gained impetus after works in the 1980s [7,8], which predicted excellent mechanical properties for carbon nitrides designed as $\beta\text{-C}_3\text{N}_4$, with a bulk modulus even greater than that for diamond. Indeed, carbon nitride films produced via vapor phase synthesis methods showed low friction and high wear resistance [9,10,11,12,13,14], and proved to be excellent barriers for water and oxygen permeation, analogously to silicon nitride [15]. Nevertheless, carbon nitride films have not been explored as barrier coatings for materials or electronic devices, in which the permeation of water and/or oxygen appears as an obstacle for commercial applications. Polymer light-emitting diodes [16] are devices affected by changes in the chemical structure of the polymers induced upon interaction with the metallic electrodes [17], mainly due to photo-oxidation mechanisms [18]. In particular, oxygen, water and light may cause the electrical field near the polymer-metal interface to vary when a voltage is applied, resulting in local areas of higher electric field that may induce rapid polymer degradation. As a consequence, the lifetime and quantum efficiency of the device will be reduced [18].

In this chapter, a novel application of carbon nitride as a barrier coating for PLEDs is reported. The aim is to minimize degradation of both polymer layer and electrodes due to the presence of oxygen and humidity, which are major factors in decreasing the lifetime of PLEDs. Fourier Transform Infrared Spectroscopy (FTIR) of the carbon nitride layers, UV-Vis Infrared Spectroscopy of the polymer layers in air at different light exposure times were performed as well as $J \times V$ characteristics of the PLEDs were taken at different times.

2.2 Experimental

The polymer light emitting diodes were made in a standard sandwich structure with glass as substrate, polymer on top of an indium tin oxide (ITO) layer and a metal cathode on top of the polymer, as shown in Figure 2.1.

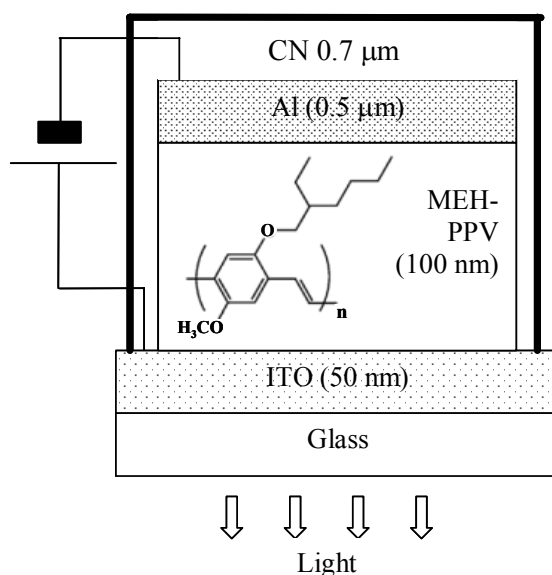


Figure 2.1: Configuration of the polymer light-emitting diode (PLED).

A cleaned glass plate covered by a thin layer of ITO of about 200 nm and $8 \Omega/\square$, transparent and conductive, works as the anode. A polymeric layer, about 100 nm thick MEH-PPV, is deposited through the spreading of a polymeric solution (in chloroform) while the substrate rotates at a speed of 800 rpm, i.e. the spin-coating technique. A $0.5 \mu\text{m}$ thick aluminum (Al) layer was evaporated on the polymeric layer, forming the cathode of the device. Finally, a thin layer of carbon nitride (CN) compound was deposited on top of the PLED by plasma enhanced chemical vapor deposition (PECVD) technique at temperatures close to $100 \text{ }^\circ\text{C}$. PECVD deposition was carried out at 13.56 MHz radio frequency generator and impedance auto-matching network. The deposition parameters are shown in Table 2.I. The substrates were not deliberately heated or cooled during deposition, and the temperature of the substrates rose up to $80 \text{ }^\circ\text{C}$ due to the plasma energy.

Table 2.I: Deposition parameters for carbon nitride films prepared by PECVD.

CH ₄ (sccm)	He (sccm)	N ₂ (sccm)	Pressure (mTorr)	Power density (mW/cm ²)	Temperature (°C)	Time (min)
25	7.5	2.5	15	375	80	120

The device (PLED) was kept under ambient conditions (room temperature, light and humidity) and was characterized by $J \times V$ curves with a HP 4145B semiconductor parameter analyzer at different times. In order to study the effects from photo-oxidation of the polymeric layer, two sets of samples were illuminated with an ELH lamp (100 mW/cm²), up to 10 hours. Illumination was interrupted only for UV-Visible-near IR (UV-Vis/IR) measurements. The experimental setup is shown schematically in Figure 2.2.

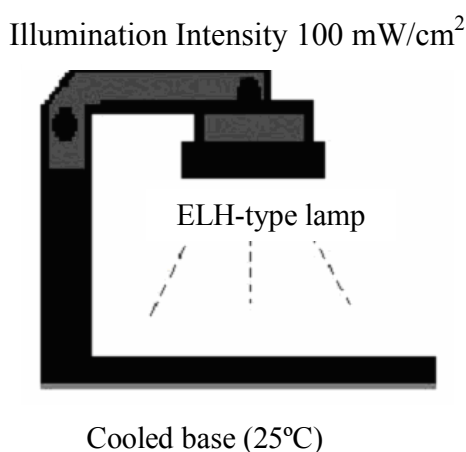


Figure 2.2: Schematic illustration of the illumination system with ELH-type lamp, white light, used for degradation experiments. ELH lamp illumination at 100 mW/cm².

UV-Vis/IR spectroscopy using a Cary spectrophotometer (Varian model 2315) was performed to evaluate the degradation process of the protected (glass/MEH-PPV/carbon nitride) and non-protected (glass/MEH-PPV) polymeric layer. A Fourier-transformed infrared (FTIR) spectrometer (model FTS-40 BIORAD) was employed to analyze the chemical bonding of the carbon nitride films. The samples produced in the system mentioned above were deposited onto p-type (100) single-crystalline silicon substrates in the 7 – 13 Ω.cm resistivity range for FTIR spectroscopy.

2.3 Results and discussions

The main bands related to the carbon nitride structures appear in the infrared spectra in Figure 2.3, viz. C-N ($1020\text{-}1280\text{ cm}^{-1}$), C=N groups ($1610\text{-}1660\text{ cm}^{-1}$), NH bending ($1590\text{-}1640\text{ cm}^{-1}$), NH_2 bending ($1555\text{-}1590\text{ cm}^{-1}$), CH_n bending ($1350\text{-}1450\text{ cm}^{-1}$), C=C bonds ($1300\text{-}1500\text{ cm}^{-1}$), C \equiv N stretching at 2200 cm^{-1} , CH_n stretching at $2800\text{-}3000\text{ cm}^{-1}$ and NH at $3300\text{-}3500\text{ cm}^{-1}$.

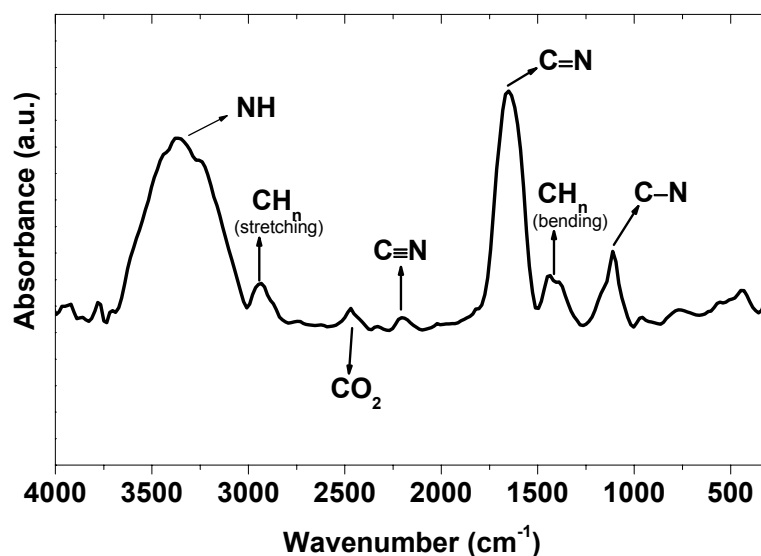


Figure 2.3: FTIR spectra of $0.7\text{ }\mu\text{m}$ thick CN_x films.

These results are consistent with the literature [19,20,21], and with the study of infrared spectra of carbon nitride films [22]. In subsidiary experiments, we varied the thickness of the carbon nitride film and observed that the absorption band assigned to C=N and NH groups decreases with decreasing film thickness. In contrast, the band assigned to C-N increased as the thickness decreased. Because the appearance of C-N bonds is associated with the hardness of carbon nitride, since three-dimensional C_3N_4 with tetrahedral C-N bonds (sp^3 C-N) is comparable to that of diamond, but two-dimensional C_3N_4 is soft [23], the results above indicate that by optimizing the conditions of film fabrication one may control the mechanical properties of the film. This is important for a material used as protection of devices.

Figure 2.4 shows the UV-Vis/IR measurements for the structures glass/MEH-PPV and glass/MEH-PPV/carbon nitride under illumination of ELH-type lamps (100 mW/cm^2) for almost 10 hours, and for the glass/MEH-PPV

structure stored in air and in the dark, up to 6 months. For samples with no protection (glass/MEH-PPV), no changes are observed in the absorption spectra when the polymer film is stored in the dark (Figure 2.4(a)), while the damage occurs very easily in the sample under illumination (Figure 2.4(b)). An intermediate behavior is observed when the glass/MEH-PPV/carbon nitride structure is stored in air, but under illumination (Figure 2.4(c)). In this case, some protection is observed and the drastic damage only occurs after 9 h of illumination. The damage is due to photo-oxidation or photo-degradation of the polymer film, with interaction with the oxygen breaking the polymer chain or interrupting its conjugation, mainly by replacing C=C groups by C=O groups [18,24,25].

Degradation is more clearly visualized in Figure 2.5, where the absorption at 500 nm is plotted against time.

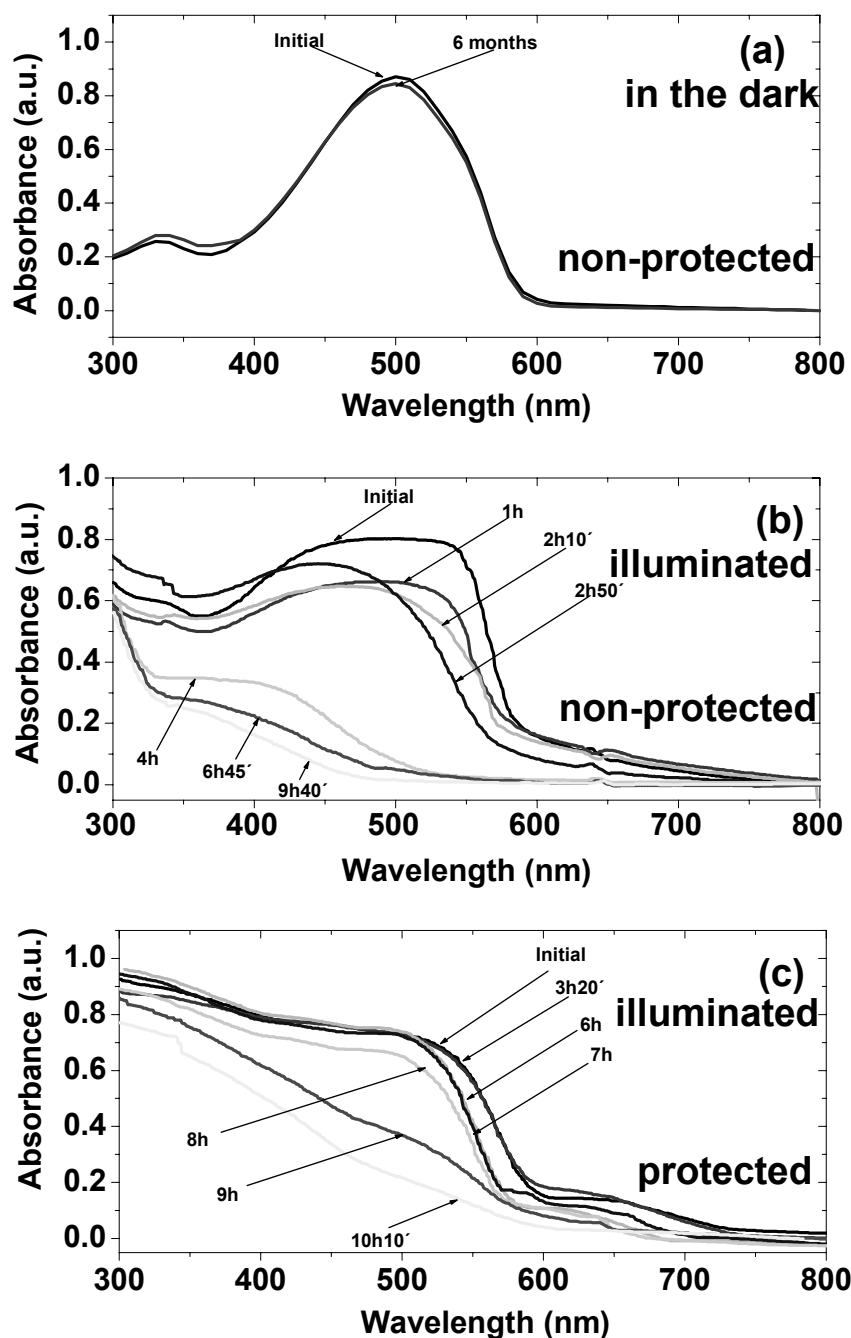


Figure 2.4: UV-Visible measurements for the structures: (a) non-protected (glass/MEH-PPV) in air and dark, (b) non-protected sample (glass/MEH-PPV) under illumination and (c) protected sample (glass/MEH-PPV/carbon nitride) under illumination.

For the sample stored in the dark, even being kept in air, there was no significant change in absorption. For the samples exposed to light, the one with no protective layer displayed a sharp decrease in absorbance in a very short period due to photo-oxidation. In contrast, the sample with a protective layer of carbon nitride only suffered degradation after 6 h of light exposure. These results

are consistent with recent reports in the literature of short lifetimes for MEH-PPV displays [18,24,25].

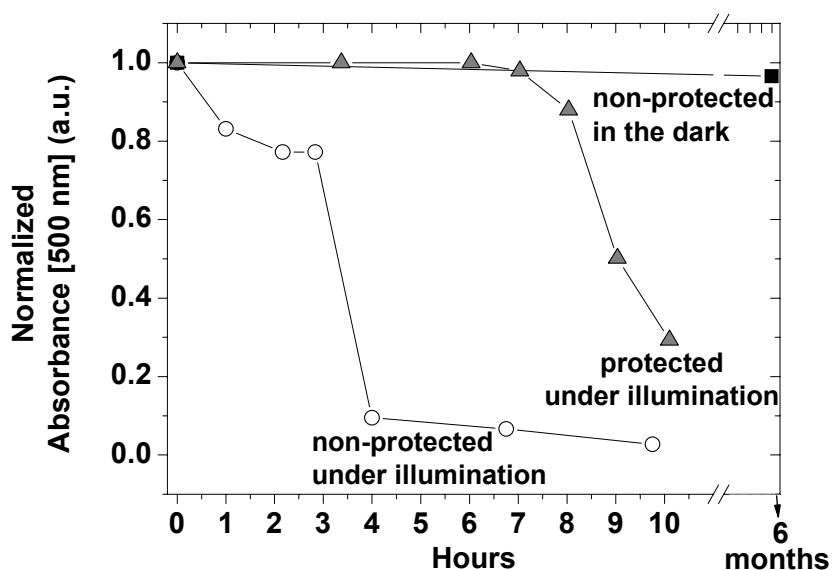


Figure 2.5: Degradation ratio normalized at 500 nm for polymeric layers in the dark and in air, protected with carbon nitride and non-protected.

The most interesting and in fact important aspect of the experiment was to determine if the encapsulation material increased the lifetime of the devices. Figure 2.6 shows $J \times V$ curves for the PLED encapsulated with a carbon nitride film with thickness of $0.7 \mu\text{m}$ and resistivity in the range of $10^{10} \Omega\cdot\text{cm}$. The PLED was kept under ambient conditions of humidity, temperature and light. The shift to higher operational voltages indicates that the device is being degraded when stored for hundreds of days. However, the lifetime of the PLED presented here is much longer than for a non-encapsulated PLED, as the latter works for only a few minutes.

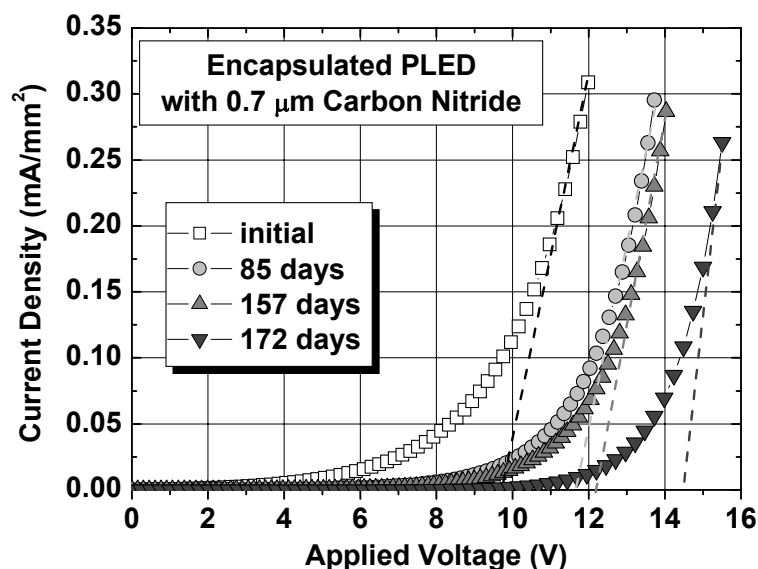


Figure 2.6: Current vs. applied voltage plots for encapsulated PLED as fabricated and at various times after fabrication with the device stored under ambient conditions.

2.4 Conclusions

In this Chapter, we reported a novel use of carbon nitride as encapsulation material for polymer light-emitting polymeric diodes. Carbon nitride meets the criteria for a material that would block humidity and have adequate thickness and flexibility. The lifetime target of >10,000 h for commercial applications is not achieved yet for the PLED. However, optimization of the encapsulation material may be sought by employing films of silicon nitride or other PECVD layer combinations. In addition, optimization of the deposition parameters of the carbon nitride films may be attempted. The experiments with EHL lamp illumination at 100 mW/cm² in air of the PLEDs with no protection indicated that MEH-PPV is easily degraded. In practice, the high photo-oxidation rate of MEH-PPV prevents it from being used in real applications, unless a proper protection is provided for the device.

2.5 References

- [1] H. Nakaue, T. Mitami, H. Kurokawa, T. Yonezawa, H. Yoshio, *Thin Solid Films* **1992**, 212, 240
- [2] A. Grill, V. Patel, B. S. Meyerson, in *Application of Diamond Films and Related Materials*, edited by Y. Tseng, M. Yoshikawa, M. Murakawa, and A. Feldman, Elsevier Science, New York, **1991**, p.686.
- [3] B. Bhushan, J. Ruan, *Surf. Coat. Technol.* **1994**, 68/69, 644.
- [4] L. White, S. S. Bhaia, M. C. Friedenber, S. W. Meeks, C. M. Mate, *Tribology* **1996**, 6, 33.
- [5] G. A. J. Amaratunga, S. R. P. Silva, *Appl. Phys. Lett.* **1996**, 68, 2529.
- [6] N. Conway, C. Godet, B. Equer, in: K. L. Jensen, W. Makie, D. Temple, J. Itoh, R. Nemanich, T. Troitter, P. Holloway (Eds.), Materials Research Society, Pittsburg, PN, San Francisco, *Mater. Res. Soc. Symp. Proc.* **2000**, vol. 621.
- [7] M. L. Cohen, *Phys. Rev. B* **1985**, 32, 7988.
- [8] A. Y. Liu, M. L. Cohen, *Science* **1989**, 245, 841.
- [9] S. Muller, *Sensors and Actuators* **1990**, A21/A23, 1.
- [10] T. A. Yeh, C. L. Lin, J. M. Sivertsen, J. H. Judy, *J. Magn. & Magn. Mater.* **1993**, 120, 314.
- [11] E. C. Cutiongco, D. Li, Y. W. Chung, C. S. Bhatia, *Trans. ASME* **1996**, 118, 543.
- [12] S. Miyake, S. Watanabe, H. Miyazawa, M. Murakawa, R. Kaneko, T. Miyamoto, *Appl. Phys. Lett.* **1994**, 65, 3206.
- [13] A. Czyzniewski, W. Precht, M. Pancielejko, P. Myslinski, W. Walkowiak, *Thin Solid Films* **1998**, 317, 384.
- [14] S. Watanabe, S. Miyake, M. Murakawa, *Proceedings of the 6th Applied Diamond Conference/2nd Frontier Carbon Tech. (ADC/FCT2001)* **2001**, p. 599.
- [15] R. M. Kubacki, *IEEE Trans. Compon. Packging Manuf. Technol, Part A* **1995**, 18, 3.
- [16] M. Pope, C. E. Swenberg, *Electronic Process in Organic Crystals and Polymers*, 2nd ed., Oxford University Press, **1999**.
- [17] W. Fahlman, W. R. Salaneck, *Surf. Sci.* **2002**, 500, 902.
- [18] R. F. Bianchi, D. T. Balogh, M. Tinani, R. M. Faria, E. A. Irene, *J. Pol. Science B: Polymer Physics* **2004**, 2, 1033.
- [19] J. M. Méndez, A. Gaona-Couto, E. Andrade, J. C. Pineda, E. P. Zavala, S. Muhl, *Nucl. Instrum. Methods Phys. Res., B Beam Interact. Mater. Atoms* **1998**, 136–138, 231.
- [20] J. Ju, Y. Xia, W. Zang, L. Wang, D. Tang, *J. Non-Cryst. Solids* **2000**, 278, 213.
- [21] Y. Togashi, Y. Hirohata, T. Hino, *Vacuum* **2002**, 66, 391.
- [22] S. E. Rodil, A.C. Ferrari, J. Robertson, S. Muhl, *Thin Solid Films* **2002**, 420–421, 122.
- [23] D. M. Teter, R. Hemley, *Sci.* **1996**, 53, 271.
- [24] B. H. Cumpston, K. F. J. Jensen, *J. Appl. Polym. Sci.* **1998**, 69, 2451.

- [25] R. F. Bianchi, D. T. Balogh, D. Goncalves, R. M. Faria, E. A. Irene, *Mol. Cryst. Liq. Cryst.* **2002**, 374, 457.

Microscopic Understanding of the Anisotropic Conductivity of PEDOT:PSS Thin Films: a qualitative study

In this chapter, the dc conductivity of commercial and specially synthesized batches of PEDOT:PSS has been studied as a function of temperature in the range from 77 K to 300 K. Electrical measurements of the dc conductivity were performed in top-bottom (normal) and coplanar (lateral) contact geometries. Depending on temperature, differences between the normal and lateral conductivity of up to three orders of magnitude were found. This shows that the spin coated material is highly anisotropic, which may cause an enhanced cross-talk between neighboring pixels in organic displays. The temperature dependence was found to follow $\sigma = \sigma_0 \exp[-(T_0/T)^\alpha]$, with the characteristic temperature T_0 , the exponent α and the prefactor σ_0 all dependent on the direction of the current. The physical reason for this unexpected behavior is the microscopic morphology of spin cast films. From low-current scanning tunneling microscopy images, it is found that the films consist of flattened PEDOT-rich particles embedded in a PSS-rich matrix of low conductivity. By performing phase-sensitive atomic force microscopy on cryogenically cleaved samples a cross-sectional view of the morphology was obtained. From this, it was found that the PEDOT-rich particles are actually organized in layers that are separated by quasi-continuous nm-thick PSS lamellas. In the normal direction, the PSS lamellas enforce nearest-neighbor hopping between the quasi-metallic PSS particles, leading to a strongly reduced conductivity and a temperature exponent $\alpha = 1$, both in agreement with experiment. The exponent $\alpha = 1/4$ that is observed for lateral transport is attributed to variable-range hopping between the PEDOT-rich particles.

3.1 Introduction

Conjugated polymers combine the advantageous characteristics of conventional polymers, such as low weight, processability, and flexibility, with the functional physical properties of conventional semiconductors, such as absorption and emission of light and a tunable conductivity, to provide innovative materials for (opto)electronic devices. In polymer light-emitting diodes, solar cells, memory storage devices, and field-effect transistors, as well as in other high-volume, low-cost applications of plastic electronics, there is a need for polymers with high conductivity to act as charge transport layer or electrical interconnect. In the large majority of devices, this role is played by poly(3,4-ethylenedioxythiophene):poly(styrenesulfonate) (PEDOT:PSS), a blend of an oxidatively doped, cationic, conducting polythiophene derivative (PEDOT) that is electrostatically bound to a PSS polyanion [1]. PEDOT:PSS combines high conductivity and good transparency in the visible region with excellent stability under ambient conditions and can be easily processed from aqueous dispersions by spin coating.

A common feature of conducting and semiconducting π -conjugated polymers is the strong influence of morphology and, hence, processing conditions on the material properties. This subject has been extensively investigated for semiconducting polymers [2]. Despite the ubiquitous use of PEDOT:PSS, relatively little attention has been given to the basics of the charge transport in this material [3,4]. The lateral conductivity of PEDOT:PSS blends has been addressed for various compositions with variation of pH [3], solvents [5], and water content [6]. From the observed temperature dependence, it was concluded that lateral electric conductivity occurs via hopping of charge carriers. However, a detailed understanding of the role of the morphology in this process is currently lacking. Moreover, possible anisotropies in the conductivity have not been systematically addressed, despite the observed anisotropy in the optical response [7]. A recent conductive atomic force microscopy (AFM) experiment on 1 μm thick drop-cast PEDOT:PSS films suggests that the charge transport perpendicular to the substrate is dominated by space-charge effects, in striking contrast to the transport parallel to the substrate [4]. For the use in pixelated displays, the issue of in- versus out-of-plane anisotropy is of utmost importance since in-plane

conductivity causes crosstalk between neighboring pixels, whereas the out-of-plane conductivity has a direct effect on the contact resistance.

The currently accepted morphology of spin-cast PEDOT:PSS films is that of a phase segregated material consisting of PEDOT:PSS grains surrounded by a shell formed by excess PSS [8]. The thickness of the grain boundary has been found to be about 30–40 Å [9,10]. The PEDOT-rich core of the grains has a much higher intrinsic conductivity than the PEDOT-depleted grain boundary, which is essentially insulating because PSS is only a weak ionic conductor. Consequently, the main obstacle is to transport electric current between the PEDOT-rich grains [3,11], while the electronic current is easily transported within the grains. Although this description rationalizes some of the properties of PEDOT:PSS thin films, a detailed and consistent correlation between morphology and electrical properties has not yet been established.

In the present study we combine scanning probe microscopy with macroscopic conductivity measurements to come to a full 3D morphological model that explains the observed anisotropic conductivity of spin coated PEDOT:PSS thin films. In particular, we find that the vertical conductivity, that is, perpendicular to the substrate, can be up to three orders of magnitude lower than the lateral conductivity in the plane of the film. Observation of pancake-shaped PEDOT-rich islands separated by lamellas of PSS in cross-sectional AFM and topographic scanning tunneling microscopy (STM) images explains not only the large difference in conductivity, but also the difference in the conduction mechanism as observed in temperature-dependent conductivity measurements. Despite apparent ordering of PEDOT-rich islands in STM images, the macroscopic in-plane conductivity was found to be totally isotropic, and the ordering was concluded to be confined to randomly oriented micrometer-size domains.

3.2 Experimental

Two PEDOT:PSS (1:6 by weight) materials were used in this work. One was purchased from H. C. Starck with the trade name Baytron P (Baytron P VP Al 4083), and the other was synthesized at TNO Science and Industry laboratories,

in Eindhoven, as follows. 3,4-Ethylenedioxythiophene (EDOT) and sodium persulfate ($\text{Na}_2\text{S}_2\text{O}_8$, Aldrich) were used as received. 16.5 g of sodium polystyrenesulfonate (NaPSS) (Aldrich, weight-average molecular weight $M_w = 200 \text{ kg mol}^{-1}$) was dissolved in ca. 200 mL ultrapure water (UPW, Millipore $> 17.5 \text{ M}\Omega\cdot\text{cm}$) and purified to remove low molecular weight impurities by repetitive dialysis against UPW using a Spectropor tube (molecular weight cut-off: 6–8 kDa). Afterwards the solution was concentrated to the original quantity of ca. 200 mL and dried by freeze drying using a Labconco FreeZone 4.5 freeze dry system. 11.4 g of NaPSS was obtained as a white powder with a size exclusion chromatography (SEC) M_w of 200 kg mol^{-1} . Then, to a stirred mixture of 1.68 g (8.1 mmol) NaPSS, 0.26 g (1.8 mmol) EDOT in 127 mL UPW was added 8.1 g (8.1 mmol) 1M HCl (aq) in one portion. The reaction flask was covered with aluminum foil. After 15 min, 0.55 g (2.3 mmol) $\text{Na}_2\text{S}_2\text{O}_8$ was added as a solid. The mixture was allowed to stir for 16 h. Subsequently, the mixture was purified by repetitive dialysis against acidic UPW (40 mM HCl) and UPW respectively using the Spectropor tube as mentioned before. The resulting PEDOT:PSS was concentrated until ca. 3.1 wt% solid content, containing only 15 ppm Na^+ ions as determined by ion chromatography. Baytron P contains about 300 ppm Na^+ using the same method.

The substrates consisted of $3 \times 3 \text{ cm}^2$ bare sodalime glass. They were first grooved into small pieces of $1 \times 1 \text{ cm}^2$ on the back side with a diamond pen, then cleaned with soap and subsequently sonicated in baths of acetone and isopropanol for 20 min each and rinsed with deionized water after each process. Residual organic contaminations were removed using a 30 min. UV-ozone treatment (UV-Ozone Photoreactor, PR-100, Ultraviolet Products).

For the in-plane electrical measurements (\parallel), four electrodes ($1 \times 6 \text{ mm}$, 1 mm apart from each other) of 5 nm of chromium followed by 95 nm of gold were evaporated on top of cleaned bare-glass substrates (see also the inset of Figure 3.1(a)). For the out-of-plane electrical measurements (\perp) 100 nm of gold was evaporated on top of a small area of ITO to eliminate the spurious series resistance caused by the ITO (see also the inset of Figure 3.1(b)).

The PEDOT:PSS solutions were filtered using a $5 \mu\text{m}$ filter and deposited in air by spin-coating for both types of electrode geometries. Then, samples were transferred into a glove box (O_2 and $\text{H}_2\text{O} < 1 \text{ ppm}$) and subsequently annealed on

a hot plate at 200 °C for 2 min to remove water. The thicknesses were about 60 and 95 nm for Baytron P and for the low-Na⁺ PEDOT:PSS, respectively, as measured by a profilometer (Alpha-step 200, Tencor Instruments). The remaining top contact for \perp electrode geometry samples were made by the evaporation of 100 nm of gold on top of PEDOT:PSS thin films using a shadow mask which gives an active area of 0.35 cm². After cutting the desired sample from the substrate, it was placed inside a cryostat (Oxford Instruments), evacuated to 10⁻⁵ mbar (1 bar = 100 kPa) and brought to the desired temperature in the 77–300 K range. Temperature control was provided by an Oxford ITC 601 temperature controller that maintained temperature stability within ± 0.1 K. Conductivities were measured by a Keithley source meter (model 2410). For all temperature-dependent measurements the electrical connections were made inside the glove box, so the measured samples never experienced contact with air after bake-out. From a comparison of two- and four-terminal measurements, the contact resistance was found to be negligible for all our samples.

Scanning tunneling microscopy (STM) experiments were measured with a Veeco/Digital Instruments MultiMode equipped with a low-current STM unit, driven by a NanoScope IV controller. For the STM measurements, freshly cut Pt-Ir tips were used and the experiments were conducted in air. Tapping mode cross-sectional atomic force microscopy (X-AFM) experiments were measured with a Veeco/Digital Instruments Dimension 3100, driven by a NanoScope IIIA controller. For the X-AFM measurements, 3 cm \times 3 cm PEDOT:PSS thin films on glass were frozen at liquid nitrogen temperature and then broken into small pieces. The tips (NCH-R from Nanosensors) used in this experiment had a spring constant $k \approx 40$ N/m.

3.3 Results and discussions

We investigated two types of PEDOT:PSS, both with a mass ratio of 1:6. One was Baytron P VP AI 4083 from H. C. Starck,[12] which contains roughly 300 ppm Na⁺. In order to make sure that intrinsic properties of PEDOT:PSS were measured, the second material was an ultrapure (15 ppm Na⁺) PEDOT:PSS that was specifically synthesized for this purpose as described in the experimental

section. For the electrical characterization, the samples were designed to have different electrode geometries so that applied electric field is either parallel (\parallel) or perpendicular (\perp) to the surface normal (see insets of Figure 3.1).

3.3.1 Temperature dependence of the electrical conductivity

The temperature-dependent conductivity [$\sigma(T)$] of spin coated PEDOT:PSS thin films is presented in Figure 3.1 for the temperature range from 77–300 K, measured in \parallel and \perp directions.

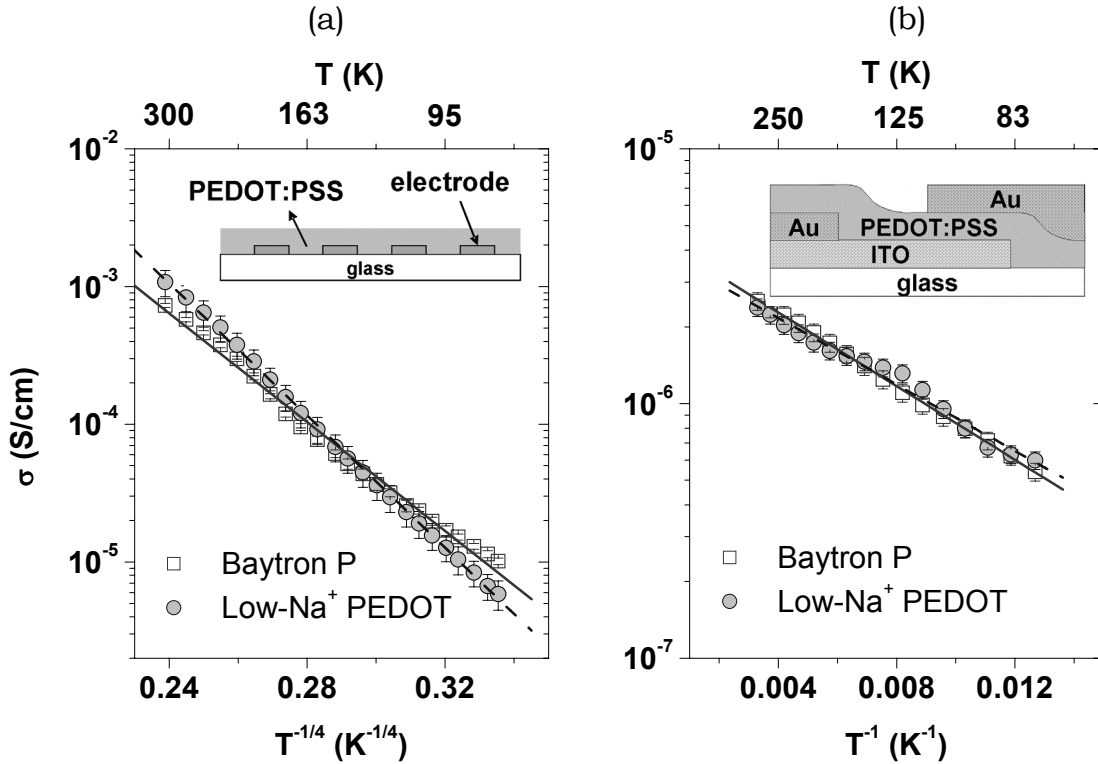


Figure 3.1: Temperature dependence of the dc conductivity of spin-coated PEDOT:PSS thin films of Baytron P and low- Na^+ PEDOT-PPS. Points are experimental data and lines are fits to Eq 3.1. (a) The electric field is applied parallel (\parallel) to the substrate, $\alpha_{\parallel} = 1/4$ and T_0 values are 4.3×10^6 K and 9.4×10^6 K for Baytron P and low- Na^+ PEDOT:PSS, respectively. (b) The electric field is applied perpendicular (\perp) to the substrate $\alpha_{\perp} = 1$ and E_3 is about 14 meV for both polymers. Note the different exponents on the horizontal axis, see main text for further explanation.

For both directions (\parallel and \perp), $\sigma(T)$ can be described by

$$\sigma(T) = \sigma_0 \exp \left[- \left(\frac{T_0}{T} \right)^\alpha \right] \quad \text{Eq 3.1}$$

where σ_0 is the conductivity prefactor, T_0 the characteristic temperature, and α an exponent that is related to the transport process [13,14].

Two remarkable features can be seen in Figure 3.1. First, the qualitatively different temperature dependence of α , as indicated by the different values of α for \parallel and \perp directions, and, second, the large difference in the magnitude of σ . The origin for these remarkable differences lays in the particular morphology of PEDOT:PSS films, as will be discussed below.

The value of $1/4$ for α that is observed in the \parallel direction (Figure 3.1(a)) can be interpreted in terms of a variable-range hopping (VRH) model. In the usual analysis of VRH, the exponent α equals $1/(1+D)$, where D is the dimensionality of the electrical conduction path. Hence $\alpha = 1/4$ indicates 3D variable-range hopping. For $\alpha = 1/4$, T_0 is connected to the density of states at the Fermi level $N(E_F)$ via $T_0 = \beta / N(E_F) \xi^3 k_B$ where ξ is the localization length, $\beta (= 21.2)$ a numerical factor and k_B the Boltzmann constant. The similarity in slope of $\sigma(T)$ versus $T^{-1/4}$, represented by T_0 , for the two types of polymers suggests that the morphology in the \parallel direction is basically the same. Moreover, the small difference in σ_0 between the two materials, 1.6 S/cm and 2.7 S/cm for Baytron P and low- Na^+ PEDOT, respectively, indicates that the conductivity is not significantly influenced by background impurities, being mainly Na^+ ions.

The simple Arrhenius, thermally activated process ($\alpha = 1$) observed for the \perp direction (Figure 3.1(b)) obviously cannot be attributed to a VRH process. Rather, it indicates a nearest-neighbor hopping (nn-H) type behavior [13,14]. In this case, the parameter T_0 represents the activation energy $E_3 \approx 1/N(E_F) a^3 k_B$, where a is the average inter-site distance, according to $T_0 = E_3/k_B$. As in the former case (\parallel direction), the morphology in the \perp direction seems to be the same for both materials, since the T_0 values are quite close.

3.3.2 Morphology

In order to elucidate the different electrical behavior in the \parallel and \perp directions, we studied the morphology using scanning probe techniques. Because of the presence of a thin (few nanometers) PSS-rich top layer [8] we hardly see meaningful features on topographic AFM images (not shown). Using STM with a relatively large setpoint current, this layer is not seen [15], and the bulk morphology becomes visible [16]. The $200 \text{ nm} \times 200 \text{ nm}$ STM image in Figure 3.2(a) shows that the PEDOT:PSS films indeed have a granular morphology, with a typical grain size of about 20–25 nm. The low surface roughness of approximately 1.75 nm implies that the grains actually have the shape of flattened balls, or pancake-like structures. This is further corroborated in the inset of Figure 3.2(a). The transformation of spherical particles in solution to pancakes in thin films is most likely the result of the spin casting procedure, during which the evaporating water causes the thickness to shrink while the film remains continuous in the lateral direction.

Figure 3.2(b) shows a $200 \text{ nm} \times 200 \text{ nm}$ tapping mode AFM (TM-AFM) phase image of the cross section of a PEDOT:PSS film which is exposed by cleaving the sample at 77 K. The cross-sectional AFM (X-AFM) image shows quasi-continuous elongated domain structures of darker and brighter color, having similar sizes as the particles in Figure 3.2(a). Since the TM-AFM phase image is sensitive to dissipation in the tip–surface interaction, and therefore to the material composition [17], the presence of multiple phases in a blend, in this case PEDOT:PSS, generally leads to a phase contrast in the TM-AFM.

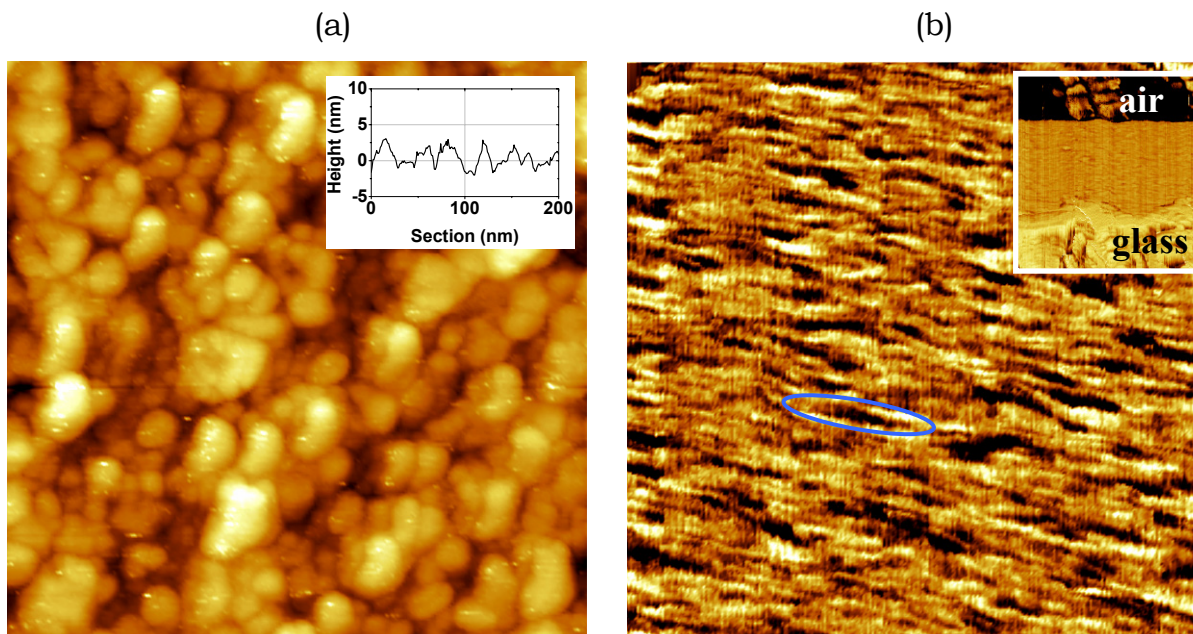


Figure 3.2: (a) 200 nm \times 200 nm topographic STM image of PEDOT:PSS on indium tin oxide (ITO) at 2.3 V, tunneling current 10 pA, and vertical scale 15 nm, the inset shows a line section. (b) 200 nm \times 200 nm cross-sectional AFM phase image of cleaved PEDOT:PSS on glass, vertical scale is 8°. The glass substrate is on the bottom side of the image, as shown by the inset of 530 nm \times 580 nm and vertical scale 70°. A pancake-like particle is highlighted by the ellipse.

Therefore, dark and bright features in the X-AFM images are interpreted as PEDOT-rich and PSS-rich regions, respectively. With this in mind, Figure 3.2(b) can be interpreted as a side view of PEDOT-rich “*pancakes*” with a thickness of a few nanometers and a diameter of a few tens of nanometers separated by PSS lamellas. In the normal direction, the separating barriers, that is, the PSS lamellas are quasi-continuous, whereas the separations in the lateral direction do not seem to be fully closed. Clearly, a top view of these lasagna-like structures should look like Figure 3.2(a). Moreover, this lasagna-type morphology is fully consistent with the lamellar structure proposed previously [4]. These STM and X-AFM measurements can be combined into the schematic morphological model depicted in Figure 3.3.

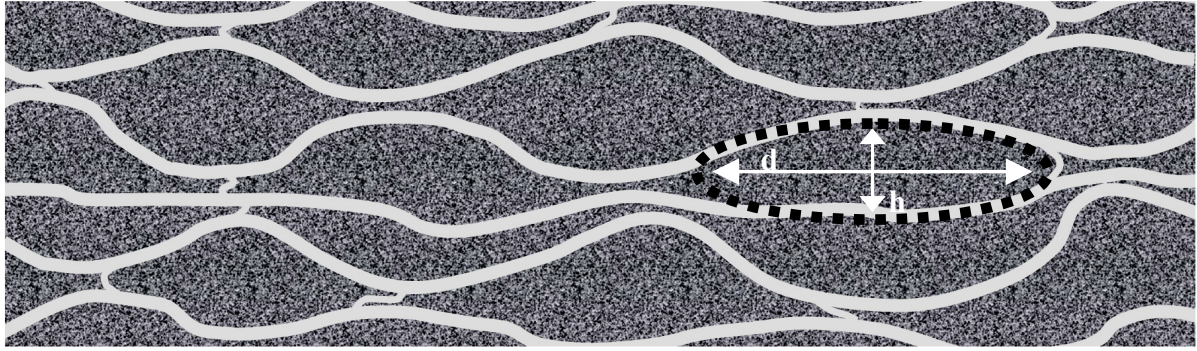


Figure 3.3: Cross-sectional view of the schematic morphological model for PEDOT:PSS thin films derived from combined STM and X-AFM measurements. PEDOT-rich clusters (dark) are separated by lamellas of PSS (bright). The PEDOT-rich lamella is composed of several pancake-like particles as pictured by the dotted lines. The typical diameter d of the particles is about 20–25 nm and the height h is about 5–6 nm.

Now, the differences in electrical transport properties in the \parallel and \perp directions can be understood. In the \parallel direction, that is, within the PEDOT-rich lamella, conduction can take place by 3D VRH because in this direction the PEDOT-rich domains are only separated by the not-completely closed constrictions. These are likely to either form a thin barrier, or no barrier at all, thereby allowing carriers to hop to non-nearest-neighbor sites. Moreover, the absence of thick barriers in the conduction path will lead to relatively high σ values (i.e. 10^{-3} S/cm at room temperature). In the \perp direction, the PEDOT-rich domains are separated by thick barriers, formed by the PSS lamella, which enforce nearest-neighbor hopping and cause a reduction of σ (i.e. 2×10^{-6} S/cm at room temperature). In a hopping system, an increase in barrier thickness has a similar effect as an increase in temperature in the sense that it promotes nearest-neighbor hopping [13]. A transition to a VRH regime at low T , however, was not observed in the investigated temperature regime.

In the view of the above results, one may anticipate similar anisotropy in layer-by-layer films of conducting polymers [18].

3.3.3 In-plane anisotropy

A striking feature that is often observed [16] on small-scale STM images is a pronounced alignment of the PEDOT-rich domains (see Figure 3.4(b) and (c)). Such alignment could easily result from the centrosymmetric forces in the spin

coating process and would likely cause in-plane anisotropy in the electrical properties of the resulting film.

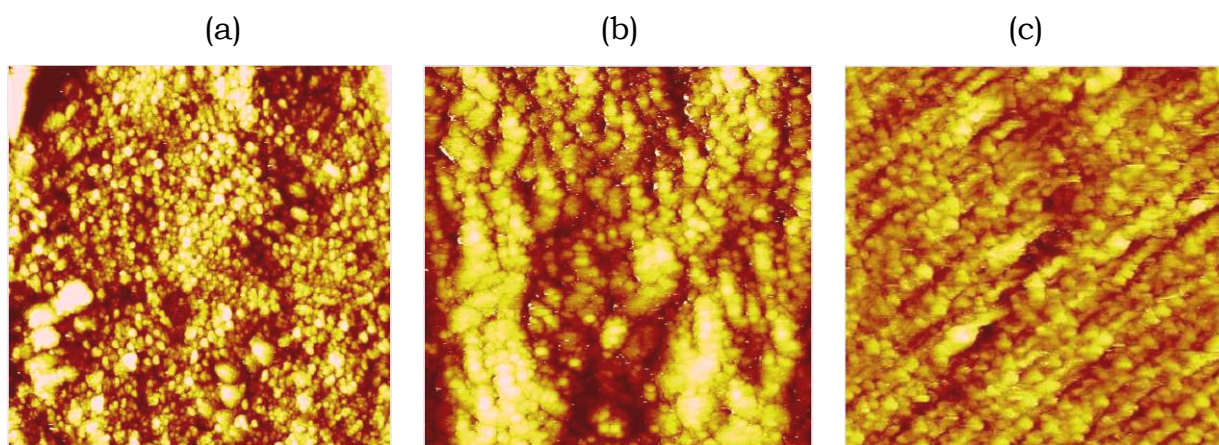


Figure 3.4: Topographic STM images of low- Na^+ PEDOT:PSS on ITO. (a) $1 \mu\text{m} \times 1 \mu\text{m}$; (b) $500 \text{ nm} \times 500 \text{ nm}$, (c) as for (b), for Baytron P. For all images, the tunneling current was 10 pA, bias 2.3 V, and vertical scale 10 nm.

On larger scale images like Figure 3.4(a), a unidirectional alignment is not always clearly observable. Moreover, no statistically relevant correlation was found between the alignment direction and the position on the $3 \text{ cm} \times 3 \text{ cm}$ substrate that was used for spin coating. In order to shed further light on the alignment issue, the conductivity was measured in different in-plane directions. For this, a shadow mask as depicted in Figure 3.5(a) was made. It allows σ to be probed in different orthogonal directions on equivalent positions on the substrate. The results of the measurements are shown in Figure 3.5(b).

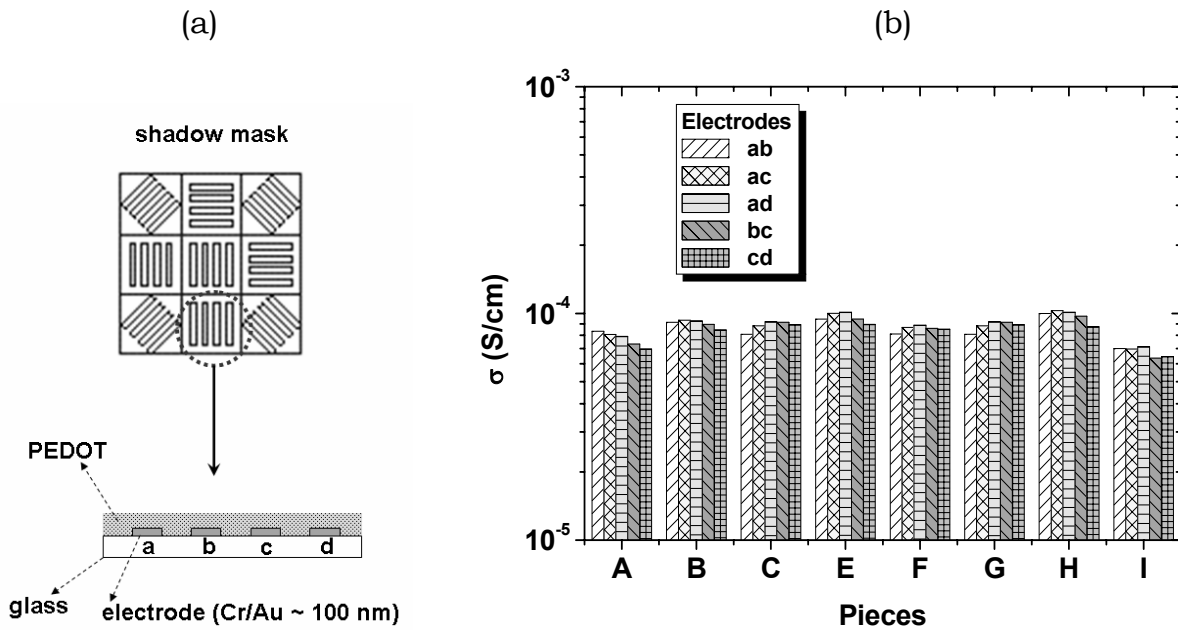


Figure 3.5: (a) Layout of the shadow mask used to evaporate Cr/Au electrodes for in-plane electrical measurements (top) and schematic side view of the samples (bottom). Samples are labeled A–I from top left to right bottom. (b) Typical conductivity of eight pieces of a 3 cm \times 3 cm PEDOT:PSS sample, measured in air (piece D was left out). Capital letters indicate the piece, and the small letters indicate the pair of electrodes used in the 2-point measurements. 4-point measurements yielded identical results. The average conductivity is $(8.5 \pm 0.7) \times 10^{-5}$ S/cm.

Figure 3.5(b) shows that the spin coated films of PEDOT:PSS form a reasonably homogeneous material in terms of electrical conductivity. Moreover, in multiple data sets, no correlation between the electrode alignment and the conductivity was found. From this and from larger scale topographic images (Figure 3.4(a)) we conclude that the observed alignment of PEDOT-rich domains is most likely confined to randomly oriented sub-micrometer-sized domains. Note, also, that the average σ in Figure 3.5(b) is about one order of magnitude lower than of that in Figure 3.1(a) at room temperature. Because the measurements of Figure 3.5(b) were performed in air and PEDOT:PSS films are hygroscopic, such differences are due to rapid water uptake [6]. Further studies on the influence of water and post-treatments on the σ of PEDOT:PSS is discussed in Chapter 5.

3.4 Conclusions

The conductivity of PEDOT:PSS thin films is studied by temperature-dependent conductivity measurements in the perpendicular and lateral directions with respect to the substrate surface. The surprising anisotropy, both in conductivity magnitude and in the conduction mechanism could successfully be correlated to a detailed morphological model that was derived from topographic STM and cross-sectional AFM images. The spin coated material was found to consist of horizontal layers of flattened PEDOT-rich particles that are separated by quasi continuous PSS lamella. An apparent in-plane alignment of PEDOT-rich domains was found to be confined to randomly oriented, submicrometer-sized domains, and did not lead to an observable anisotropy in the in-plane conductivity.

3.5 References and notes

- [1] For a review on PEDOT see for example, a) L. B. Groenendaal, F. Jonas, D. Freitag, H. Pielartzik, J. R. Reynolds, *Adv. Mater.* **2000**, *12*, 481. b) S. Kirchmeyer, K. Reuter, *J. Mater. Chem.* **2005**, *15*, 2077.
- [2] a) H. Sirringhaus, P. J. Brown, R. H. Friend, M. M. Nielsen, K. Bechgaard, B. M. W. Langeveld-Voss, A. J. H. Spiering, R. A. J. Janssen, E. W. Meijer, P. Herwig, D. M. de Leeuw, *Nature* **1999**, *401*, 685. b) B. J. Schwartz, *Annu. Rev. Phys. Chem.* **2003**, *54*, 141. c) M. Kemerink, J. K. J. van Duren, P. Jonkheijm, W. F. Pasveer, P. M. Koenraad, R. A. J. Janssen, H. W. M. Salemink, J. H. Wolter, *Nano Lett.* **2003**, *3*, 1191.
- [3] a) A. N. Aleshin, S. R. Williams, A. J. Heeger, *Synth. Met.* **1998**, *94*, 173. b) T. P. Nguyen, S. A. de Vos, *Appl. Surf. Sci.* **2004**, *221*, 330.
- [4] C. Ionescu-Zanetti, A. Mechler, S. A. Carter, R. Lal, *Adv. Mater.* **2004**, *16*, 385.
- [5] a) T. Y. Kim, J. E. Kim, K. S. Suh, *Polym. Int.* **2006**, *55*, 80. b) J. Quyang, Q. Xu, C.-W. Chu, Y. Yang, G. Li, J. Shinar, *Polymer* **2004**, *45*, 8443.
- [6] J. Huang, P. F. Miller, J. S. Wilson, A. J. de Mello, J. C. de Mello, D. D. C. Bradley, *Adv. Funct. Mater.* **2005**, *15*, 290.
- [7] L. A. A. Pettersson, F. Carlsson, O. Inganäs, H. Arwin, *Thin Solid Films* **1998**, *313-314*, 356.
- [8] a) X. Crispin, S. Marciniak, W. Osikowicz, G. Zotti, A. W. Denier van der Gon, F. Louwet, M. Fahlman, L. Groenendaal, F. de Schryver, W. R. Salaneck, *J. Polym. Sci. Part B: Polym. Phys.* **2003**, *41*, 2561. b) A. M. Higgins, S. J. Martin, P. C. Jukes, M. Geoghegan, R. A. L. Jones, S. Langridge, R. Cubitt, S. Kirchmeyer, A. Wehrum, I. Grizzi, *J. Mater. Chem.* **2003**, *13*, 2814.
- [9] G. Greczynski, T. Kugler, M. Keil, W. Osikowicz, M. Fahlman, W. R. Salaneck, *J. Electron Spectrosc. Relat. Phenom.* **2001**, *121*, 1.
- [10] J. Hwang, F. Amy, A. Kahn, *Org. Electron.* **2006**, *7*, 387.
- [11] L. Zuppiroli, M. N. Bussac, S. Paschen, O. Chauvet, L. Forro, *Phys. Rev. B* **1994**, *50*, 5196.
- [12] H. C. Starck, <http://www.baytron.com>.
- [13] N. Mott, E. A. Davis, *Electronic Processes in Non-Crystalline Materials*, Clarendon, Oxford **1979**.
- [14] B. I. Shklovskii, A. L. Efros, *Electronic Properties of Disordered Semiconductors*, Springer, Berlin **1984**.
- [15] Unlike AFM, STM topography reflects a surface of equal conductivity, which, in low-conductivity materials, does not necessarily coincide with the sample surface. The current setpoint and bias used in this work, 10 pA and 2.3 V, respectively, were enough to penetrate the insulating PSS-rich surface layer, while maintaining stable imaging of the deeper, more conducting bulk layers. See S. Timpanaro *et al.* [16] for more details.
- [16] S. Timpanaro, M. Kemerink, F. J. Touwslager, M. M. de Kok, S. Schrader, *Chem. Phys. Lett.* **2004**, *394*, 339.
- [17] a) J. P. Cleveland, B. Anczykowski, A. E. Schmid, V. B. Elings, *Appl. Phys. Lett.* **1998**, *72*, 2613. b) D. Raghavan, M. VanLandingham, X. Gu, T. Nguyen, *Langmuir* **2000**, *16*, 9448.

- c) X. Crispin, F. L. E. Jakobsson, A. Crispin, P. C. M. Grim, P. Anderson, A. Volodin, M. Van der Auweraer, W. R. Salaneck, M. Berggren, *Chem. Mater.* **2006**, 18, 4354.
- [18] a) V. Zucolotto, M. Ferreira, M. R. Cordeiro, C. J. L. Constantino, D. T. Balogh, A. R. Zanatta, W. C. Moreira, O. N. Oliveira Jr., *J. Phys. Chem. B* **2003**, 107, 3733. b) F. T-Strixino, E. C. Pereira, S. V. Mello, O. N. Oliveira Jr., *Langmuir* **2004**, 20, 3740. c) B. S. Shim, Z. Tang, M. P. Morabito, A. Agarwal, H. Hong, N. A. Kotov, *Chem. Mater.* **2007**, 19.

Anisotropic hopping conduction in spin-coated PEDOT:PSS thin films: a quantitative study

This is an extension of the previous Chapter. Here, the charge transport in spin coated poly(3,4-ethylenedioxythiophene):poly(styrenesulfonate) [PEDOT:PSS] has been investigated as a function of temperature and electric field. Both the magnitude and the transport mechanism are found to be strongly anisotropic. This striking behavior is quantitatively explained in terms of a morphological model in which flattened, quasi-metallic PEDOT-rich grains are organized in horizontal layers that are separated by continuous insulating PSS lamellas. In this model, the in-plane conductivity is described by 3D variable-range hopping between ~ 25 nm sized PEDOT-rich particles separated by sub-nm PSS barriers, while the out-of-plane conductivity is described by nearest-neighbor hopping between more widely spaced molecular sites. These length scales are supported by previously reported scanning probe measurements in Chapter 3.

4.1 Introduction

Conducting polymers offer a unique combination of properties that make them attractive materials for many electronic applications. Typically, these polymers are made conducting by chemical doping, resulting in polycations or polyanions with a relatively mobile charge [1]. The conductivity of these materials can be tuned by, amongst others, chemical manipulation of the polymer backbone, the nature of the dopant, the degree of doping, and by blending with other polymers.

Poly(3,4-ethylenedioxythiophene) blended with poly(4-styrenesulfonic acid) (PEDOT:PSS) is one of the most important and successful conducting polymers synthesized in the field of organic electronics [2]. Combining a relatively high conductivity [3] with optical transparency in the doped state it is suitable for applications such as antistatic coatings [4], electrode in light-emitting diodes [5], photovoltaics [6], memories [7], sensors [8] and as active material for electrochromic devices [9]. As such, PEDOT:PSS has found application in basically all organic/polymeric devices. Even though there is extensive commercial and scientific interest in PEDOT:PSS, the nature of the charge transport is still not clear. In addition, the correlation between the morphology and the conductive properties is incompletely understood and has been addressed in a limited number of publications [10,11,12,13,14,15].

Despite large differences in interpretation and experimental data, it is generally believed that charge transport in PEDOT:PSS occurs by a hopping process. Typically, the resulting conductivity σ can be described by

$$\sigma(T) = \sigma_0 \exp\left[-\left(\frac{T_0}{T}\right)^\alpha\right] \quad \text{Eq 4.1}$$

where T_0 is a material-dependent parameter, and the exponent $\alpha = 1/(1+D)$ is taken as the signature of variable-range hopping (VRH) [16] in D dimensions. Alternatively, an exponent close to 1/2 can result from the effects of either Coulomb interactions that cause the opening of a soft gap in the density of states [17] or charging energy in a granular (quasi-)metallic system [18,19].

From the few papers addressing the charge transport in PEDOT:PSS systems no consistent picture emerges. For instance, some authors [20,21,22] have interpreted the temperature dependence of the conductivities of pristine PEDOT:PSS thin films in terms of a 1D-VRH model with $\alpha = 1/2$. On the other hand, Aleshin *et al.* [3] interpreted $\alpha = 1/2$ on free-standing pristine PEDOT:PSS thick films in terms of a charging energy model [18,19] proposed by Zuppiroli *et al.* [23]. In this model, conduction is supposed to result from tunneling between small conducting grains separated by an insulating barrier. Such model seems reasonable to explain electronic conduction in PEDOT:PSS thin films since their morphology is supposed to be a phase segregated material consisting of conductive PEDOT-rich grains surrounded by a shell formed by excess PSS [24], which is only weakly (ionically) conducting and acts as an insulating barrier. However, in this model a particular relation between shell thickness and core diameter of the particles is required, for which, in the case of PEDOT:PSS, no experimental indications are found [12].

Recently, more detailed insights in the morphology of PEDOT:PSS have been obtained. Conductive AFM experiments on μm -thick drop cast PEDOT:PSS films have suggested that the morphological model for PEDOT:PSS thin films is actually a lamellar structure of PEDOT and PSS [10]. In the previous Chapter [12], the lamellar structure was confirmed and resolved in more detail for spin coated thin films by phase-sensitive AFM on cryogenically cleaved PEDOT:PSS samples, which revealed a cross-sectional view of the morphology. From that, it was found that the PEDOT-rich oblate spheroid- or pancake-shaped particles, 20-30 nm in diameter (d_{\parallel}), 4-6 nm in height (d_{\perp}), are actually organized in layers that are separated by quasi-continuous nm-thick PSS lamellas, see Figure 4.1 for a schematic representation. The morphology qualitatively explained the observed differences in magnitude and temperature dependence of the conductivity in the normal (\perp) and parallel (\parallel) current directions. Particularly, it was shown that the conductivities of spin coated PEDOT:PSS thin films, measured in lateral and vertical directions with respect to the sample surface, are highly anisotropic in the temperature range of 77 K – 300 K and are well described by Eq. 4.1 [12]. In the normal direction, the horizontal PSS lamellas were assumed to impose nearest-neighbor [16,17] hopping (nn-H) between the quasi-metallic PEDOT particles, leading to a strongly reduced conductivity and a temperature exponent

$\alpha = 1$. The exponent $\alpha = 1/4$ that is observed for lateral transport was tentatively attributed to variable-range hopping (VRH) [16,17] between the PEDOT-rich particles that laterally are separated by much thinner barriers, leading to an enhanced conductivity in this direction.

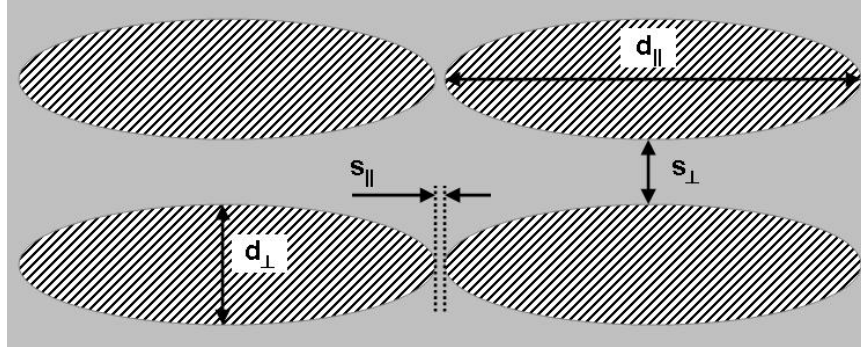


Figure 4.1: Schematic representation of the morphological model for PEDOT:PSS, side view. Quasi-metallic PEDOT-rich clusters (hatched regions) are separated by lamellas of insulating PSS (gray background).

The present investigation is motivated by the need to quantify this model. In particular, the question is raised what is the nature of the states between which the hopping takes place. Are these individual (sub)nm-sized molecular sites formed by e.g. single ionized PEDOT segments, or are these PEDOT-rich particles that contain many, strongly coupled ionized PEDOT segments? We will show results of the electric field dependence measurements (non-ohmic hopping conduction) where the characteristic hopping lengths for vertical (L_{\perp}) and lateral (L_{\parallel}) transport are extracted and found to agree very well with the expectations for VRH and nn-H transport. Based on the L_{\parallel} values, it will be demonstrated that the hopping process takes place between PEDOT-rich islands and not between single PEDOT segments or dopants. The constant L_{\perp} values indicate hopping within and through the insulator PSS barrier. In the end, these results are combined in a morphological model that is fully consistent with earlier findings of Chapter 3 and accounts quantitatively for all parameters involved in the charge transport.

4.2 Experimental

The commercially available aqueous dispersion of PEDOT:PSS (Baytron P VP Al 4083 from H. C. Starck) has been used. Sample preparation and electrical measurements in both lateral (\parallel) and vertical (\perp) directions followed the same procedures described in Chapter 3, section 3.2 on page 41.

4.3 Results

4.3.1 Temperature dependence

The temperature dependencies of the conductivity $\sigma(T)$ in the Ohmic or low electric field regime for the spin coated PEDOT:PSS thin films measured in lateral and vertical directions are shown in Figure 4.2(a) and (b) [25].

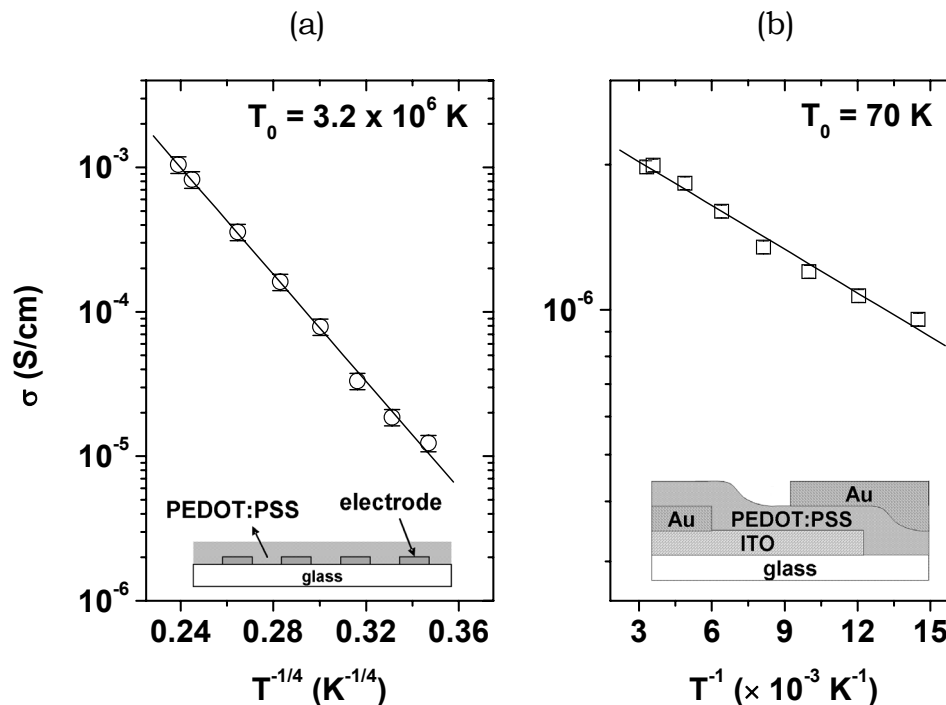


Figure 4.2: Symbols represent conductivity vs (a) $T^{-1/4}$, and (b) T^{-1} for PEDOT:PSS samples measured in lateral (\parallel) and vertical directions (\perp), respectively. Straight lines are fits to Eq 4.1. The insets show the used devices. The bottom gold layer in the vertical device shunts the ITO underneath, which has a much higher resistivity. Electrical contacts are made to both gold pads, which have a lateral separation of less than 1 mm.

Two remarkable features are observed in Figure 4.2. First, the large difference in magnitude of σ . Second, the different temperature dependence of σ , as observed by the different values of α for \parallel and \perp directions. Since α is the main parameter to give information about the conduction mechanism, and the measured temperature-dependent data of any material may exhibit, within experimental error, visually good and indistinguishable linearity on $\log \sigma(T)$ vs. $T^{-\alpha}$ plots for “any” α value between 0.1 and 1 over the entire temperature range, its precise value is of major importance. In Figure 4.3, the correlation coefficient of the fit of Eq. 4.1 to the measured conductivity is plotted against α . The maxima are $\alpha_{\parallel} = 0.25 \pm 0.01$ ($R = 0.99999$) and $\alpha_{\perp} = 0.81 \pm 0.25$ ($R = 0.99621$), close to the theoretical values $1/4$ for 3D-VRH and 1 for nn-H. Using a equal to $1/4$ we find the fitting parameters of Eq 4.1 for the \parallel direction as the slope $T_{0,\parallel} = (3.2 \pm 0.1) \times 10^6$ K and $\sigma_0 = (24.6 \pm 1.3)$ S/cm. In this case, $T_{0,\parallel} = \beta/N(E_F) \xi_{\parallel}'^3 k_B$, where β (~ 21.2) [17] is a numerical factor, k_B the Boltzmann constant and ξ_{\parallel}' is the effective localization length [26].

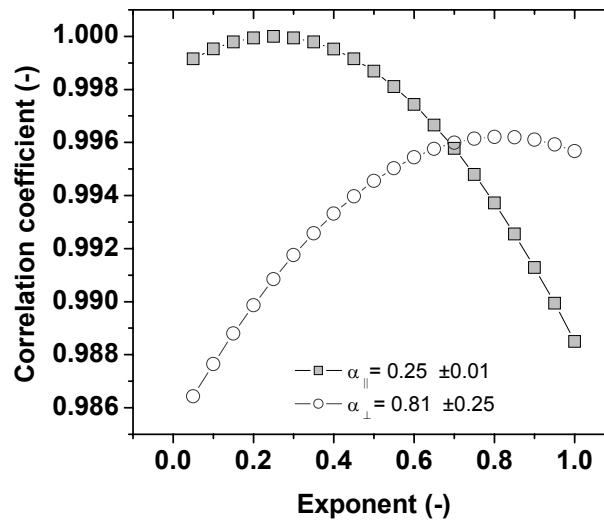


Figure 4.3: Correlation coefficients of the measured and fitted (using eq. 4.1) conductivity versus exponent α for PEDOT:PSS samples measured in lateral (\parallel) and vertical directions (\perp) over 77 K – 300 K.

In the \perp direction, the activation energy is the slope $E_3 = k_B T_{0,\perp} \sim 1/N(E_F) a^3$, with a the average inter-site distance (roughly equal to the cube root of the site density), giving $\sigma_0 = (2.6 \pm 1.1) \times 10^{-6}$ S/cm and $E_3 = (6.0 \pm 0.5) \times 10^{-3}$ eV which

corresponds to $T_{0,\perp} = 70$ K. In this case, the parameter E_3 represents the typical inter-site energy difference.

4.3.2 Electric field dependence

We turn our attention now to the electric field dependence measurements, which enable one to extract the length scales of the predominant transport process [27,28]. As the applied electric field approaches zero, σ approaches a constant value which depends on the temperature, i.e. the Ohmic regime is entered. In the opposite case, as the electric field is increased, deviations from Ohmic behavior become apparent and one expects an increase in σ when the energy associated with the electric field times a typical hopping distance becomes of the same order as the typical inter site energy difference.

4.3.2.1 Normal direction

For nn-H in a disordered material, as observed here in the \perp direction, we first derive an expression to quantify the non-ohmic conductivity. We require that the current be symmetrically modified by forward and reverse fields, i.e. the electric field modifies the forward and reverse hopping probabilities by equally lowering and raising the energy required for typical forward and reverse hops. This directly leads to the following equation for the vertical current density J_{\perp} :

$$J_{\perp}(F,T) \propto \exp\left[-\frac{E_3}{k_B T}\right] \left\{ \exp\left(\frac{eF_{\perp}L_{\perp}}{k_B T}\right) - \exp\left(-\frac{eF_{\perp}L_{\perp}}{k_B T}\right) \right\} \propto \left\{ 2 \sinh\left(\frac{eF_{\perp}L_{\perp}}{k_B T}\right) \right\} \quad \text{Eq 4.2}$$

where E_3 is the activation energy, $\frac{eF_{\perp}L_{\perp}}{k_B T}$ is the amount by which forward and reverse energies are lowered and raised and e is the electron charge. F_{\perp} and L_{\perp} are the applied electric field and the characteristic nearest-neighbor hopping length in the \perp direction, respectively.

In Eq 4.2, by expanding the \sinh function as $x + \frac{x^3}{3!} + \dots + \frac{x^{2n+1}}{(2n+1)!}$ and combining with $\sigma = J/F$, we find for the electric field dependence of conductivity at modest fields, i.e. $(eF_{\perp}L_{\perp}/k_{\text{B}}T) < 1$:

$$\sigma_{\perp}(F, T) \propto \sigma_{0,\perp}(0, T) \left[1 + \frac{1}{6} \left(\frac{eF_{\perp}L_{\perp}}{k_{\text{B}}T} \right)^2 \right] \quad \text{Eq 4.3}$$

The experimental dependence of the conductivity on field strength is shown in Figure 4.4(a) for the \perp direction. The conductivity increases with the applied electric field F , especially at lower temperatures.

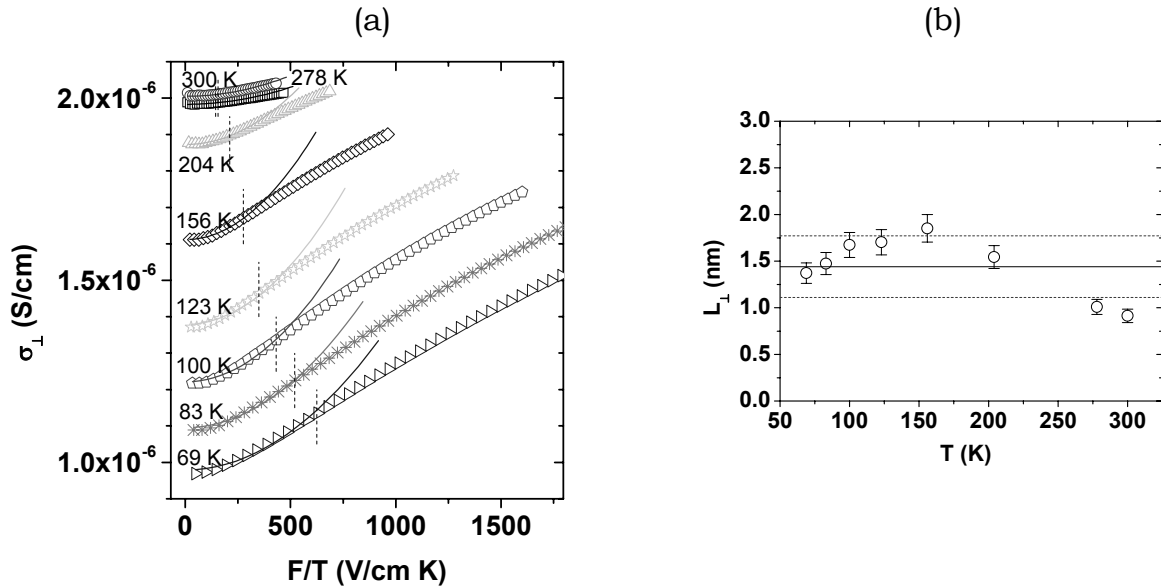


Figure 4.4: (a) Conductivity vs. F/T for PEDOT:PSS thin film measured in vertical (\perp) direction with respect to the film plane at different temperatures. Solid lines are fits to Eq 4.3; (b) Temperature dependence of the characteristic hopping length L_{\perp} for the same sample. $L_{\perp} = (1.4 \pm 0.4)$ nm.

In Figure 4.4(a), the solid lines are fits to Eq. 4.3 and the slopes of σ vs. F/T curves for $F \rightarrow 0$, which give L_{\perp} , were extracted and plotted in Figure 4.4(b). Despite the relatively large scatter and the magnitude of the error bars, Figure 4.4(b) shows the absence of a clear trend in $L_{\perp}(T)$, in agreement with nn -H theory [16,17]. Taking a equal to $L_{\perp} = 1.4$ nm and $T_0 = 70$ K we find $N(E_{\text{F}})_{\perp} = 6.0 \times 10^{22}$ $\text{eV}^{-1}\text{cm}^{-3}$.

4.3.2.2 Lateral direction

Several authors derived expressions for the electric field dependence of the current in 3D-VRH at modest fields, i.e. when $(eF_{\parallel}L_{\parallel}/k_{\text{B}}T) < 1$. Ladiou *et al.* [29] have summarized the 3D-VRH current equation for modest electric fields as follows:

$$I_{\parallel}(F, T) = I_{o,\parallel} \exp \left\{ - \left(\frac{T_0}{T} \right)^{\alpha} \left[1 - A \frac{(eF_{\parallel}\xi'_{\parallel})^x}{(k_{\text{B}}T)^{x'}} + B \left(\frac{eF_{\parallel}\xi'_{\parallel}}{k_{\text{B}}T} \right)^{\beta} \right] \right\} \quad \text{Eq 4.4}$$

where A , B , x , x' and β are parameters, A and B being positive. The first term $A(eF_{\parallel}\xi'_{\parallel})^x/(k_{\text{B}}T)^{x'}$ represents the enhancement of the hopping probability when F grows. The second term $B(eF_{\parallel}\xi'_{\parallel}/k_{\text{B}}T)^{\beta}$ was only addressed by Böttger *et al.* [30] and arises when the presence of reverse hops, or ‘returns’ in the optimal percolation pathway is taken into account [30]. When the field increases, these trajectories rapidly loose probability, which prevents the current from increasing too quickly, and may actually lead to a negative differential conductivity. At somewhat higher fields, this term becomes irrelevant, and under typical experimental conditions Eq. 4.4 converges to [28,29,30,31]

$$\sigma_{\parallel}(F, T) = \sigma_{o,\parallel}(0, T) \exp \left(0.17 \frac{eF_{\parallel}L_{\parallel}}{k_{\text{B}}T} \right) \quad \text{Eq 4.5}$$

where F_{\parallel} is the applied electric field and L_{\parallel} the characteristic hopping length. Note that Eq. 4.5 results from Eq. 4.4 by neglecting the returns ($B = 0$) and by assuming that the F_{\parallel} and T dependencies of σ_{\parallel} and I_{\parallel} are close to each other. An expression similar to Eq. 4.5 was derived by Shklovskii *et al.* who ignored correlations between site energies [28] but took field-induced changes in the local chemical potential into account [32], giving $A \approx 1$, $x = x' = 0.53$ and $B = 0$ in Eq. 4.4. In order to limit the number of free parameters, we shall first use Eq. 4.5 to describe the ‘high’ electric field data and subsequently use these parameters as input in Eq. 4.4 to interpret our full results.

At each temperature in Figure 4.5(a), the data are fitted quite well by straight lines, using Eq. 4.5. Indeed, the nonzero slope of σ_{\parallel} vs. F/T in the entire field range shown indicates that there is an electric-field-induced nonlinearity in σ_{\parallel} and this behavior, as for the \perp direction, is more pronounced at low temperatures.

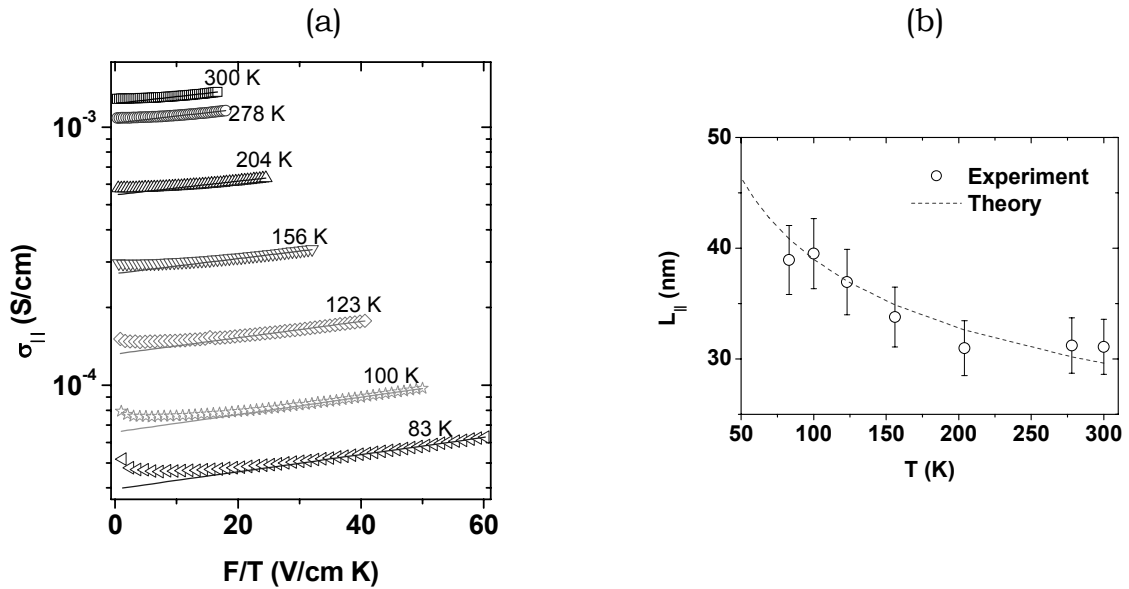


Figure 4.5: (a) Conductivity vs. F/T for PEDOT:PSS thin film measured in lateral (\parallel) direction with respect to the film plane at different temperatures. Solid lines are fits to Eq. 4.5. (b) Temperature dependence of the characteristic hopping length L_{\parallel} for the same sample.

As the temperature is changed, the slope of the lines through the data in Figure 4.5(a) also changes, implying that the characteristic hopping length L_{\parallel} , in contrast to L_{\perp} , is temperature dependent, in agreement with VRH theory. Figure 4.5(b) shows a plot of the temperature dependence of L_{\parallel} . The characteristic hopping length in 3D VRH is expected to vary as $T^{-1/4}$ at low temperatures. By combining the expression for the slope $T_0 = \beta/N(E_F) \xi_{\parallel}^3 k_B$ and the Mott expression for $L_{\parallel} = [(8\pi/9)k_B T N(E_F) / \xi_{\parallel}']^{-1/4}$ [33] we arrive at

$$\frac{L_{\parallel}}{\xi_{\parallel}'} = \left[\frac{9}{8\pi\beta} \right]^{1/4} \left[\frac{T_0}{T} \right]^{1/4} \quad \text{Eq 4.6}$$

which is used to fit the experimental data of $L_{||}$ by adjusting the term $\xi'_{||}$ (dashed line in Figure 4.5(b)). Clearly, the experiment is well described by the theoretical prediction and $\xi'_{||}$ was found to be (8.2 ± 0.5) nm. Using this result and the expression for $T_{0,||}$, $N(E_F)_{||}$ is found to be 1.4×10^{17} eV⁻¹cm⁻³. Most importantly, the magnitude of the characteristic hopping length in the lateral direction is fully consistent with hopping transport between ~ 25 nm sized particles, rather than with hopping between individual molecular sites.

4.4 Discussion

Table 4.I: Parameters describing the electrical conduction in Baytron P PEDOT:PSS thin films. See text for further discussion.

	Lateral ()	Vertical (⊥)
conduction mechanism	3D-VRH	nn-H
σ at 300 K (S/cm)	$(1.1 \pm 0.1) \times 10^{-3}$	$(2.0 \pm 0.1) \times 10^{-6}$
T_0 (K)	$(3.2 \pm 0.1) \times 10^6$	70 ± 6
σ_0 (S/cm)	24.7 ± 1.3	$(2.6 \pm 1.1) \times 10^{-6}$
$N(E_F)$ (eV.cm³)⁻¹	$(1.4 \pm 0.2) \times 10^{17}$	$(6.0 \pm 1.7) \times 10^{22}$
ξ' (nm)	8.2 ± 0.5	---
L (nm)	30 - 40	1.4 ± 0.4

In this section, the length scales and density of states that were extracted in the preceding section will be evaluated and, where possible, related to the morphological model outlined in the Introduction. Secondly, the discrepancies between the experimental and fitted conductivities in Figure 4.4(a) and Figure 4.5(a) will be discussed.

The use of an effective localization length $\xi'_{||}$, instead of the normal one which appears in conventional Mott theory, is common practice in granular systems [26]. The underlying argument is that the only *significant* decay of the wave function occurs in the separating barriers, i.e. in the quasi-insulating PSS, and not in the quasi-metallic PEDOT-rich particles. This implicitly requires a strong coupling between the wave functions of the individual PEDOT sites. Given the high degree of doping -about 1 in 3 PEDOT monomers is ionized [34]- and the

high PEDOT density in the cores, -the cores take up less than half the film volume [12]- the fulfillment of this requirement is not at all unlikely [23]. Under this condition, the relation between the effective localization length and the decay length in the barrier ξ can be approximated by $\xi_{\parallel}' = \xi(d_{\parallel} + s_{\parallel})/s_{\parallel}$ with d_{\parallel} and s_{\parallel} the particle diameter and spacing, as defined in Figure 4.1. The absence of an accurate measure of s_{\parallel} prevents a precise calculation of ξ , but taking s_{\parallel} between 0.5 and 1 nm and $d_{\parallel} = 25$ nm, a value of ξ in the range 0.15 - 0.3 nm is found, which again seems reasonable [23].

Turning now to the density of states, we observe that the experimentally extracted value in Table I, $N_{\parallel}(E_F) = 1.4 \times 10^{17} \text{ eV}^{-1}\text{cm}^{-3}$, corroborates the physical picture sketched in the preceding paragraph. Assuming a rectangular density of states with a typical width of 0.5 eV, and a volume per site of $25 \times 25 \times 6 \text{ nm}^3$, the morphological model leads to a density of states of roughly $1.3 \times 10^{17} \text{ eV}^{-1}\text{cm}^{-3}$, in excellent agreement with the value derived from transport measurements.

The large and unexpected difference between $N_{\parallel}(E_F)$ and $N_{\perp}(E_F)$ of ~ 5 orders of magnitude indicates that the sites that dominate the transport are not the same for both directions. In addition, the value of 1.4 nm found for a is in contradiction with nearest-neighbor hopping (nn-H) between PEDOT-rich particles. In the latter case, a value of 5-6 nm should be observed. Therefore it is concluded that the dominating nn-H process is, in fact, taking place between dilute states inside the insulating PSS lamellas.

These results are fully consistent with previous, qualitative analysis in Chapter 3, on similar samples [12] and we conclude that the temperature and field dependencies of the anisotropic conductivity in spin-coated PEDOT:PSS thin films are in full quantitative agreement with the morphological model proposed in Chapter 3.

Let us now come back to the deviations from the theoretically predicted field dependence in Figure 4.4(a) and Figure 4.5(a). In the vertical direction (Figure 4.4(a)), the conductivity is found to increase slower than quadratically beyond certain field strength. The critical field F_c at which this sets in is given by the ratio of the energy difference E_3 and tunneling distance a associated with a typical hop, i.e. $E_3 = k_B T_0 \approx eaF_c$. The vertical lines in Figure 4.4(a) indicate the

position of F_c for the various curves. As expected, once the critical field is reached, the differential conductivity decreases.

Finally, we return to the problem of the *returns* in the lateral conductivity. The problem is extremely complex and the precise values of the parameters in Eq. 4.4 were found to depend on the assumptions made. For example, Shklovskii [32] takes into account changes in the chemical potential by the field, giving $A \sim 1$, $x = x' \sim 0.53$ in Eq. 4.4, whereas Pollak *et al.* [28] take into account the correlations between nearest-neighbor sites, giving $x = x' = 1$ and $A = 0.085$ in Eq. 4.4. For both models, however, the *returns*, i.e. the second term in Eq. 4.4, are neglected. In the few theoretical works dealing with this problem Böttger *et al.* have found by numerical calculation [30] $x = x' = 1$, $A = 1/6$, $B \sim 0.02$ and $\beta \sim 0.9$, with β a parameter related to the return length, with 50 % of error due to numerical uncertainties. In order to assess this behavior in our samples we therefore re-plot Figure 4.5(a) into Figure 4.6 and for each temperature a fit to Eq. 4.4 has been performed using as fixed parameters those ones previously obtained, i.e. T_0 , α , $\xi_{||}'$ and $x = x' = 1$.

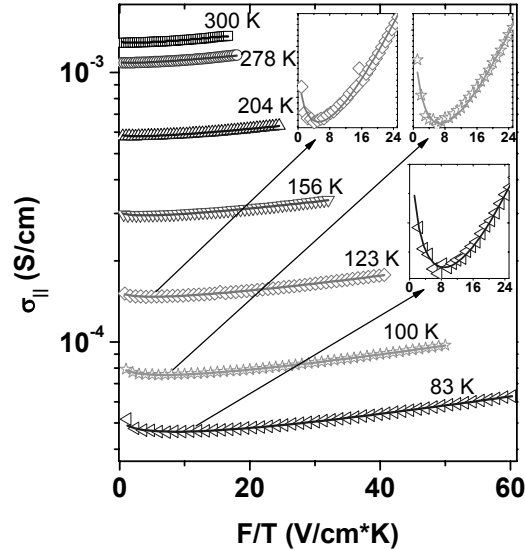


Figure 4.6: Conductivity vs. F/T for a PEDOT:PSS film measured in lateral (\parallel) direction with respect to the film plane at different temperatures. Solid lines are fits to Eq. 4.4, considering the presence of reverse hops, or *returns* in the optimal percolation pathway. The insets show the same conductivity vs. F/T plots for sample at 83 K, 100 K, and 123 K restricted to low electric fields.

In the investigated temperature range, we found that the Pollak model best describes our data, yielding in the second term of Eq. 4.4 $B = 0.02 - 0.05$ and $\beta =$

0.36 – 0.60, not so far from the values found by Böttger [30]. Due to the various uncertain numerical factors involved in the theoretical works, we refrain from making an estimation of the actual length of the returns. However, taking into account the second term of Eq. 4.4, a distinctly better description of the data is obtained, especially at low electric field and temperature, see insets of Figure 4.6 for 83 K, 100 K, and 123 K, where this behavior is more pronounced. Qualitatively, these results show that a considerable rearrangement of the percolation pathways occurs in these samples at relatively low field strengths. The convergence of the data to the description by Pollak *et al.* [28] (Eq. 4.4) indicates that at intermediate fields the percolation pathways are more or less fixed in space.

4.5 Conclusions

The presented results allow us to set a quantitative morphological model for PEDOT:PSS thin films that, on the one hand, incorporates all length scales that are found in the field dependent measurements and, on the other hand, is fully consistent with previously reported scanning probe data [12] in Chapter 3, see Figure 4.1. In the \perp direction, the separating PSS barriers are (quasi) continuous and 1-2 nm thick, whereas the separations in the \parallel direction are on average much thinner, i.e. $s_{\perp} \gg s_{\parallel}$. Due to this particular morphology, spin cast films of PEDOT:PSS have a relatively high in-plane conductivity, which is well described by 3D variable range hopping. In the out-of-plane direction, the low site density in the PSS enforces nearest neighbor hopping and an up to three orders of magnitude lower conductivity.

4.6 References and notes

- [1] *Handbook of Conducting Polymers*, 3rd Ed. T. A. Skotheim, J. Reynolds (Eds.), CRC Press, **2007**.
- [2] a) L. B. Groenendaal, F. Jonas, D. Freitag, H. Pielartzik, J. R. Reynolds, *Adv. Mater.* **2000**, *12*, 481. b) S. Kirchmeyer, K. Reuter, *J. Mater. Chem.* **2005**, *15*, 2077.
- [3] A. N. Aleshin, S. R. Williams, A. J. Heeger, *Synth. Met.* **1998**, *94*, 173.
- [4] F. Jonas, W. Krafft, B. Muys, *Macromol. Symp.* **1995**, *100*, 169.
- [5] M. M. de Kok, M. Buechel, S. I. E. Vulto, P. van de Weijer, E. A. Meulenkaamp, S. H. P. M. de Winter, A. J. G. Mank, H. J. M. Vorstenbosch, C. H. L. Weijtens, V. van Elsbergen, *Phys. Stat. Sol. A* **2004**, *201*, 1342.
- [6] C. J. Ko, Y. K. Lin, F. C. Chen, C. W. Chu, *Appl. Phys. Lett.* **2007**, *90*, 063509.
- [7] F. Verbakel, S. C. J. Meskers, R. A. J. Janssen, *Chem. Mater.* **2006**, *18*, 2707.
- [8] S. C. J. Meskers, J. K. J. van Duren, R. A. J. Janssen, F. Louwet, L. Groenendaal, *Adv. Mater.* **2003**, *15*, 613.
- [9] A. Kumar, D. M. Welsh, M. C. Morvant, F. Piroux, K. A. Abboud, J. R. Reynolds, *Chem. Mater.* **1998**, *10*, 896.
- [10] C. Ionescu-Zanetti, A. Mechler, S. A. Carter, R. Lal, *Adv. Mater.* **2004**, *16*, 385.
- [11] S. Timpanaro, M. Kemerink, F. J. Touwslager, M. de Kok, S. Schrader, *Chem. Phys. Lett.* **2004**, *394*, 339.
- [12] A. M. Nardes, M. Kemerink, R. A. J. Janssen, J. A. M. Bastiaansen, N. M. M. Kiggen, B. M. W. Langeveld, A. J. J. M. van Breemen, M. M. de Kok, *Adv. Mater.* **2007** *19*, 1196.
- [13] X. Crispin, F. L. E. Jakobsson, A. Crispin, P. C. M. Grim, P. Anderson, A. Volodin, C. van Haesendonck, M. Van der Auweraer, W. R. Salaneck, M. Berggren, *Chem. Mater.* **2006**, *18*, 4354.
- [14] J. Huang, P. F. Miller, J. S. Wilson, A. J. de Mello, J. C. de Mello, D. D. C. Bradley, *Adv. Funct. Mater.* **2005**, *14*, 562.
- [15] T. Y. Kim, J. E. Kim, K. S. Suh, *Polym. Int.* **2006**, *55*, 80.
- [16] N. Mott, E. A. Davis, *Electronic Processes in Non-Crystalline Materials*, Clarendon Press, Oxford, **1979**.
- [17] B. I. Shklovskii, A. L. Efros, *Electronic Properties of Disordered Semiconductors*, Springer, Berlin, **1984**.
- [18] P. Sheng, B. Abeles, Y. Arie, *Phys. Rev. Lett.* **1973**, *3*, 44.
- [19] P. Sheng, *Phys. Rev. B* **1980**, *21*, 2180.
- [20] J. Y. Kim, J. H. Jung, D. E. Lee, J. Joo, *Synth. Met.* **2002**, *126*, 311.
- [21] J. Ouyang, Q. Xu, C. W. Chu, Y. Yang, G. Li, J. Shinar, *Polymer* **2004**, *45*, 8443.
- [22] S. Ashizawa, R. Horikawa, H. Okuzaki, *Synth. Met.* **2005**, *153*, 5.
- [23] L. Zuppiroli, M. N. Bussac, S. Paschen, O. Chauvet, L. Forro, *Phys. Rev. B* **1994**, *50*, 5196.

- [24] X. Crispin, S. Marciniak, W. Osikowicz, G. Zotti, A. W. Denier van der Gon, F. Louwet, M. Fahlman, L. Groenendaal, F. de Schryver, W. R. Salaneck, *J. Polym. Sci Part B: Polym. Phys.* **2003**, *41*, 2561.
- [25] The values of the parameters T_0 and σ_0 are found to depend on the batch of material used, and on the age of the batch. These variations in T_0 and σ_0 are typically less than a factor ~ 2 and ~ 10 , respectively. Variations between samples prepared on one day are typically below 10% for both parameters. The values of α do not vary with batch or sample.
- [26] J. Zhang, B. I. Shklovskii, *Phys. Rev. B* **2004**, *70*, 115317.
- [27] R. M. Hill, *Philos. Mag.* **1971**, *24*, 1307.
- [28] M. Pollak, I. Riess, *J. Phys. C* **1976**, *9*, 2339.
- [29] F. Ladieu, D. L'Hôte, R. Tourbot, *Phys. Rev. B* **2000**, *61*, 8108.
- [30] a) H. Böttger, D. Wegener, *Phys. Status Solidi B* **1984**, *121*, 413. b) H. Böttger, V. V. Bryksin, *Hopping Conduction in Solids* (VCH, Deerfield Beach, FL, **1985**), pp. 236-259. c) Böttger, D. Wegener, in *Hopping and Related Phenomena*, edited by H. Fritzche and M. Pollak (World Scientific, Singapore, **1990**). d) H. Böttger, P. Szyler, D. Wegener, *Phys. Status Solidi B* **1985**, *128*, K179. e) H. Böttger, P. Szyler, D. Wegener, *Phys. Status Solidi B* **1986**, *133*, K143.
- [31] E. I. Levin, B. I. Shklovskii, *Sov. Phys. Semicond.* **1984**, *18*, 534.
- [32] B. I. Shklovskii, *Sov. Phys. Semicond.* **1976**, *10*, 855.
- [33] N. F. Mott, *Metal-Insulator Transitions*, Taylor and Francis, London, **1974**.
- [34] F. Zhang, A. Petr, H. Peisert, M. Knupfer, L. Dunsch, *J. Phys. Chem. B* **2004**, *108*, 17301.

Conductivity and environmental stability of PEDOT:PSS thin films treated with sorbitol

The electrical properties of poly(3,4-ethylenedioxythiophene):poly(4-styrenesulfonate) (PEDOT:PSS) thin films deposited from aqueous dispersion using different concentrations of sorbitol as a processing additive were monitored in time during changes in temperature and relative humidity (RH). The results are compared to pristine thin films, processed without adding sorbitol. With increasing RH, the conductivity of the pristine PEDOT:PSS initially degrades, until it increases by more than one order of magnitude above ~ 30-35 % RH. This increase is attributed to an ionic contribution to the overall conductivity. In contrast, it is found that the well-known conductivity enhancement of PEDOT:PSS films prepared using sorbitol as a processing additive, is accompanied by an increased environmental stability. The higher stability results from a reduced tendency to take up water from the air, which is attributed to a denser packing of the PEDOT:PSS after sorbitol treatment.

5.1 Introduction

The electronic properties of conducting polymers are of interest for physical concepts and technological applications. Accordingly, the development of highly conducting polymers with a good stability and an acceptable processability has been the focus of many recent studies [1]. Currently, a variety of conducting polymers is available for various applications, such as polyaniline, polypyrrole, and polythiophenes [2]. In this respect, poly(3,4-ethylenedioxythiophene) (PEDOT) has been found to exhibit a relatively high conductivity and appears to be the most stable conducting polymer currently available [3,4]. PEDOT itself is an insoluble material but when it is synthesized in the presence of poly(4-styrenesulfonate) (PSS) an aqueous dispersion can be obtained that can be cast into thin films. In the films positively charged PEDOT chains are incorporated into a negatively charged PSS matrix that acts to compensate the charges (Figure 5.1). The aqueous PEDOT:PSS dispersions have found a wide range of application in antistatic coatings [5], as electrode in light-emitting diodes [6], photovoltaics [7], memories [8], sensors [9], and as active material for electrochromic devices [10], field-effect transistors [11] and circuits in general [12].

Thin films of PEDOT:PSS blends [3,4,13] are extremely hygroscopic [14] and post-deposition treatments in air by thermal annealing are generally unstable due to the fast water uptake. For example, reported conductivities measured in air are roughly one order of magnitude lower compared to those measured under an inert environment [14,15].

Addition of sorbitol, a polyhydroxy alcohol, to the aqueous PEDOT:PSS dispersion is known to enhance the conductivity of the thin films by several orders of magnitude, depending on its concentration [14]. The dramatic effect of sorbitol as processing additive arises from a further reorganization and stabilization of the PEDOT and PSS chains during subsequent thermal annealing of the films by a plasticizing effect [16]. While this method to enhance the conductivity has been previously studied, the reasons for the remarkable behavior are still under debate [16,17,18,19,20,21,22].

In this Chapter, the conductivity and environmental stability of poly(3,4-ethylenedioxythiophene):poly(4-styrenesulfonate) (PEDOT:PSS) with different sorbitol concentrations is investigated. In-situ conductivity and water-uptake

measurements during thermal treatment and exposure to humidity are combined to further investigate the various properties of pristine and sorbitol-treated PEDOT:PSS thin films [14,23]. It is found that the conductivity enhancement upon addition of sorbitol is accompanied by an enhanced environmental stability towards uptake from water. This effect is attributed to a denser packing of the sorbitol-treated films, reducing the water uptake, in combination with a morphology that is less susceptible to swelling. The results presented here have immediate implications for device making.

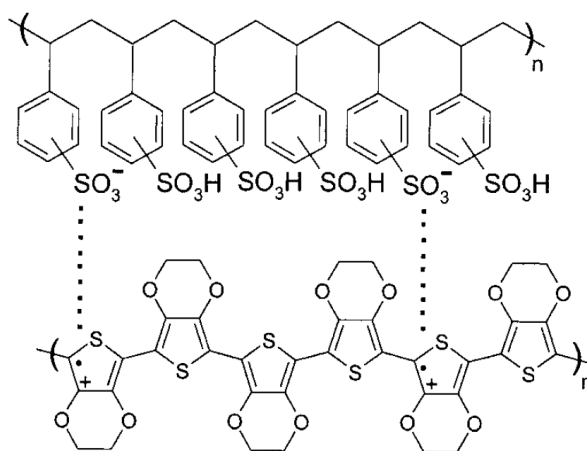


Figure 5.1: Chemical structure of PEDOT (bottom) and PSS (top).

5.2 Experimental

Sample preparation for the 4-point-probe electrical measurements (lateral direction, ||) followed the same procedure described in Chapter 3, section 3.2 on page 41.

The commercially available aqueous dispersion of PEDOT:PSS (Baytron P VP Al 4083 from H. C. Starck) has been used. Different amounts of sorbitol were added to the aqueous dispersion, 2.5 wt-% (of the total solution), 5.0 wt-% and 10 wt-% of D-sorbitol 97% (Sigma-Aldrich). The solutions were stirred for at least 24 h at room temperature and filtered using a 5 μ m filter and deposited in air by spin coating, which resulted in 90-100 nm thick films as measured by a profilometer (Alpha-step 200, Tencor Instruments). As a comparison, PEDOT:PSS

without sorbitol was used, referred to as 'pristine', and in this case the film thickness was about 60 nm.

For both the humidity and annealing experiments, the conductivity has been measured as a function of time during the variation of moisture levels and temperature. The humidity experiments were carried out in an in-house made glove box capable of varying and controlling the relative humidity up to 50 % by fluxing N₂ bubbled through demineralized water (degassed with He) into the box. The samples were first annealed at 200 °C for 2 min and then placed on a block of stainless steel to rapidly cool down. Electrical measurements were performed by an Agilent semiconductor analyzer, model 4156C, under constant applied bias, and acquired every 10 sec. Only after 1 to 2 hours when the conductivity had stabilized, the humidity levels have been increased, first up to 30 % for each sample (0, 2.5, 5 and 10 wt-%) and then repeated again to up to 50 % of relative humidity, always using fresh samples.

For the annealing experiments, samples were transferred to a commercial Mbraun glove box (O₂ and H₂O < 1 ppm) and placed on a hot plate. Electrical measurements have also been performed by the semiconductor analyzer, under constant bias and at every 10 sec during the entire annealing process, i.e. heating up to 200 °C, constant at 200 °C for 2 min, and cooling down. Temperature-dependent (77-300 K) conductivity measurements have been performed only for the pristine sample in the situations of (i) not annealed, (ii) annealed, and (iii) after the exposure to moisturized environment for the same device. In this case, the sample was also transferred into a glove box (O₂ and H₂O < 1 ppm). After cutting the desired sample from the substrate, it was placed inside a cryostat (Oxford Instruments), evacuated to 10⁻⁵ mbar and brought to the desired temperature in the 77-300 K range. Temperature control was provided by an Oxford ITC 601 Temperature Controller that maintained temperature stability within ± 0.1 K. Electrical measurements were performed with a Keithley 2410 source meter connected to a PC. For all temperature-dependent measurements the electrical connections were made inside the glove box, so the sample never experienced contact with air after bake-out. From a comparison of 2- and 4-terminal measurements the contact resistance was found to be negligible for all our samples.

Water uptake was studied by thermal gravimetric analysis (TGA) and quartz crystal microbalance experiments (QMB). TGA was measured with a Q500 Thermogravimetric Analyzer (TA Instruments) at a heating rate of 10 °C/min under a moisturized atmosphere created by fluxing 60 ml/min of N₂ bubbled through deionized water into the oven. For TGA experiments, free-standing thick films of pristine and 10 wt-% of sorbitol-added PEDOT:PSS were prepared by casting the solutions on cleaned glass substrates. Here, the UV-ozone treatment step was left out in order keep the surface as hydrophobic as possible. Both samples were dried in air at 120 °C for about 20 min and 60 min for pristine and 10 wt-%, respectively, until dark blue lustrous films were obtained. By doing so, the removal of the film from the glass substrates was relatively easy. For the QMB, only the pristine sample was measured and it was deposited directly onto the piezoelectrical micro-crystal and subsequently dried. This experiment was conducted in an inert environment and the variation of mass was observed by enhancing the humidity level to 49 % by fluxing N₂ bubbled through DI water.

5.3 Results

5.3.1 Effect of thermal annealing

For thermal annealing two different temperature cycles were chosen. Process 1 involves rapid thermal annealing, i.e. the PEDOT:PSS sample is placed for 2 min on a hot plate at 200 °C and rapidly cooled to room temperature on a block of stainless steel for 5 min. Process 2 is more gradual and entails heating up at ~ 10 °C/min, a constant temperature of 200 °C for 2 min, and subsequent natural cooling to room temperature in about 3 hours. During process 2 we monitored changes in conductivity in real-time (Figure 5.2). The first observation in Figure 5.2 is that for all PEDOT:PSS thin films a positive temperature coefficient of conductivity is found during process 2, for both heating and cooling. Below 120 °C, the conductivity of the pristine film is more sensitive to a rise in temperature than the conductivity of thin films processed from sorbitol/water. In the latter case, temperature causes a strong effect in conductivity only above

120 °C, enhancing its value to saturate around 160 °C. At 200 °C, temperature is kept constant for about 2 min and a slight decrease in conductivity is observed for sorbitol-added samples. In contrast, the conductivity increases monotonically for pristine PEDOT:PSS, even after the heating up had finished. The thermal cycling is completed with the natural (~ 3 hours) cooling of the samples to room temperature and constant conductivity (insets in Figure 5.2). The rapid thermal annealing (process 1) affords virtually the same conductivity at the end. Thus, the annealing speed has no significant influence on the final conductivity.

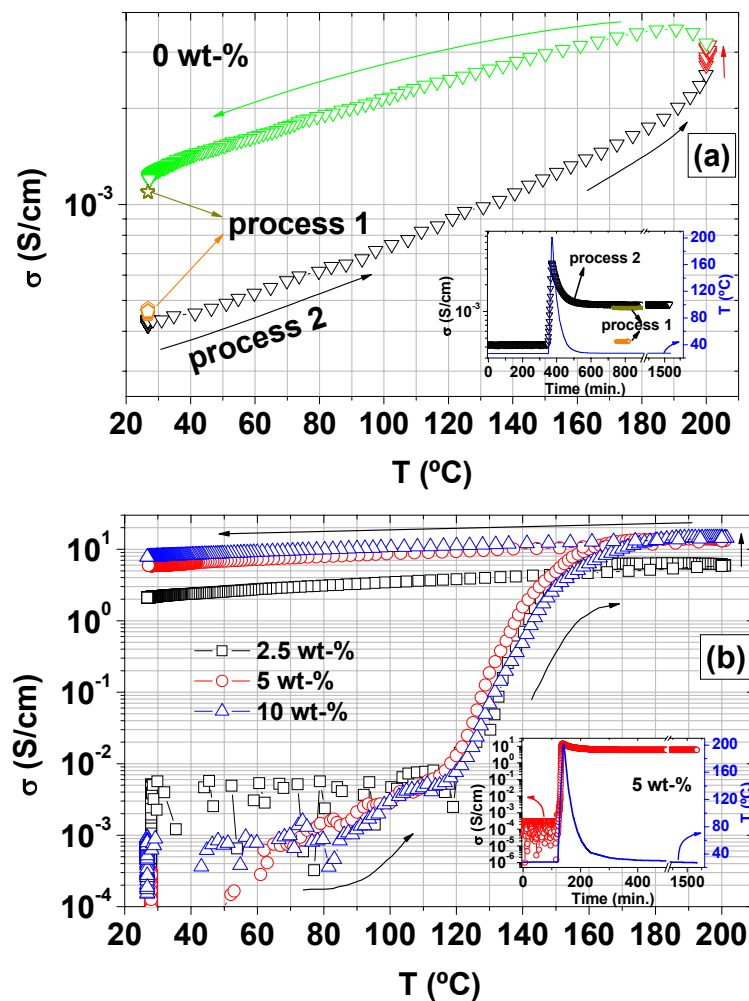


Figure 5.2: Variation of the conductivity with temperature during process 2, i.e. heating up to 200 °C, constant at 200 °C for 2 min, and subsequent cooling of PEDOT:PSS thin films with (a) 0 wt-% (pristine film) and (b) 2.5 to 10 wt-% of sorbitol concentrations. Measurements were performed under N_2 environment. The insets show the evolution of the conductivity as a function of time during the annealing process. The conductivities of process 1 in (a) were measured for sample right after spin coating, i.e. prior to annealing, (open pentagons) and after quick annealing + forced cooling down (open stars). All the other arrows indicate the thermal cycling direction during process 2.

In process 2 thermal hysteresis is evident in all PEDOT:PSS samples and the final conductivities are always higher than the initial, about a factor three for the pristine sample and remarkably 4-5 orders of magnitude for samples that were processed by adding sorbitol to the solution.

The changes in the conductivity for PEDOT:PSS thin films during the annealing procedure under N_2 environment (Figure 5.2) are related to thermally induced morphological changes in the PEDOT:PSS thin films. The conductivities of all sorbitol-added PEDOT:PSS films (Figure 5.2 (b)) appear to follow the same behavior. Temperatures below 120 °C seem to be too low to significantly induce changes in the conductivities. In fact, the addition of sorbitol induces some instability in the conductivity of these films, as suggested by the inset of Figure 5.2(b). Without any annealing (< 100 min) the conductivities oscillate between $\sim 10^{-4} - 10^{-7}$ S/cm. One can easily rule out the possibility of instrumental noise and this effect is found in the majority of the sorbitol-samples prior to annealing. After the sample has been heated above 120 °C, the changes in the conductivity with time become gradual and oscillations disappear. We therefore attribute these fluctuations below 120 °C to localized spontaneous molecular rearrangements facilitated by the plasticizing effect of sorbitol at room temperature, which may induce changes in the percolation pathways [35]. Beyond 120 °C, conductivity is already smoothed. The fact that the conductivity is negatively affected by mixing PEDOT:PSS and sorbitol contradicts other results, where the simple addition of a mixture of high-boiling solvents[†] had a much bigger effect in the conductivity enhancement than the following annealing step [24]. The conductivity of the pristine not-annealed film measured for about 5 hours has a constant (and average) value of 4×10^{-4} S/cm, see the time-dependent measurement in the inset of Figure 5.2(a).

The annealing behavior described above is likely caused by the presence of sorbitol and remnant water enabling morphological changes in the PEDOT:PSS films. The evaporation of sorbitol (and residual water) sets in around 80 °C and reaches a maximum around 120 °C as evidenced from mass spectrometry experiments that show a strong increase of the $m/z = 103$ peak at 80 °C, characteristic of a sorbitol fragment [25]. Since the loss of sorbitol coincides with

[†] This work adopts the term 'high-boiling solvent', commonly used in literature, to refer to a substance with a *boiling-point temperature* higher than water (100 °C, at a pressure of 1 atm). For instance, the *boiling-point temperature* of sorbitol, used in this work, is ~ 300 °C at 1 atm.

the onset of the conductivity increase, we propose that the increased space in the film due to the removal of sorbitol and water, in combination with the large thermal energy during annealing and the plasticizing action of the remaining solvent mixture, enables the PEDOT and PSS clusters to rearrange towards a more relaxed and compact morphology. The latter is supported by AFM and STM studies on these films, in which the lamellar arrangement of PEDOT and PSS appears to be enhanced by sorbitol treatment [16,26]. At 160 °C sorbitol and water have almost completely evaporated from the film [25], which corroborates the above interpretation of the data in Figure 5.2.

5.3.2 Effect of humidity

The change in physical, optical, and electrical properties of polymers with respect to the change on the relative humidity of the environment has been studied in many different aspects [27,28,29,30]. As the relative humidity of the environment increases, water vapor is absorbed by the polymer. Evidently, if any electrical property of a material responds strongly to environmental changes, the material may be used in sensor application [31]. On the other hand, it has been shown that uptake of water by PEDOT:PSS leads to a degradation of the device performance in solar cells that use PEDOT:PSS as an electrode material [32].

In Figure 5.3, we show the variation of conductivity as a function of the RH for PEDOT:PSS thin films prepared from an aqueous dispersion containing sorbitol in different concentrations. Before starting the RH experiment, all samples were thermally annealed following process 1. Each graph in Figure 5.3 shows two curves, which represent the sweeps from zero to medium (up to 30 %) and high (up to 50 %) levels of RH. Independently of the final RH, all experiments demonstrate that exposure of the samples to humidity induces a reduction in conductivity. The remarkable feature in Figure 5.3 is the comparison of the pristine sample (Figure 5.3(d)) with the three samples processed from sorbitol/water mixtures concentration (Figure 5.3(a)-(c)).

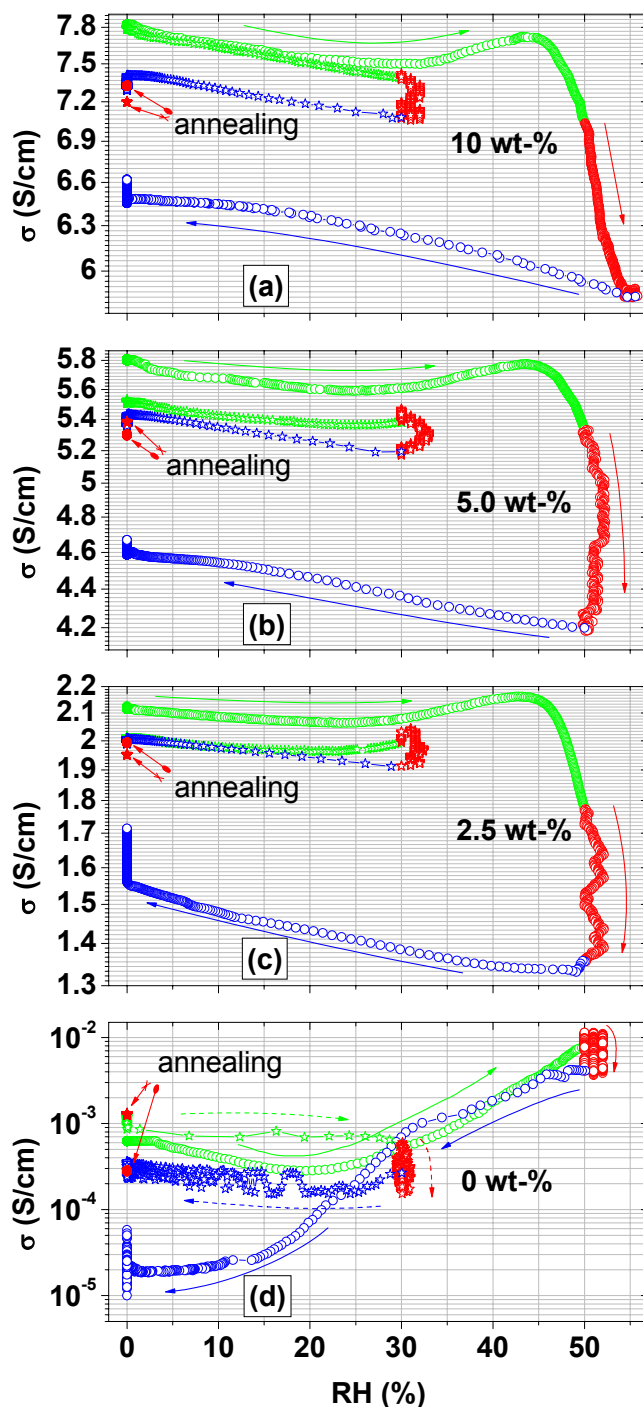


Figure 5.3: Conductivity versus relative humidity (RH) for samples with different sorbitol concentrations under medium (up to 30 % of relative humidity, open stars) and high (up to 50 % of relative humidity, open circles) moisture levels: (a) 10 wt-%, (b) 5 wt-%, (c) 2.5 wt-% and (d) 0 wt-%. Samples were kept at maximum moisture levels, i.e. about 30 % and 50 %, during 1.5 to 2 hours and annealed afterwards (closed symbols). The arrows indicate the moisture cycling, RH(%) up (green symbols), constant (red symbols) and down (blue symbols) and where the conductivity ended up after a second annealing procedure at 200 °C for 2 min (closed red dot and stars for annealing after the RH sweeps up to 30 % and 50 %, respectively).

By increasing the relative humidity of up to 50 %, the pristine sample (Figure 5.3(d)) shows first a decrease in conductivity of nearly a factor 2.5 (note

that this is almost the same amount by which the conductivity is increased during the thermal annealing procedure, see previous section and discussion section below), and then a steady increase in conductivity, finally exceeding the initial value by about one order of magnitude, suggesting ionic conduction [33]. This appears to happen above $\sim 30\%$ RH, since this effect is not clear in the RH sweep up to 30% . Following the humidity cycling in Figure 5.3(d), RH is kept constant at $\sim 50\%$ for about 1.5-2 hours during which the conductivity is slightly decreases due to the swelling from the water uptake. After that, the RH is swept down to 0% and the conductivities further decrease. In contrast, in the RH sweep up to 30% the conductivity has a very similar shape in the up and down sweeps.

Sorbitol treated samples behavior (Figure 5.3(a)-(c)) show basically the same trend among them, but are very different compared to the pristine sample. Most importantly, the relative change in conductivity is much smaller than for pristine samples, indicating an enhanced environmental stability. This is attributed to a reduced uptake of water, as will be explained in the next section. Up to 30% RH conductivity decrease slightly ($\sim 5\%$) by water uptake. Exceeding $\sim 30\%$ RH, the conductivity start to increase and reach a maximum value around 45% RH, suggesting again an ionic contribution to the overall conductivity. However, at this point, the increase in conductivity is not very high and the value barely exceeds the initial level. At maximum and constant RH level, $\sim 50\%$, conductivity is lowered and some scatter is observed. With $\sim 50\%$ RH for 1.5 – 2 hours the conductivity reach their minimal values. Finally, the RH cycling is completed when the humidity levels are taken back to 0% . During drying under N_2 atmosphere, a slight recovery of the conductivity is observed, but the values always end up below the initial ones. The exact reason for this effect is unclear at present, but it seems likely that the water absorbed by the samples causes morphological changes that are irreversible with drying at room temperature.

Figure 5.3 shows that the degrading effect of humidity on the conductivity of pristine PEDOT:PSS thin films can only be completely recovered after exposure to 30% RH. Surprisingly, this is not the case for PEDOT:PSS films with sorbitol, where the thermal annealing can even cause a further reduction of the conductivity, see solid red dot in Figure 5.3. On the other hand, after exposure to

50 % RH the subsequent thermal annealing at least partially recovers the conductivity for all samples (solid red star in Figure 5.3).

5.3.3 Water uptake

TGA of pristine and 10 wt-% samples was carried out under a wet atmosphere to measure the uptake and release of water in order to understand the (lack of) environmental stability of conductivity as described in the previous section. In the experiments the changes in sample weight were monitored during two repetitive thermal cycles involving annealing up to 200 °C and subsequent cooling, followed by a longer period at room temperature.

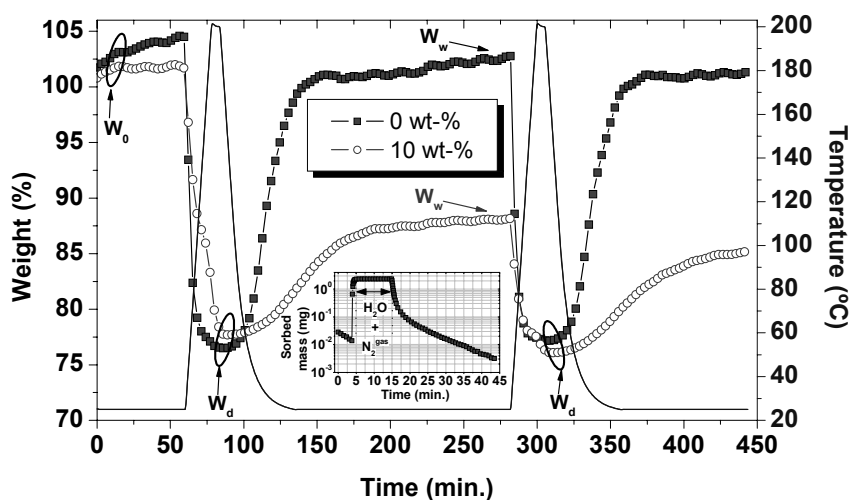


Figure 5.4: TGA of pristine PEDOT:PSS (■) and PEDOT:PSS mixed with 10 wt-% of sorbitol (○) under a moisturized atmosphere. W_0 , W_w and W_d are the weights of the fresh, wet and dry samples, respectively. The inset shows the absorbed mass of the pristine film measured with QMB when a moisturized atmosphere of 49 % RH is introduced (at $t = 6$ min.) and removed (at $t = 16$ min.).

The TGA curves in Figure 5.4 show three plateaus intercalated by two broadened valleys due to mass loss and subsequent gain which occur when both samples are annealed at 200 °C for 6 min. Both samples lose mass when increasing the temperature. During subsequent cooling a gain in mass occurs, due to the re-uptake of water, which is essentially reversible, as indicated by the second annealing step. Unlike the pristine sample, the 10 wt-% sample does not completely recover its initial mass, W_0 , after the first annealing, which is due to the evaporation of sorbitol.

The slope during the water uptake is ~ 6 times higher for the pristine sample than for the 10 wt-% sample. Also the water uptake, $([W_w - W_d]/W_d) \times 100$ %, where W_w and W_d are the weights of the wet and dry samples, is much larger for the pristine sample than for the 10 wt-% sample. The values found are 35 % and 13 %, respectively. These observations are in line with the proposed denser morphological packing of the sorbitol-treated samples, reducing the water uptake capacity and thereby improving environmental stability.

The time scale of the experiments discussed above is mainly a result of the thickness of the films in Figure 5.4, both having thickness of the order of ~ 20 μm . For a much thinner film of ~ 100 nm as used in many devices, the water uptake takes place in seconds rather than minutes, as shown by the inset of Figure 5.4 for the pristine sample. More importantly, this experiment also shows that the water uptake of thin films can be totally reversed without annealing, i.e. by purging dry N_2 . In particular, this implies that any changes in the conductivity after exposure to humidity and subsequent drying with N_2 or by pumping cannot be due to the presence of water itself.

5.3.4 Temperature dependence

In order to further investigate structural effects of the post-deposition treatments and exposure to moisturized environment on electrical transport properties, we have measured the temperature dependence in the 77-300 K range of the d.c. conductivity for the pristine sample after the conditions of no thermal annealing, thermal annealing, and exposure to 30 % RH.

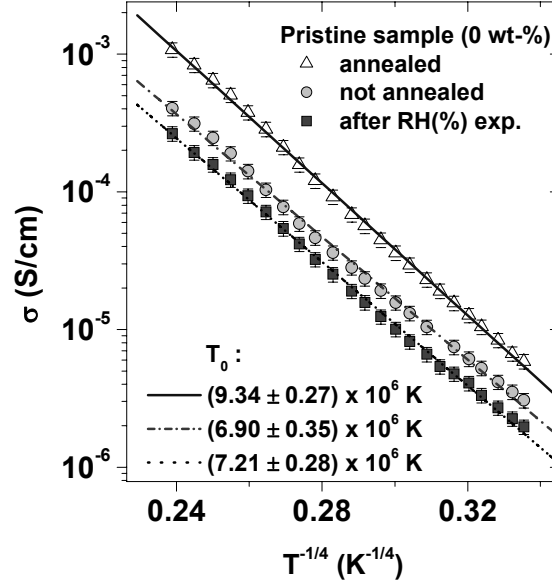


Figure 5.5: Temperature dependence of the conductivity for PEDOT:PSS thin films before any treatment (\circ), after annealing (Δ), and after exposure to humidity (\blacksquare). Lines are fits to Mott's 3D-VRH expression, see text.

In Figure 5.5, the temperature dependence of the conductivity for a pristine PEDOT:PSS thin film is, for all conditions, found to follow the Mott's 3D variable-range hopping (VRH) [34] expression $\sigma = \sigma_0 \exp\left[-(T_0/T)^\alpha\right]$. Here, σ_0 is the conductivity at infinite temperature, T_0 is the characteristic temperature and $\alpha = 1/(1+D) = 1/4$ in $D = 3$ dimensions as previously found in Chapters 3 and 4 [14,35]. The most interesting features in Figure 5.5 are the slopes characterized by the T_0 parameter. In Mott's 3D VRH model, $T_0 = \beta/(N(E_F)\zeta'^3 k_B)$, where β is a numeral factor, k_B the Boltzmann constant, $N(E_F)$ the density of states around the Fermi level and ζ' the effective localization length [35,36]. As a result, changes in the slopes in Figure 5.5 can be assigned to microscopic changes in the material upon annealing. These changes are reversible since the T_0 values for the conditions prior to any treatment and after exposure to RH are statistically equal. Moreover, since the sample chamber of the cryostat is at high vacuum during measurements, the differences in T_0 cannot arise from substantial differences in the amount of water present in the film, see previous section. Recalling that conduction in these materials takes place by hopping between PEDOT-rich grains of ~ 20 nm size [15], it is hard to imagine reversible changes in the total number of sites per unit volume N_0 . However, (de-)ionization of sulfonic acid groups on the PSS or of Na, present at a level of ~ 300 ppm in Baytron P, may affect the

energetic disorder, as reflected by the characteristic width of the density of states ΔE [36]. Since, in lowest order, $N(E_F) \sim N_0/\Delta E$, such a mechanism could explain the dependence of T_0 on sample history. Alternatively, one can tentatively attribute the observed differences in T_0 to subtle changes in the effective localization length, most likely induced by slight de-and remixing of the PEDOT and PSS phases upon the various treatments. Since the differences in T_0 are small, independent validation of the above mechanisms, e.g. by SPM techniques, is virtually impossible.

5.4 Discussion

To clarify the complex effects of the humidity dependency presented in this Chapter, we should recall the morphology of the spin coated PEDOT:PSS, which is a phase segregated material consisting of conductive PEDOT-rich grains surrounded by a shell formed by excess PSS [15,26]. The PSS is a polymer electrolyte, having a negatively charged immobile sulfonic acid group and a positively charged mobile counter ion, see Figure 5.1, and it is highly hydrophilic in nature. Hence, in this polymer electrolyte, ionic transport may occur through cations like Na^+ [14] or H^+ that jump from one sulfonic acid group to another. When the PEDOT:PSS film is hydrated, those cations are expected to become mobile above a certain threshold. In Figure 5.3, this seems to occur around 30 % RH, and a conductance channel that is parallel to the conventional electron (or hole) hopping conduction is opened. This proposition implies that below this threshold, humidity dependent changes in the conductivity must be due to changes in the conventional electron hopping channel. This seems indeed to be the case, since the reduction in conductivity when going from 0 to 30 % RH in Figure 5.3(d) is equal in magnitude to the gain in conductivity upon annealing in Figure 5.5. In the discussion of Figure 5.5 it was shown that the conduction both prior and after annealing follows Mott's VRH law, i.e. it is electronic in nature.

The relative magnitude of the ionic conduction channel, which for sorbitol-treated samples also seems to open around 30 % RH, is largest for pristine samples. However, the absolute magnitude of the ionic conduction channel is larger by an order of magnitude for the sorbitol-treated samples. Hence, the ionic

conductivity does not scale with the presence of the segregated PSS top layer [37], being most pronounced for the 0 wt-% sample [24,37,38,39]. The larger ionic conductivity of sorbitol-treated films is, however, in agreement with our previous observation that the width of the PSS lamellas separating the granular PEDOT layers seems to be enhanced by sorbitol treatment [26]. Due to the acidic and hydrophilic nature of PSS, one expects that the ionic current is mainly carried in the PSS, with the lamellas acting as the main transport channels.

5.5 Conclusions

We have studied the role of sorbitol as a typical processing additive on the conductivity of PEDOT:PSS thin films under thermal annealing and exposure to humidity. The well established conductivity enhancement caused by adding sorbitol to the aqueous dispersion, is accompanied by a remarkable increase in environmental stability after thermal annealing, as evidenced from a reduced water uptake, which we attribute to a denser packing of the PEDOT:PSS material. Up to 30 % of relative humidity, the conductivity of PEDOT:PSS is dominated by conventional variable-range hopping of electrons, which is negatively affected by the uptake of water. Exceeding 30 % of relative humidity, a parallel ionic channel starts to contribute to the total conductivity.

5.6 References and notes

- [1] V. Saxena, B. D. Malhotra, *Curr. Appl. Phys.* **2003**, 3, 293.
- [2] *Handbook of Conducting Polymers*, edited by T. A. Skotheim, J. Reynolds, 3rd ed. (CRC, Boca Raton, FL, **2007**).
- [3] L. B. Groenendaal, F. Jonas, D. Freitag, H. Pielartzik, J. R. Reynolds, *Adv. Mater.* **2000**, 12, 481.
- [4] S. Kirchmeyer, K. Reuter, *J. Mater. Chem.* **2005**, 15, 2077.
- [5] F. Jonas, W. Krafft, B. Muys, *Macromol. Symp.* **1995**, 100, 169.
- [6] M. M. de Kok, M. Buechel, S. I. E. Vulto, P. van de Weijer, E. A. Meulenkaamp, S. H. P. M. de Winter, A. J. G. Mank, H. J. M. Vorstenbosch, C. H. L. Weijtens, V. van Elsbergen, *Phys. Stat. Sol. A* **2004**, 201, 1342.
- [7] C. J. Ko, Y. K. Lin, F. C. Chen, C. W. Chu, *Appl. Phys. Lett.* **2007**, 90, 063509.
- [8] F. Verbakel, S. C. J. Meskers, R. A. J. Janssen, *Chem. Mater.* **2006**, 18, 2707.
- [9] S. C. J. Meskers, J. K. J. van Duren, R. A. J. Janssen, F. Louwet, L. Groenendaal, *Adv. Mater.* **2003**, 15, 613.
- [10] A. Kumar, D. M. Welsh, M. C. Morvant, F. Piroux, K. A. Abboud, J. R. Reynolds, *Chem. Mater.* **1998**, 10, 896.
- [11] B. Yoo, A. Dodabalapur, D. C. Lee, T. Hanrath, B. A. Korgel *Appl. Phys. Lett.* **2007**, 90, 072106.
- [12] B. Chen, T. Cui, Y. Liu, K. Varshneyan, *Solid-State Electron.* **2003**, 47, 841.
- [13] L. B. Groenendaal, G. Zotti, P. H. Aubert, S. M. Waybright, J. R. Reynolds, *Adv. Mater.* **2003**, 15, 855.
- [14] J. Huang, P. F. Miller, J. S. Wilson, A. J. de Mello, J. C. de Mello, D. D. C. Bradley, *Adv. Funct. Mater.* **2005**, 15, 290.
- [15] A. M. Nardes, M. Kemerink, R. A. J. Janssen, J. A. M. Bastiaansen, N. M. M. Kiggen, B. M. W. Langeveld, A. J. J. M. van Breemen, M. M. de Kok, *Adv. Mater.* **2007**, 19, 1196.
- [16] S. Timpanaro, M. Kemerink, F. J. Touwslager, M. M. de Kok, S. Schrader, *Chem. Phys. Lett.* **2004**, 394, 339.
- [17] J. Y. Kim, J. H. Jung, D. E. Lee, J. Joo, *Synth. Met.* **2002**, 126, 311.
- [18] F. J. Touwslager, N. P. Willard, D. M. de Leeuw, *Synth. Met.* **2003**, 135–136, 53.
- [19] L. A. A. Pettersson, S. Ghosh, O. Inganäs, *Organ. Electron.* **2002**, 3, 143.
- [20] S. K. M. Jönsson, W. R. Salaneck, M. Fahlman, *J. Electron Spectrosc., Relat. Phenom.* **2004**, 137–140, 805.
- [21] J. Ouyang, C.-W. Chu, F.-C. Chen, Q. Xu, Y. Yang, *Adv. Funct. Mater.* **2005**, 15, 203.
- [22] X. Crispin, F. L. E. Jakobsson, A. Crispin, P. C. M. Grim, P. Anderson, A. Volodin, C. van Haesendonck, M. Van der Auweraer, W. R. Salaneck, M. Berggren, *Chem. Mater.* **2006**, 18, 4354.

- [23] J. Huang, P. F. Miller, J. C. de Mello, A. J. de Mello, D. D. C. Bradley, *Synth. Met.* **2003**, 139, 569.
- [24] S. K. M. Jönsson, J. Bigerson, X. Crispin, G. Greczynski, W. Osikowicz, A. W. Denier van der Gon, W. R. Salaneck, M. Fahlman, *Synth. Met.* **2003**, 139, 1.
- [25] Direct Insert Probe-Mass Spectrometry (DIP-MS) measurements revealed that sorbitol and H₂O are almost completely removed when the films are annealed at 200 °C for 2 min.; the evaporation of sorbitol sets in at 80 °C, reaches a maximum rate at 120 °C, and vanishes around 160 °C, see Appendix A.
- [26] A. M. Nardes, M. Kemerink, R. A. J. Janssen, *submitted for publication*.
- [27] H. S. Kang, H.-S. Kang, J. K. Lee, J. W. Lee, J. Joo, J. M. Ko, M. S. Kim, J. Y. Lee, *Synth. Met.* **2005**, 155, 176.
- [28] Y. Kudoh, K. Akami, Y. Matsuda, *Synth. Met.* **1998**, 98, 65.
- [29] Y. Kudoh, K. Akami, H. Kusayanagi, Y. Matsuda, *Synth. Met.* **2001**, 123, 541.
- [30] W. A. Daoud, J. H. Xin, Y. S. Szeto, *Sens. Actuators B Chem.* **2005**, 86, 330.
- [31] D. Nilsson, T. Kugler, O. Svensson, M. Berggen, *Sens. Actuators B Chem.* **2002**, 86, 193.
- [32] K. Kawano, R. Pacios, D. Poplavskyy, J. Nelson, D. D. C. Bradley, J. R. Durrant, *Sol. Energy Mater. Sol. Cells* **2006**, 90, 3520.
- [33] C. Carlberg, X. Chen, O. Inganas, *Solid State Ionics* **1996**, 85, 73.
- [34] N. Mott, E. A. Davis, *Electronic Processes in Non-Crystalline Materials*, Clarendon Press, Oxford, **1979**.
- [35] A. M. Nardes, M. Kemerink, R. A. J. Janssen, *Phys Rev. B.* **2007**, 76, 085208.
- [36] J. Zhang, B. I. Shklovskii, *Phys. Rev. B* **2004**, 70, 115317.
- [37] G. Greczynski, T. Kugler, M. Keil, W. Osikowicz, M. Fahlman, W. R. Salaneck, *J. Electron Spectrosc. Relat. Phenom* **2001**, 121, 1.
- [38] J. Hwang, F. Amy, A. Kahn, *Org. Electron.* **2006**, 7, 387.
- [39] H. J. Snaith, H. Kenrick, M. Chiesa, R. H. Friend, *Polymer* **2005**, 46, 2573.

Surface potential of PEDOT:PSS thin films studied by scanning Kelvin probe microscopy

This Chapter discusses the role of the surface layer of sorbitol-treated PEDOT:PSS thin films by simultaneously studying the work function and the surface morphology. Work function shifts are measured by scanning Kelvin probe microscopy. The observed upward shift upon sorbitol treatment is consistent with earlier observations of the increase of the PEDOT to PSS ratio at the sample surface.

6.1 Introduction

In the last few years, there has been an increasing interest in organic electronics due to the promise of low cost and highly efficient devices [1]. Examples of organic devices range from sensors and organic photovoltaic (PV) cells to organic light emitting diodes (OLEDs). Poly(3,4-ethylenedioxythiophene) doped with poly(styrenesulfonic acid) (PEDOT:PSS) has demonstrated great performance in virtually all of these applications. For example, covering the ITO anode by PEDOT:PSS reduces the operating voltage and increases the device lifetime remarkably in OLEDs [2], which was attributed to a lower hole injection barrier between the active layer and PEDOT:PSS as well as to a smoothening of the ITO surface.

However, the use of PEDOT:PSS thin films brings along other consequences and issues. The spin coated thin films exhibit a complex three dimensional distribution of PEDOT and PSS [3,4,5] and this morphology largely determines the film's electrical properties. Moreover, typical PEDOT:PSS dispersions contain substantial amounts of excess PSS that segregates from the PEDOT:PSS complex. Because PSS is a poor (ionic) conductor, an excess of PSS limits the film conductivity [5]. PSS is also known to degrade the performance of OLEDs over time by its acidic attack on indium tin oxide (ITO) anodes [6] and, by segregating to the surface, plays a major role in determining the work function of thin films [7].

Several applications require control of the electrode work function χ . For PEDOT:PSS thin films, a range of work functions is reported from 4.7 to 5.4 eV [8,9,10,11] and it has been found that this level can be tuned so as to minimize the hole-injection barrier at the anode [12] in organic LEDs [13,14] and PV cells [15]. The spread in work function values is assumed to be related to differences in the top layer, which may contain an excess of PSS [7,16,17,18]. The PSS-rich top layer may be modified by the addition of a high-boiling solvent to the aqueous PEDOT:PSS dispersion [16,17,18] or (non-)intentionally by other processing conditions [19].

For the above reasons accurate understanding of and control over the PEDOT:PSS surface morphology is crucial. This Chapter aims to bring further insights into the consequences of the addition of sorbitol to the PEDOT:PSS

aqueous solution. In particular the changes in the film work function in relation to the morphology at the surface are studied. Using scanning Kelvin probe microscopy (SKPM) we find that the work function of PEDOT:PSS thin films is indeed reduced by sorbitol treatment. Additionally, a shift to higher values with time is seen while constantly scanning the sample. This is found to be a spurious effect, resulting from the measurement procedure.

6.2 Experimental

Sample preparation for electrical measurements (lateral direction, ||) follows the procedure described in Chapter 3, section 3.2 on page 41.

The PEDOT:PSS aqueous solution (Baytron P VP Al 4083 from H. C. Starck) was mixed with D-sorbitol 97 % (Sigma-Aldrich) in different concentrations, 2.5 wt-%, 5.0 wt-%, and 10 wt-%. The solutions were stirred for at least 24 h at room temperature and spin coated after filtration through a 5 μm filter. The samples were then transferred to a glove box filled with N_2 (O_2 and H_2O < 1 ppm) for a subsequent annealing step to remove H_2O and sorbitol.

The conductivity was optimized as a function of annealing temperature and time using a Keithley 2410 sourcemeter. The standard procedure was set to 200 $^\circ\text{C}$ and 2 min and samples annealed under this condition were subjected to surface potential measurements by scanning Kelvin probe microscopy (SKPM). SKPM and tapping mode AFM measurements were made with a Veeco MultiMode AFM, driven by an extended NanoScope IIIa controller, using conductive Pt coated tips (Olympus OMCL-AC240TM-B2, spring constant $k \approx 2$ N/m), inside a glove box. SKPM combines classical Kelvin probe with AFM and allows one to measure the local surface potential V_{sp} , which, for a metallic tip and sample with work functions χ_{tip} and χ_{sample} respectively, is given by $qV_{sp} = \chi_{tip} - \chi_{sample}$ with q the elementary charge.

6.3 Results and discussion

6.3.1 Conductivity enhancement

The electrical conductivity of PEDOT:PSS thin films, processed from an aqueous dispersion containing sorbitol in different concentrations, is presented in Figure 6.1 as a function of annealing temperature and annealing time. The electrical conductivity of the pristine PEDOT:PSS film, i.e. cast without using sorbitol, is $(1.2 \pm 0.2) \times 10^{-3}$ S/cm when annealed at 200 °C for 2 min, which is in excellent agreement with the manufacturer's specifications [20]. Interestingly, without further annealing or at annealing temperatures below ~ 100 °C, the addition of sorbitol has little effect on the conductivity. The electrical conductivity of the sorbitol-added samples increases significantly only after bake-out at temperatures above 150 °C and saturates at 200 °C. This may be attributed to the simultaneous evaporation of sorbitol and remnant water. Modulated-differential scanning calorimetry (MDSC) and direct insertion probe-mass spectrometry (DIP-MS) analysis have shown that simultaneous evaporation of sorbitol and water starts at 80 °C, reaching a maximum rate at 120 °C and is vanished at 160 °C [21], in agreement with the trends found in Figure 6.1(a). More detailed annealing studies are shown in Chapter 5.

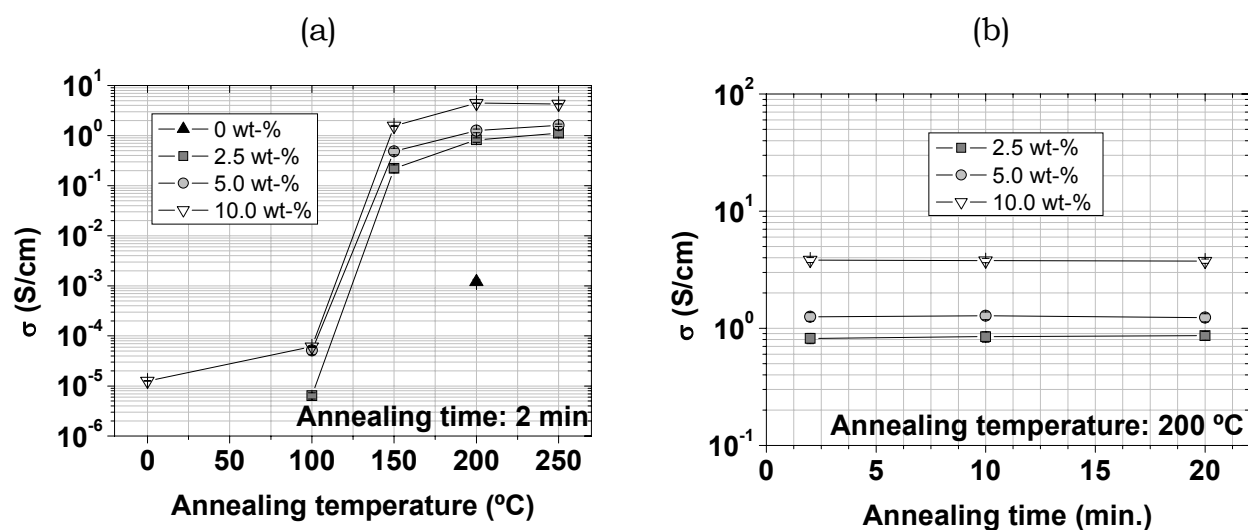


Figure 6.1: Conductivity versus (a) annealing temperature and (b) annealing time for PEDOT:PSS thin films mixed with 2.5, 5, and 10 wt-% sorbitol. For comparison, the pristine film (0 wt-%) is also shown.

Figure 6.1(b) shows that the enhanced conductivities are independent of annealing time. Even after 20 min no significant change in conductivity is observed. Therefore, in terms of conductivity, Figure 6.1(a) and (b) enable us to set the optimal annealing temperature and time to 200 °C and 2 min.

The removal of sorbitol and water during annealing and the reported plasticizing effect of the solvent mixture enable the PEDOT and PSS clusters to rearrange in a more relaxed and compact morphology [22,23,24,25]. The addition of sorbitol leads to an increase in the size of the conductive PEDOT-rich particles or clusters [3,26]. Figure 6.2 shows the morphological changes as observed in topographic AFM images. Although the topographic AFM images show that all films are very flat, having a vertical scale of only 5 nm, the rms-roughness continuously increases from 1.05 nm (0 wt-%) to 2.36 nm (10 wt-%) with increasing sorbitol concentration used in the aqueous dispersion for spin coating. This is in line with the increasing cluster size reported before [18]. Alternatively, the increasing roughness can be taken as being due to a thinning of the smooth PSS-rich top layer that covers the rougher bulk material [3,26].

In the next section, surface potential measurements will give more insight on this issue.

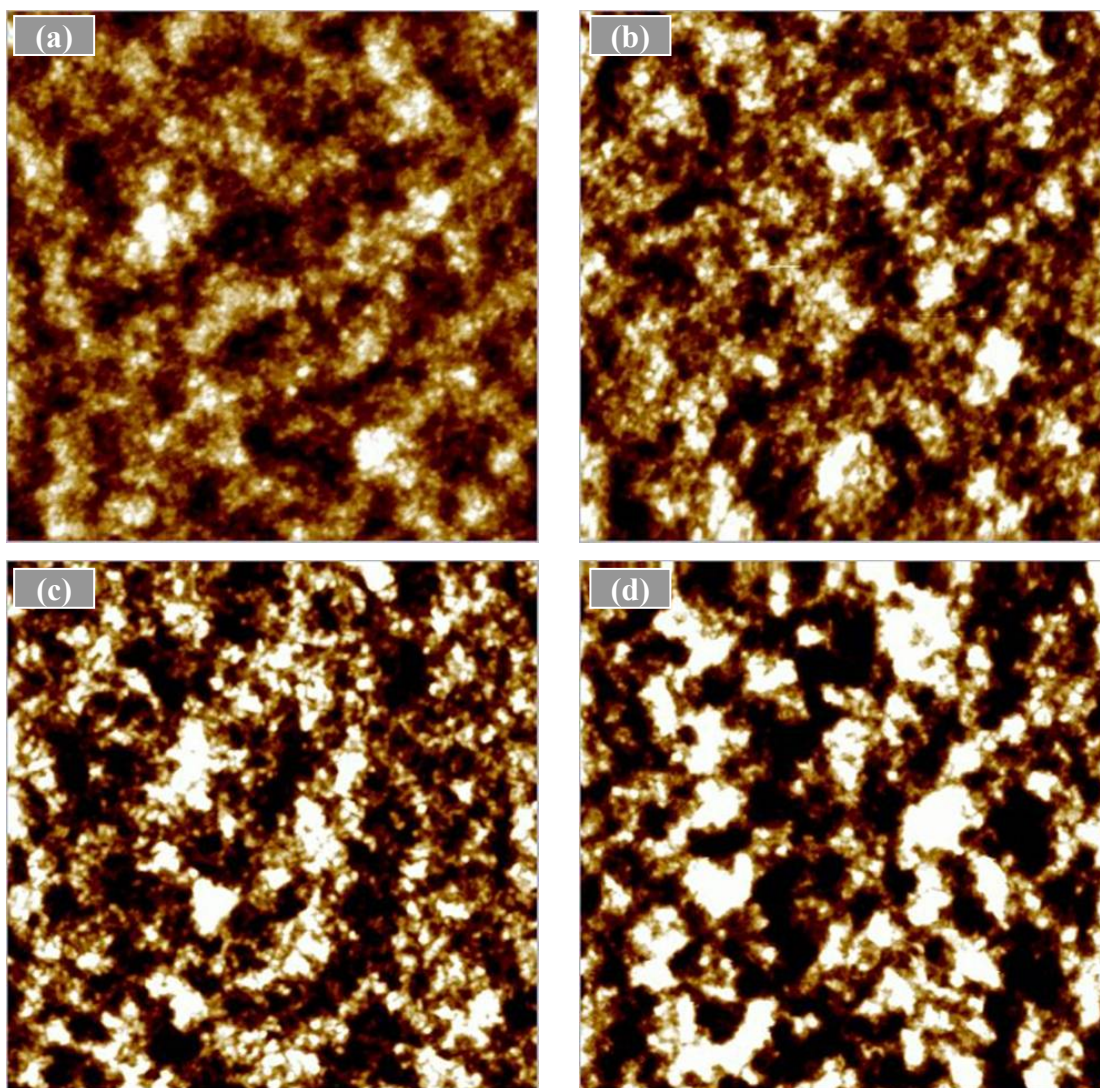


Figure 6.2: $2 \times 2 \mu\text{m}^2$ topographic AFM images of PEDOT:PSS thin films processed from an aqueous dispersion containing sorbitol in different concentrations: (a) 0 wt-% (pristine); (b) 2.5 wt-%; (c) 5 wt-%; (d) 10 wt-%. The rms-roughness is 1.05, 1.38, 1.76, and 2.36 nm, respectively. The vertical scale is 5 nm for all images.

6.3.2 Surface potential analysis

The surface potential relates to the work function as $qV_{sp} = \chi_{tip} - \chi_{sample}$, as stated earlier, where χ_{tip} and χ_{sample} are the work functions of the tip and sample, respectively. Upon addition of sorbitol, a shift from ~ 5.1 eV (0 wt-%) to ~ 4.8 eV (10 wt-%) in the work function of PEDOT:PSS thin films is observed.

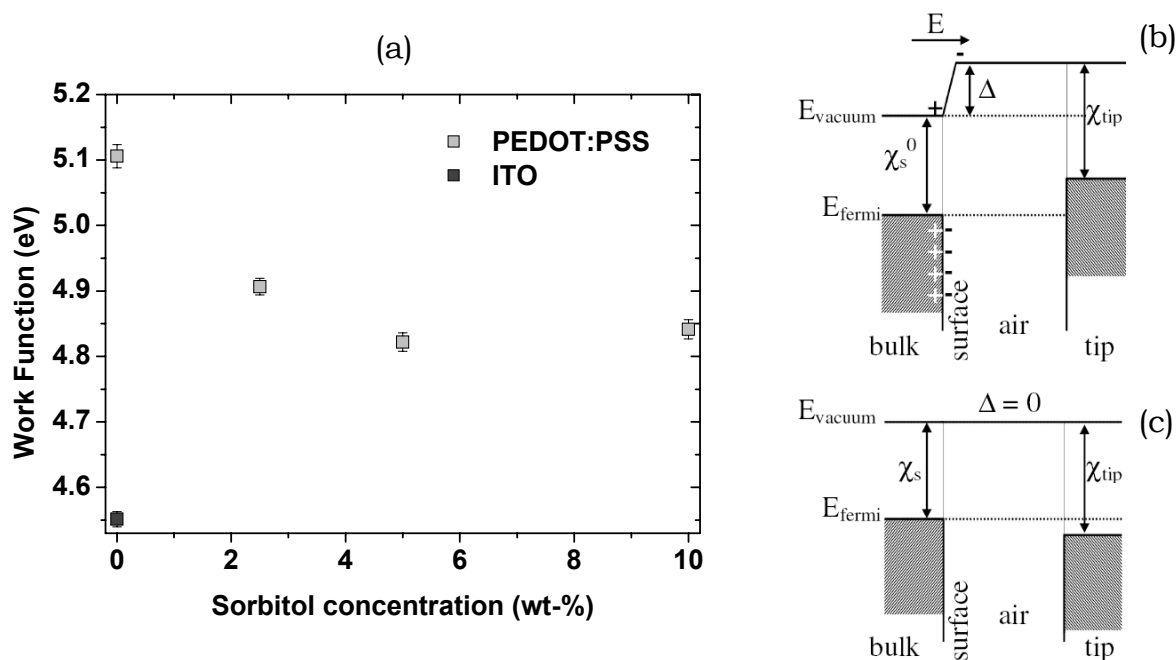


Figure 6.3: (a) Work function of PEDOT:PSS thin films spin cast from solutions with different sorbitol concentrations. The work function of ITO is shown for comparison. (b+c) Schematic representation of the band diagrams during SKPM on PEDOT:PSS thin films. (b) pristine PEDOT:PSS with a PSS-rich surface layer and (c) sorbitol-treated PEDOT:PSS without PSS surface layer. χ_s^0 , χ_s and χ_{tip} , are respectively the work functions of ‘bulk’ PEDOT:PSS, sorbitol-treated PEDOT:PSS thin film, and the tip. Δ is the surface dipole due to the PSS-rich surface layer, which effectively enhances the film work function to $\chi_s^0 + \Delta$.

Using highly oriented pyrolytic graphite (HOPG) as work function reference, $\chi_{HOPG} = 4.475 \pm 0.005$ eV [27], the measured V_{sp} is translated into the work function values of PEDOT:PSS thin films shown in Figure 6.3(a). HOPG is chosen as reference due to its work function stability, independent of the measurement conditions, i.e. in vacuum, air, or under inert atmosphere [27]. Furthermore, a fresh and clean surface of HOPG can easily be obtained by removing the topmost layers with adhesive tape.

The shift in the surface potential, i.e. a shift in the work function, is consistent with a removal of the PSS-rich surface layer as explained in the band diagrams of Figure 6.3(b) and (c). The (positive) sign of the work function change with increasing sorbitol content leads to the conclusion that the PSS-rich top layer results in an inward directed surface potential dipole as indicated in Figure 6.3(b) [28]. Compared to the situation without this dipole layer, see Figure 6.3(c), the work function is effectively increased, the magnitude of the shift Δ depending on the surface layer thickness. Hence, upon reduction of the surface layer

thickness by sorbitol treatment, the work function will decrease, i.e. the surface potential will increase, as observed in the SKPM measurements.

Interestingly, it is observed that for each individual sample, the surface potential also shifts in time. For all samples, the surface potential was measured on approximately 17 min intervals, on the same spot ($500 \times 500 \text{ nm}^2$) with the same feedback parameters. Consecutive measurements showed, for all samples, an exponentially saturating shift to higher values. One could attribute this to an ongoing contamination of the SKPM-tip during the measurements. However, all measurements in Figure 6.3(a) were conducted using different cantilevers and these were all calibrated by measuring the V_{sp} of the reference HOPG sample, before and after each PEDOT:PSS sample. Hence, tip contamination can be excluded.

In order to shed light into this issue, we further studied the AFM-phase images of the PEDOT:PSS samples. Since the phase of the oscillating cantilever in TM-AFM is sensitive to the material composition [29], the presence of multiple phases in a blend, in this case PEDOT and PSS, generally leads to a phase contrast [4,30].

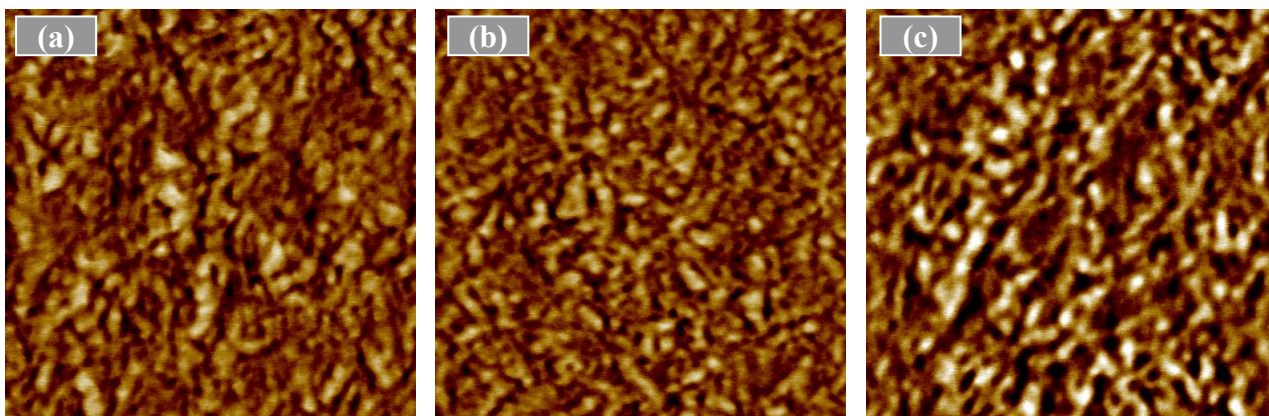


Figure 6.4: $500 \times 500 \text{ nm}^2$ TM-AFM phase images of PEDOT:PSS thin films: (a) first image acquired at $t = 0$ for a PEDOT:PSS thin film processed from an aqueous dispersion containing 10 wt-% sorbitol; (b) same as (a) for $t \sim 7$ hours; (c) same as (a) for $t \sim 14$ hours. Vertical scale is 15° for all images

Previously (Chapter 3), dark and bright features in the AFM phase images were interpreted as PEDOT-rich and PSS-rich regions, respectively [3]. For example, Figure 6.4(a)-(c) show the phase image of a PEDOT:PSS thin film processed from an aqueous dispersion containing 10 wt-% sorbitol. The initial V_{sp} value measured in Figure 6.4(a) is $(19 \pm 5) \text{ mV}$ and after ~ 7 hours the last V_{sp}

value recorded is (78 ± 3) mV. Next, the tip is withdrawn and re-engaged after ~ 14 hours yielding a measured V_{sp} of again (24 ± 3) mV.

It is not clear why the V_{sp} of the PEDOT:PSS samples shifts during measurements, especially since no significant morphological changes are observed in the phase images of Figure 6.4(a) and (b) (recall that the measurements were conducted in a glove box with H_2O and O_2 levels < 1 ppm). In Figure 6.4(c), the phase contrast is somewhat increased, whereas V_{sp} is found to be shifted back to its initial value. Apparently the (unknown) cause of the temporal work function shift is measurement-induced and not accompanied by significant changes in the top layer morphology. Conversely, the slight enhancement in the phase contrast, which one could interpret in terms of more pronounced phase separation, does not lead to a measurable work function shift.

6.4 Conclusions

The addition of sorbitol to a PEDOT:PSS solution prior to spin coating enhances the electrical conductivity of the dried films by three orders of magnitude after annealing. The optimal annealing time and temperature, in terms of conductivity, are found to be $200\text{ }^\circ\text{C}$ and 2 min. , respectively. The morphological changes due to addition of sorbitol are accompanied by changes in the work function of the PEDOT:PSS thin films, which we attribute to an increase in the ratio of PEDOT to PSS at the surface upon addition of sorbitol. Minor shifts of the work function in time are found to be measurement-induced and to be uncorrelated to the surface morphology as visualized in AFM phase images.

6.5 References and notes

- [1] S. R. Forrest, *Nature* **2004**, 428, 911.
- [2] A. Elschner, F. Bruder, H.-W. Heuer, F. Jonas, A. Karbach, S. Kirchmeyer, S. Thurm, R. Wehrmann, *Synth. Met.* **2000**, 111-112, 139.
- [3] S. Timpanaro, M. Kemerink, F. J. Touwslager, M. de Kok, S. Schrader, *Chem. Phys. Lett.* **2004**, 394, 339.
- [4] A. M. Nardes, M. Kemerink, R. A. J. Janssen, J. A. M. Bastiaansen, N. M. M. Kiggen, B. M. W. Langeveld, A. J. J. M. van Breemen, M. M. de Kok, *Adv. Mater.* **2007**, 19, 1196.
- [5] M. Kemerink, S. Timpanaro, M. de Kok, E. A. Meulenkaamp, F. J. Touwslager, *J. Phys. Chem. B* **2004**, 108, 18820.
- [6] A. M. Higgins, S. J. Martin, P. C. Jukes, M. Geoghegan, R. A. L. Jones, S. Langride, R. Cubitt, S. Kirchmeyer, A. Wehrum, I. Grizzi, *J. Mater. Chem.* **2003**, 13, 2817.
- [7] J. Hwang, F. Amy, A. Kahn, *Org. Electron.* **2006**, 7, 387.
- [8] J. C. Scott, G. Malliaras, W. D. Chen, J. Breach, J. Salem, P. Brock, S. Sachs, C. Chidsey, *Appl. Phys. Lett.* **1999**, 74, 1510.
- [9] G. Greczynski, T. Kugler, M. Keil, W. Osikwicz, M. Fahlman, W. R. Salaneck, *J. Electron Spectrosc. Relat. Phenom* **2001**, 121, 1.
- [10] A. J. Makinen, I. G. Hill, R. Shashindhar, N. Nikolov, Z. H. Kafafi, *Appl. Phys. Lett.* **2001**, 79, 557.
- [11] N. Koch, A. Kahn, J. Ghijsen, J.-J. Pireaux, J. Schwartz, R. L. Johnson, A. Elschner, *Appl. Phys. Lett.* **2003**, 82, 70.
- [12] F. Zhang, A. P. Peisert, M. Knupfer, L. Dunsch, *J. Phys. Chem. B* **2004**, 108, 17301.
- [13] P. K. H. Ho, J.-S. Kim, J. H. Burroughes, H. Becker, F. Y. L. Sam, T. M. Brown, F. Cacialli, R. H. Friend, *Nature* **2000**, 404, 481.
- [14] H. Frohne, D. C. Muller, K. Meerholz, *Chem. Phys. Chem.* **2002**, 3, 707.
- [15] H. Frohne, S. E. Shaheen, C. J. Brabec, D. C. Muller, N. S. Sariciftci, K. Meerholz, *Chem. Phys. Chem.* **2002**, 3, 795.
- [16] S. K. M. Jönsson, J. Bigerson, X. Crispin, G. Greczynski, W. Osikowicz, A. W. Denier van der Gon, W. R. Salaneck, M. Fahlman, *Synth. Met.* **2003**, 139, 1.
- [17] H. J. Snaith, H. Kenrich, M. Chiesa, R. H. Friend, *Polymer* **2005**, 46, 2573.
- [18] J. Huang, P. F. Miller, J. S. Wilson, A. J. de Mello, J. C. de Mello, D. D. C. Bradley, *Adv. Funct. Mater.* **2005**, 15, 290.
- [19] N. Koch, A. Vollmer, A. Elschner, *Appl. Phys. Lett.* **2007**, 90, 043512.
- [20] www.baytron.com
- [21] A. M. Nardes, X. Lou, J. L. J. van Dongen, *Unpublished results*.
- [22] X. Crispin, S. Marciniak, W. Osikowicz, G. Zotti, A.W. Denier Van Der Gon, F. Louwet, M. Fahlman, L. Groenendaal, F. De Schryver, W.R. Salaneck, *J. Polym. Sci. B* **2003**, 41, 2561.

- [23] L. A. A. Pettersson, S. Ghosh, O. Inganäs, *Org. Electron.* **2002**, 3, 143.
- [24] S. K. M. Jonsson, J. Birgersson, X. Crispin, G. Greczynsky, W. Osikowicz, A. W. D. van der Gon, W. R. Salaneck, M. Fahlman, *Synth. Met.* **2003**, 139, 1.
- [25] W. H. Kim, G. P. Kushto, H. Kim, Z. H. Kafafi, *J. Polym. Sci. B* **2003**, 41, 2522.
- [26] A. M. Nardes, M. Kemerink, R. A. J. Janssen, *submitted*.
- [27] W. N. Hansen, G. J. Hansem, *Surf. Sci.* **2001**, 481, 172.
- [28] Although PEDOT:PSS is quasi metallic, it is actually a semiconductor, which means that locally net charge densities can be formed. Only partial screening of the surface dipole by mobile cations (mostly Na⁺) is expected, since, at a typical Na concentration of 300 ppm, the screening length is large compared to the surface layer thickness of a few nm.
- [29] a) J. P. Cleveland, B. Anczykowski, A. E. Schmid, V. B. Elings, *Appl. Phys. Lett.* **1998**, 72, 2613. b) D. Raghavan, M. VanLandingham, X. Gu, T. Nguyen, *Langmuir* **2000**, 16, 9448. c) X. Crispin, F. L. E. Jakobsson, A. Crispin, P. C. M. Grim, P. Anderson, A. Volodin, M. Van der Auweraer, W. R. Salaneck, M. Berggren, *Chem. Mater* **2006**, 18, 4354.
- [30] X. Crispin, F. L. E. Jakobsson, A. Crispin, P. C. M. Grim, P. Anderson, A. Volodin, C. van Haesendonck, M. Van der Auweraer, W. R. Salaneck, M. Berggren, *Chem. Mater.* **2006**, 18, 4354.

A morphological model for solvent-induced conductivity enhancement in PEDOT:PSS thin films

The well-known conductivity enhancement of poly(3,4-ethylenedioxythiophene):poly(4-styrenesulfonate) (PEDOT:PSS) thin films by addition of high-boiling-point solvents like sorbitol is shown to result from a rearrangement of PEDOT-rich clusters into elongated domains. The changing film morphology is followed by STM and AFM, whereas the charge transport mechanism is derived from temperature dependent conductivity measurements. The experimental results are combined into a quantitative morphological model that explains, amongst others, the observed transition from 3D to 1D variable-range hopping conduction.

7.1 Introduction

The performance of (opto)electronic devices based on organic and polymer materials as active layer or electrodes is found to be closely related to mesoscopic (dis)order and other morphological properties of the active materials [1,2,3,4]. For that reason, it is crucial to understand the effects of molecular arrangement on the electronic properties of organic materials and organic-based devices. A detailed comprehension on how charges move through the material is probably the best feedback to assist in the aforementioned development of novel devices. Hence, considerable efforts have been made to improve and understand the charge transport characteristics of these materials [5]. Temperature dependent conductivity measurements are likely the most direct way to experimentally study the mechanism of charge transport in organic conjugated systems and the results can directly be compared with predictions of theoretical models [6,7]. However, a common problem in charge transport studies on organic materials is a lack of detailed knowledge of the morphology.

A good example of this problem is the well-known but poorly understood highly conducting state of PEDOT:PSS, obtained by the addition of high-boiling solvents or polar compounds to the water-borne dispersion [8,9,10,11,12,13]. Technologically, highly conducting PEDOT:PSS opens opportunities to replace the well-known but expensive inorganic indium tin oxide (ITO) as anode in optoelectronic devices, like organic photovoltaic cells [14,15] and organic light-emitting diodes [16,17,18,19], and forms a good candidate for electrodes for field-effect transistors [20] and circuits in general [21].

The origin of this conductivity increase has been tentatively explained in the literature and related to changes on (i) a nanoscopic level such as increase in interchain interactions [9,11], conformational changes in PEDOT chains [22], and screening effects between polymer and dopant due to the polar solvent [22], or to changes on (ii) a mesoscopic level leading to the formation of larger particles with concomitant reduction of the PPS shell and increased hopping between particles [15,18,23,24,25,26]. However no strong consensus among the explanations has been found. Typically, the temperature dependent conductivity in doped organic materials like PEDOT:PSS can be described in the framework of variable-range hopping (VRH) as:

$$\sigma = \sigma_0 \exp \left[- \left(\frac{T_0}{T} \right)^\alpha \right] \quad \text{Eq 7.1}$$

In Eq. 7.1, σ_0 is the conductivity at infinite temperature, T_0 is the characteristic temperature and α the exponent that in standard VRH theory is equal to $1/(1+D)$, where D is dimensionality of the system. Assuming that the density of the states near the Fermi level $N(E_F)$ is either constant or varies smoothly with energy, Mott [6] obtained $\alpha = 1/4$ in three dimensions (3D). Straightforward application of Eq. 7.1 to 1D systems turned out to be problematic because of the presence of ‘blocking sites’ in infinitely long 1D chains. However, Shante *et al.* [27] have shown that the conductivity of ‘real’ systems, consisting of a large number of parallel 1D chains of finite length, can be described by Eq. 7.1. Later it was shown that for both 2D and 3D-VRH systems at (very) low temperatures $\alpha = 1/2$ can also result from long-range electron-electron interactions which give rise to a Coulomb gap in $N(E_F)$ [7]. Finally, $\alpha = 1/2$ has also been interpreted in terms of a charging-energy-limited tunneling model [28,29,30]. However, in this model a proportionality between (insulating) shell thickness and core diameter of the metallic particles is required, for which, in the case of PEDOT:PSS, no experimental indications are found.

Previous studies on the effect of addition of solvents or solvent compounds to the spin coated solution on the charge transport properties of PEDOT:PSS films have shown that the conductivity can be enhanced by several orders of magnitude, depending on the solvent/compound. Kim *et al.* [10] found that $\sigma(T)$ of PEDOT:PSS deposited from pure H₂O followed a quasi 1D-VRH model, while that of highly conductive PEDOT:PSS deposited with organic solvents followed a power law $\sigma(T) \sim T^\alpha$, with α varying from 0.54 to 1.2. Ouyang *et al.* [31] and Ashizawa *et al.* [32] have also described their results for ethylene glycol treated PEDOT:PSS using the 1D-VRH model. In contrast, Crispin *et al.* [18] concluded that upon addition of diethylene glycol a three-dimensional conducting network is formed, which in principle should lead to $\alpha = 1/4$. Their X-ray photoelectron spectroscopy (XPS) studies indicated that sorbitol and diethylene glycol induce a morphology change at the surface of PEDOT:PSS and these results were interpreted as a segregation of the excess PSS. However, no clear connection was

made between the topography of the film and XPS measurements [23,33]. Timpanaro *et al.* [24] have shown with scanning tunneling microscopy that the addition of sorbitol leads to an increase in the apparent size of the PEDOT-rich particles, which is associated with the increase of conductivity. Thus, the morphology change in the PEDOT:PSS appears to be another plausible mechanism to explain the high conductivity of PEDOT:PSS. In conclusion, the conductivity enhancement is well established, but the responsible mechanism has been controversial. The present study aims to resolve this problem.

This Chapter reports a study of the temperature dependence of the d.c. conductivity of sorbitol-treated PEDOT:PSS, both in low and moderate electric fields, in combination with a morphology analysis by scanning probe microscope (SPM) techniques. The transition from 3D to quasi 1D-VRH conduction that is found upon addition of sorbitol appears to be due to a rearrangement of PEDOT-rich particles into elongated and aligned clusters in which the charge transport takes place. The characteristic hopping distance matches well with the observed size of the PEDOT particles. Finally, the conductivity enhancement is attributed to an increased effective localization length.

7.2 Experimental

To the PEDOT:PSS aqueous dispersion (Baytron P VP Al 4083), 2.5 wt-%, 5.0 wt-% and 10 wt-% of D-sorbitol 97% (Sigma-Aldrich) were added and stirred for at least 24 h at room temperature. Solutions were filtered, and deposited in air by spin coating technique on substrates with appropriate electrodes for electrical characterization (4 and/or 2-point probe techniques). The annealing step was done under inert atmosphere. All the sample preparation and electrical measurements are described in details in Chapter 3, section 3.2. The thickness of the thin films treated with sorbitol was 90-100 nm and the pristine film ~ 60 nm as measured by the profilometer.

Scanning tunneling microscopy (STM) and tapping mode cross-sectional atomic force microscopy (X-AFM) experiments is also referred to section 3.2. The tips (PPP-NCHR from NanoSensors) used in this experiment had a spring constant $k \approx 20$ N/m.

7.3 Results

7.3.1 Charge transport

For the temperature-dependent conductivity of all three different sorbitol contents studied in this Chapter, a good fit is obtained to the variable-range hopping model (Eq. 7.1) as demonstrated in Figure 7.1. In fact, the correct exponent α in Eq. 7.1 was determined as the α value at which the correlation coefficient R of the fit in Figure 7.1 reached a maximum. These fits were sufficiently sharp and the best α values, using this approach, have more than 96 % of accuracy for all samples. The upper right inset of Figure 7.1 shows R of the fit of Eq. 7.1 to the measured conductivity plotted versus the exponent α . The optimal α values are shown in Table 7.I, and are very close to $1/2$, which we interpret as indicative of quasi 1D-VRH. Alternative interpretations of this finding are discussed at the end of this section.

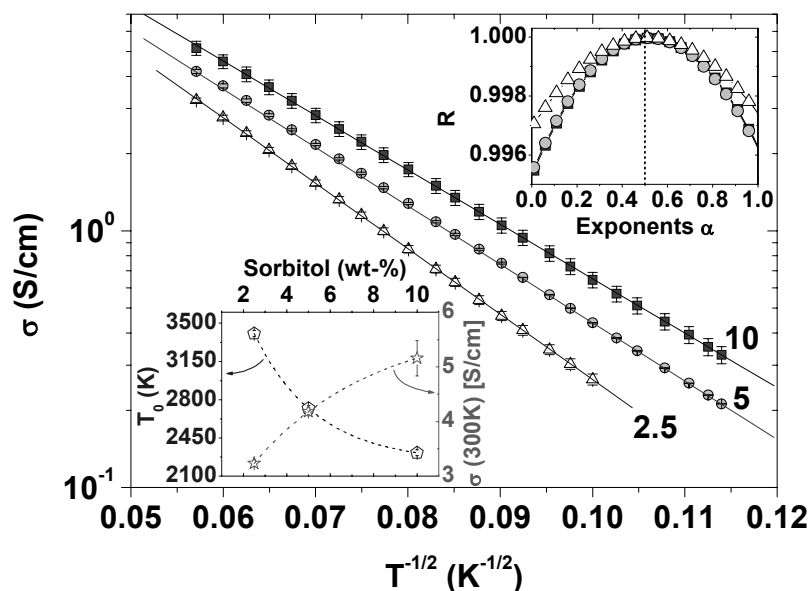


Figure 7.1: Temperature dependence of the conductivity for PEDOT:PSS samples with (Δ) 2.5 wt-%, (\circ) 5 wt-% and (\blacksquare) 10 wt-% of sorbitol concentration added to the aqueous dispersion used for spin coating of the films. Straight lines are fits to Eq. 7.1. Upper right inset: analysis of the exponent α for the whole temperature range, i.e. the correlation coefficient R of the fit of Eq. 7.1 to the data in the main panel plotted versus α . The vertical dashed line represents $\alpha = 1/2$. Lower left inset: evolution of T_0 and σ at 300 K as a function of sorbitol concentration, the dashed lines serves to guide the eye. The values of these parameters are also shown in Table 7.I.

Table 7.I: Parameters describing the electrical conduction in sorbitol-enhanced PEDOT:PSS thin films.

	2.5 wt-%	5 wt-%	10 wt-%
σ at 300 K (S/cm)	3.24 ± 0.06	4.18 ± 0.07	5.2 ± 0.3
α (77 K-307 K)	0.52 ± 0.01	0.53 ± 0.02	0.52 ± 0.01
T_0 (K)	3406 ± 26	2720 ± 27	2314 ± 27
σ_0 (S/cm)	91.3 ± 1.3	83.3 ± 1.4	81.7 ± 1.5
$N(E_F)$ (eV·cm³)⁻¹	$(1.9 \pm 0.4) \times 10^{18}$	n.d.	$(1.8 \pm 0.3) \times 10^{18}$
ξ' (nm)	33 ± 2	n.d.	44 ± 3
L (nm)	60-80	n.d.	65-95

Once the transport mechanism is identified as 1D VRH, the other parameters in Eq. 7.1 can also be discussed. The slopes of the curves in Figure 7.1 represent the quantity $-T_0^{1/2}$, where T_0 is given by

$$T_0 = \frac{4}{k_B N(E_F) \xi'} \quad \text{Eq 7.2}$$

Here, ξ' is the effective localization length, $N(E_F)$ is the density of (localized) states at the Fermi level, k_B is the Boltzmann's constant [27]. The systematic variation of T_0 and σ at 300 K as a function of sorbitol concentration is shown in the lower left inset of Figure 7.1. T_0 drops and σ (300 K) increases by addition of sorbitol to the aqueous PEDOT:PSS dispersion up to 10 wt-%. Coincidentally, they both vary by a similar fraction. Common explanations for this behavior suggest a lower energy barrier between the hopping sites and/or a longer localization length of the charge and/or an increasing of $N(E_F)$ [31,32]. However, authors have only looked at the variation of T_0 , which indeed depends on $N(E_F)$ and ξ' , see Eq. 7.2, but no quantitative analysis has been made so far. In order to clarify this issue, we measured the electric field dependence of the conductivity, which allows one to extract the characteristic length scales of the hopping process.

As the electric field is increased, deviations from Ohmic behavior become evident. In Figure 7.2, the electric field dependence of the conductivity is plotted at different temperatures for 2.5 wt-% and 10 wt-% of sorbitol. The electric field dependent conductivity $\sigma(F)$ for hopping in a disordered systems in moderate electric fields F is of the general form [34,35]:

$$\sigma(T, F) = \sigma(T, 0) \exp\left(c \frac{eFL}{k_B T}\right) \quad \text{Eq 7.3}$$

Here, eFL is the energy that electrons can pick-up from the electric field in one hop which, at intermediate fields, is comparable to the activation energy of the dominant or characteristic hop. In this term, L is the characteristic hopping length and e the electronic charge. The prefactor c accounts for the fact that not all critical hops are in the direction of the applied field, and different authors predict different values for c , depending on the assumptions made. In the following analysis we will use Eq. 7.3 with $c = 1$, mainly because of the absence of an applicable theory for non-Ohmic quasi 1D-VRH. As a result, the extracted hopping lengths should be considered a lower limit to the real value.

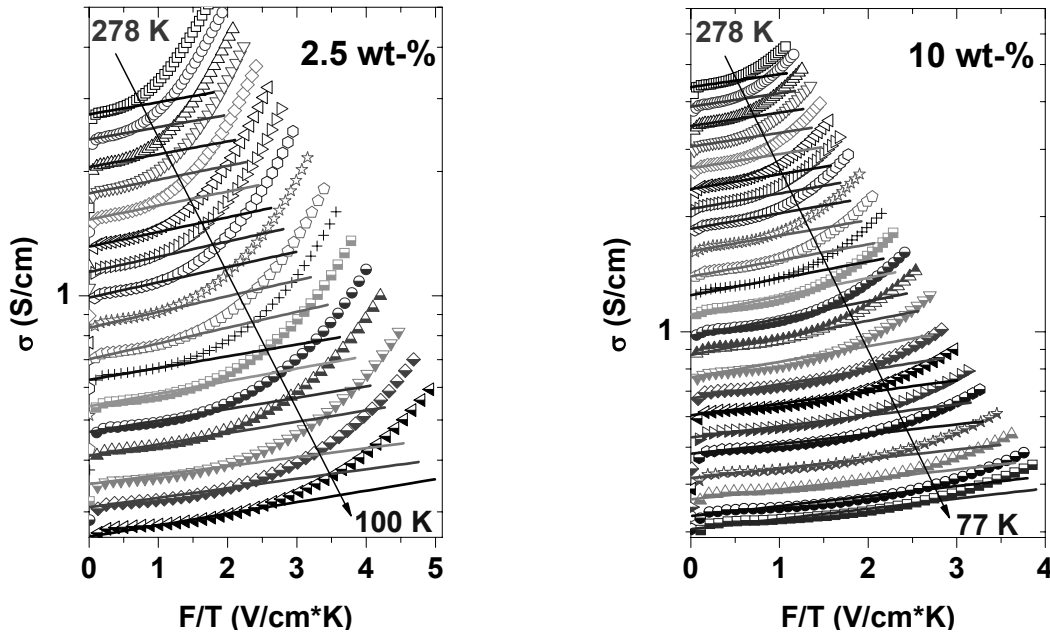


Figure 7.2: Conductivity as a function of F/T for PEDOT:PSS thin films with 2.5 wt-% and 10 wt-% of sorbitol added to the aqueous dispersion used for spin coating of the films at different temperatures. Solid lines are fits to Eq. 7.3.

At each temperature in Figure 7.2, the data are fitted quite well by Eq. 7.3 at low to moderate electric field. Deviations from straight lines in Figure 7.2 indicate the onset of another conduction mechanism at high electric field, which is beyond the scope of the present work. As the temperature is changed, the slope of the lines through the data in Figure 7.2 also changes. The temperature dependence of the hopping length $L(T)$ extracted from the slopes of Figure 7.2 is

shown in Figure 7.3. For both samples, the hopping length increases with decreasing temperature and reaches a maximum at a critical temperature T_{C1} , 145 K and 130 K for 2.5 wt-% and 10 wt-% samples, respectively. After T_{C1} , a sudden decrease in the hopping length is observed and the values of L reach a second critical temperature T_{C2} after which they seem to saturate or even start rising again. The inset of Figure 7.3 shows the analysis of the power exponent α in Eq. 7.1 for temperatures below T_{C1} . Although we previously found an excellent correspondence with $\alpha = 1/2$ for the whole temperature range in Figure 7.1, α is found to be less than $1/2$ for the specific range below T_{C1} . We shall further discuss this behavior in the discussion section.

The characteristic hopping length in 1D-VRH is expected to vary as $T^{-1/2}$ according to [27]

$$L(T) = \frac{\xi'}{2} \left(\frac{T_0}{T} \right)^{\frac{1}{2}} \quad \text{Eq 7.4}$$

which is used to extract ξ' from the measured samples in Figure 7.3. Good agreement between Eq. 7.4 and the data in Figure 7.3 is obtained in the range where L continuously increases, and the extracted ξ' values are shown in Table 7.I. They are found to be about a factor 5 larger than that of pristine samples (8.2 nm)[36]. Next, from T_0 and ξ' we have calculated the 1D density of states $N(E_F)$ using Eq. 7.2, and found 4.2×10^6 and 4.6×10^6 eV⁻¹cm⁻¹ for 2.5 and 10 wt-%, respectively. By using the width (30-40 nm, respectively) and thickness (6-7 nm) of the 1D channels (see next section) these numbers can be transformed into an estimate for the 3D density of states, see Table 7.I.

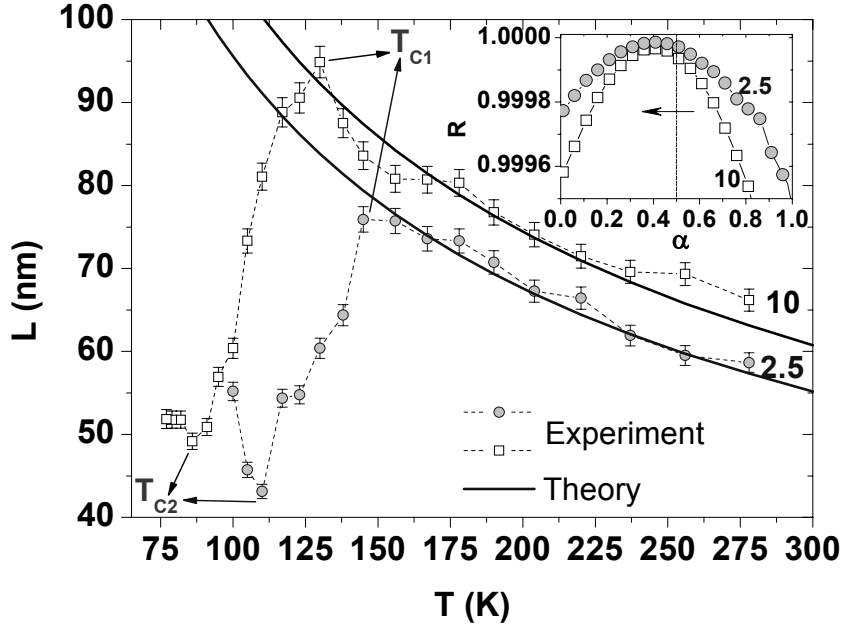


Figure 7.3: Temperature dependence of the characteristic hopping length for PEDOT:PSS thin films with (○) 2.5 wt-% and (□) 10 wt-% of sorbitol added to the aqueous dispersion used for depositing the layers. The dashed lines connect the data points, the solid lines are fits to Eq. 7.4. The inset shows the analysis of the power exponent α in Eq. 7.1 for temperatures below T_{C1} , i.e. the correlation coefficient R to the fit of Eq. 7.1 is plotted versus α . A vertical dashed line at $\alpha = 1/2$, clearly shows the shift of the best-fitting value of α to lower values, in this case $\alpha_{2.5 \text{ wt-\%}} = 0.40 \pm 0.02$ and $\alpha_{10 \text{ wt-\%}} = 0.39 \pm 0.03$.

While the results in Figure 7.3 corroborate our identification of quasi 1D-VRH as the transport mechanism around room temperature, the behavior at $T < T_{C1}$, requires an alternative interpretation. The Efros-Shklovskii or Coulomb gap model should be relevant only at low temperatures, i.e. the thermal energy should be smaller than the width of the Coulomb gap, i.e. $k_B T < \delta$. Ignoring any anisotropy, δ can be estimated as $\delta \approx \sqrt{N(E_F) e^6 / (4\pi\epsilon_0\epsilon_r)^3}$ [7,40]. By taking $N(E_F) \sim 10^{18} \text{ eV}^{-1}\text{cm}^{-3}$ and assuming $\epsilon_r = 3$, δ is roughly 10 meV or 120 K, which is very close to the observed values of T_{C1} . Hence, the discontinuity in $L(T)$ at T_{C1} can tentatively be attributed to a transition to another transport regime, governed by the opening of a Coulomb gap. At T_{C2} the transition appears to have completed. Depending on the details of the system, the associated temperature exponent α can theoretically expected to be $1/2$ [7,40] or $2/5$ [37]. The experimentally extracted values for α below T_{C1} closely match the latter number; it is however not clear whether the theory in Ref. 37 can directly be applied to the present granular system. In addition, the remaining temperature range below T_{C2} is too

small to extract a value for α with any accuracy and we refrain from a further analysis of the low temperature data.

7.3.2 Morphology

The interpretation of the charge transport data of sorbitol-treated PEDOT:PSS thin films in terms of a quasi 1D-VRH model is striking in view of the fact that charge transport in pristine films of the same material is governed by 3D-VRH, i.e. $\alpha = 1/4$ in Eq 7.1 [36,38] (see Chapters 3 and 4). This transition can however be readily understood from changes in the film morphology as seen by low-current STM, see Figure 7.4. Clearly, for the sample made without adding sorbitol (referred to as 0 wt-%), the 20-25 nm sized PEDOT-rich particles are (almost) randomly distributed. Upon adding sorbitol to the aqueous dispersions used for spin coating, these particles arrange spontaneously along lines that, for the image size shown, all run in a preferential direction. It seems logical to assume that the particles are more strongly coupled, i.e. are separated by a thinner PSS barrier, along these lines than perpendicular to these lines. This assumption directly explains the quasi 1D behavior of the sorbitol treated samples. Actually, this morphology seems to be a perfect example of ‘a large number of parallel chains of finite length’ that was considered in Ref. 27.

Despite the strong particle alignment in sorbitol-enhanced films and the fact that such alignment is found everywhere on the sample, no preferential orientation direction could be observed on length scales above $\sim 1 \mu\text{m}$. Due to the random orientation of these ordered domains, the macroscopic in-plane conductivity is most likely isotropic [39]. Since the typical domain size is at least one order of magnitude bigger than the characteristic hopping length, one may anticipate that the macroscopic conductivity is limited by the intra-domain conduction, leading to the observed quasi 1D behavior.

Another effect of the addition of sorbitol is an increase in size of the PEDOT-rich particles. Going from the pristine PEDOT:PSS sample, Figure 7.4(a), to 10 wt-% sorbitol, Figure 7.4(c), the particle diameter increases from 20-25 nm to about 40 nm in average. Qualitatively, an increased particle size may be expected to result in a reduced density of states. However, the density of states $N(E_F)$ of the present samples is about an order of magnitude higher than the

value of $1.4 \times 10^{17} \text{ eV}^{-1}\text{cm}^{-3}$ found for pristine films [36]. This behavior is tentatively attribute to a narrowing of the density of states resulting from reduced disorder in the sorbitol treated films. In addition, batch-to-batch variations, which can amount up to a factor two or so in T_0 , may play a role.

The size of the PEDOT-rich particles is fully consistent with the observed, rather large, hopping length L in Figure 7.3. This implies that the conduction in sorbitol-treated PEDOT:PSS, like in the pristine material [36], takes place by hopping of charge carriers between PEDOT-rich particles, rather than between single molecular sites.

To complete the morphological picture, we performed cross-sectional phase-imaging AFM (X-AFM) on cryogenically cleaved sorbitol treated films. This technique was previously shown in Chapter 3 to allow the visualization of PEDOT-rich and PSS-rich regions because of differences in visco-elastic properties [38]. In Figure 7.5 it can be seen that in the vertical direction the sorbitol treated film consists of flattened dark areas (blue color), which we interpret as the PEDOT-rich domains, separated by quasi continuous bright areas (yellow color), interpreted as PSS lamellas. The typical in-plane size of the PEDOT-rich particles is of the same order as that of the spherical objects in Figure 7.4(b), consistent with the interpretation of these as the PEDOT-rich clusters. This lamellar morphology is very similar to the one observed in our previous work for pristine films [38] shown in Chapter 3. Apparently, the sorbitol-facilitated reorganization of PEDOT and PSS does not significantly affect the phase separation in the vertical direction.

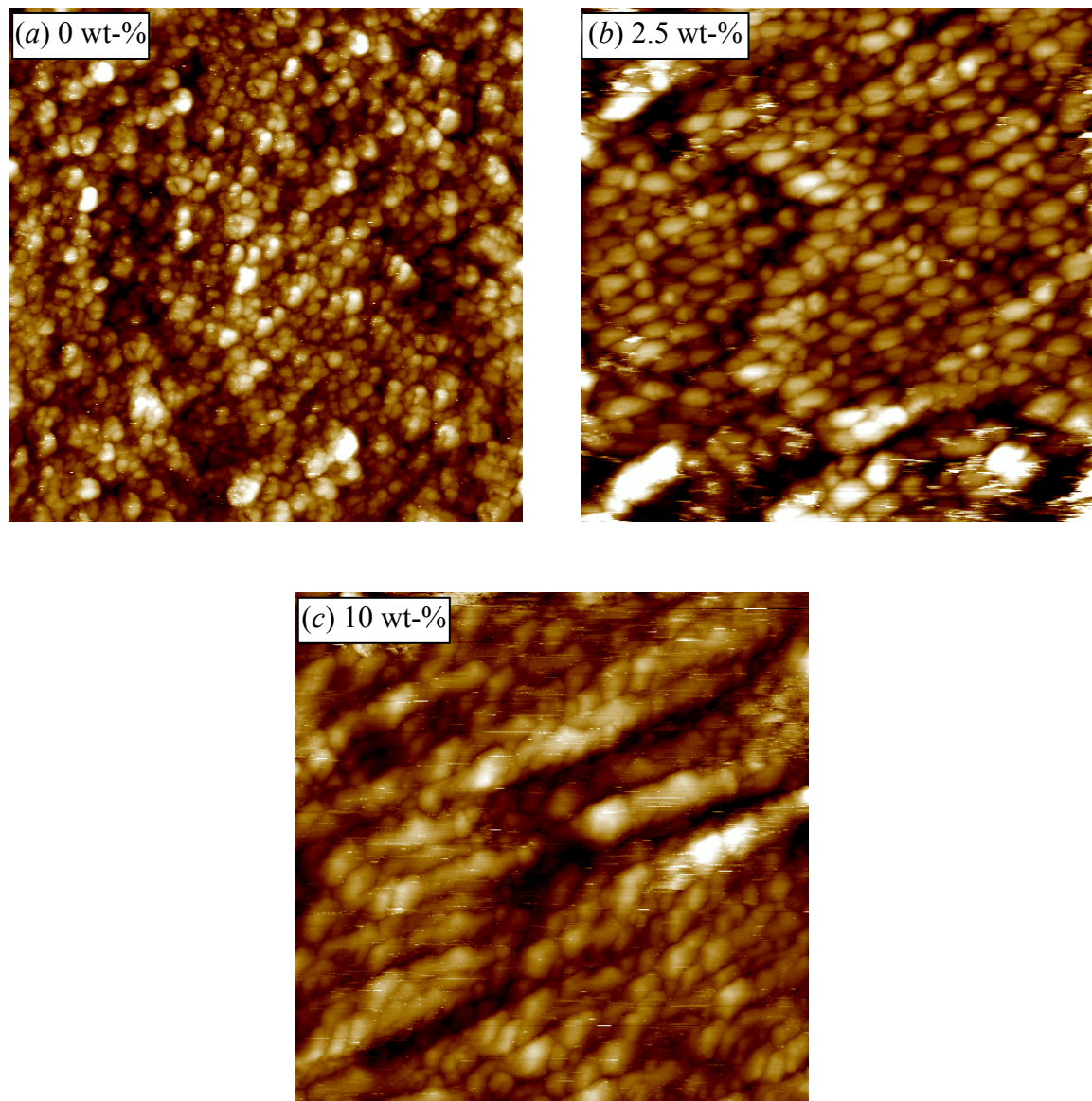


Figure 7.4. Topographic STM images of PEDOT:PSS spin coated on ITO with different sorbitol concentration in the aqueous dispersion: (a) 0 wt-% (pristine) [bias: 2.3 V; $I_{\text{tunneling}}$: 20 pA], (b) 2.5 wt-% [bias: 0.1 V; $I_{\text{tunneling}}$: 10 pA], and (c) 10 wt-% [bias: 0.5V; $I_{\text{tunneling}}$: 0.5 pA]. All images were captured in areas of $500 \times 500 \text{ nm}^2$ and vertical scale of 10 nm. The 20-40 nm sized bright objects and the thin depressions are interpreted as PEDOT-rich particles and separating PSS barriers, respectively [38].

7.4 Discussions

Comparing the values of the effective localization length ξ' for sorbitol samples (30-45 nm, see Table 7.1) and that found for pristine material (8 nm, Ref.

36), we observe an increase of about a factor 4-5. In a granular material the use of an effective localization length, rather than of the normal one, reflects the fact that the wave function only picks up a significant ‘tunneling action’ in the separating barriers, i.e. in the PSS. Hence, ξ' and ξ are related via $\xi' = \xi(d + s)/s$ with d and s the particle diameter and barrier thickness, respectively [40]. The observed increase of ξ' upon including sorbitol in film formation is most likely due to a decrease in s , since d increases only slightly. The decrease in s is consistent with a better mixing of PEDOT and PSS due to the plasticizing action of sorbitol. Moreover, a reduced inter-particle tunneling barrier width s explains the large increase in conductivity upon (increasing) sorbitol treatment.

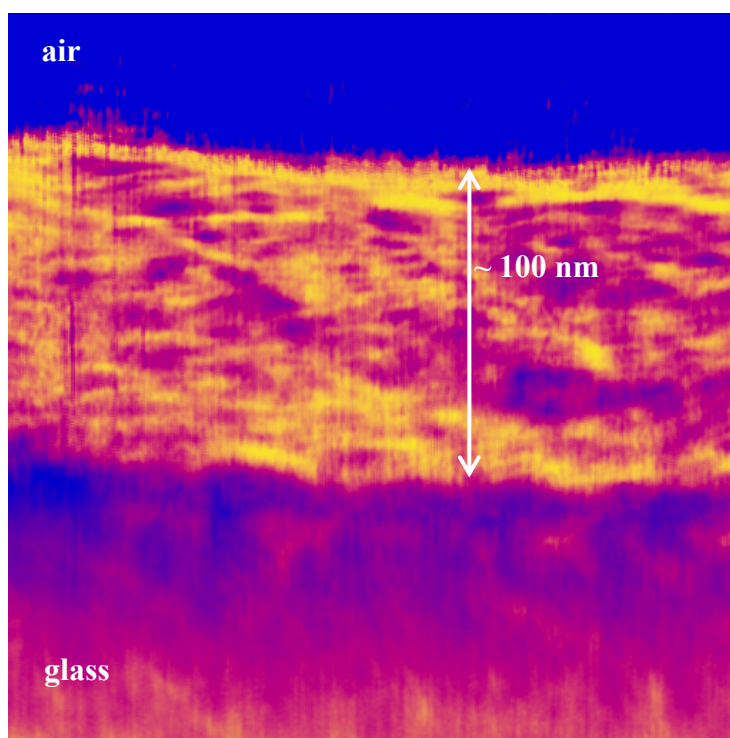


Figure 7.5: $250 \times 250 \text{ nm}^2$ cross-sectional AFM phase image of cleaved PEDOT:PSS deposited on glass from an aqueous dispersion containing 2.5 wt-% sorbitol. Vertical scale is 30° . Bright (yellow) and dark (blue) areas in the PEDOT:PSS film are interpreted as PSS lamellas and PEDOT-rich particles, respectively [38].

7.5 Conclusions

We have studied the conductivity of PEDOT:PSS thin films deposited by spin coating from aqueous dispersions containing a high-boiling solvent (sorbitol). We found that the well-known conductivity enhancement by several orders of magnitude is accompanied by a transition from 3D variable-range hopping to quasi 1D-VRH. Using scanning probe microscopy, the latter effect could be explained by a sorbitol-induced self-organization of the PEDOT-rich grains into 1D aggregates between which hopping of charge carriers takes place. Although these aggregates are aligned within (sub) micrometer sized domains, these domains seem to have no preferential orientation, i.e. no macroscopic in-plane anisotropy is present. The typical hopping distance of 60-90 nm, which is extracted from non-Ohmic transport, matches well with hopping between 30-40 nm sized grains. Combining these results, the sorbitol-induced conductivity increase could be attributed to a decrease in thickness of the PSS barrier separating the PEDOT-rich grains.

7.6 References and notes

- [1] F. P. Wenzl, P. Pachler, C. Suess, A. Haase, E. J. W. List, P. Poelt, D. Somitsch, P. Knoll, U. Scherf, G. Leising, *Adv. Funct. Mater.* **2004**, *14*, 441.
- [2] B. J. Schwartz, *Ann. Rev. Phys. Chem.* **2003**, *54*, 141.
- [3] R. Kline, M. McGehee, *Polym. Rev.* **2006**, *46*, 27.
- [4] H. Hoppe, N. S. Sariciftci, *J. Mater. Chem.* **2006**, *16*, 45.
- [5] V. I. Arkhipov, I. I.; Fishchuk, A. Kadashchuk, H. Bäessler, In *Photophysics of Molecular Materials: From Single Molecules to Single Crystals*, G. Lanzani (Ed.) Wiley-VCH, **2006**, p 261-366.
- [6] N. Mott, E. A. Davis, *Electronic Processes in Non-Crystalline Materials*, Clarendon Press, Oxford, **1979**.
- [7] B. I. Shklovskii, A. L. Efros, *Electronic Properties of Disordered Semiconductors*, Springer, Berlin, **1984**.
- [8] F. Jonas, A. Karbach, B. Muys, E. van Thillo, R. Wehrmann, A. Elschner, R. Dujardin, *European Patent EP 686662*, **1995**.
- [9] L. A. A. Pettersson, S. Ghosh, O. Inganäs, *Organ. Electron.* **2002**, *3*, 143.
- [10] J. Y. Kim, J. H. Jung, D. E. Lee, J. Joo, *Synth. Met.* **2002**, *126*, 311.
- [11] F. J. Touwslager, N. P. Willard, D. M. de Leeuw, *Synth. Met.* **2003**, *135–136*, 53.
- [12] F. Louwet, L. Groenendaal, J. Dhaen, J. Manca, J. Van Luppen, E. Verdonck, L. Leenders, *Synth. Met.* **2003**, *135–136*, 115.
- [13] M. Döbbelin, R. Marcilla, M. Salsamendi, C. Pozo-Gonzalo, P. M. Carrasco, J. A. Pomposo, D. Mecerreyes, *Chem. Mater.* **2007**, *19*, 2147.
- [14] F. Zhang, M. Johansson, M. R. Andersson, J. C. Hummelen, O. Inganäs, *Adv. Mater.* **2002**, *14*, 662.
- [15] H. J. Snaith, H. Kenrick, M. Chiesa, R. H. Friend, *Polymer* **2005**, *46*, 2573.
- [16] A. J. Mäkinen, I. G. Hill, R. Shashidhar, N. Nikolov, Z. H. Kafafi, *Appl. Phys. Lett.* **2001**, *79*, 557.
- [17] W. H. Kim, A. J. Mäkinen, N. Nikolov, R. Shashidhar, H. Kim, Z. H. Kafafi, *Appl. Phys. Lett.* **2002**, *80*, 3844.
- [18] X. Crispin, F. L. E. Jakobsson, A. Crispin, P. C. M. Grim, P. Anderson, A. Volodin, C. van Haesendonck, M. Van der Auweraer, W. R. Salaneck, M. Berggren, *Chem. Mater.* **2006**, *18*, 4354.
- [19] J. Ouyang, Y. Yang, *Adv. Mater.* **2006**, *18*, 2141.
- [20] B. Yoo, A. Dodabalapur, D. C. Lee, T. Hanrath, B. A. Korgel *Appl. Phys. Lett.* **2007**, *90*, 072106.
- [21] B. Chen, T. Cui, Y. Liu, K. Varahramyan, *Solid-State Electron.* **2003**, *47*, 841.
- [22] J. Ouyang, C.-W. Chu, F.-C. Chen, Q. Xu, Y. Yang, *Adv. Funct. Mater.* **2005**, *15*, 203.

- [23] S. K. M. Jönsson, J. Birgersson, X. Crispin, G. Greczynski, W. Osikowicz, A. W. Denier van der Gon, W. R. Salaneck, M. Fahlman, *Synth. Met.* **2003**, 139, 1
- [24] S. Timpanaro, M. Kemerink, F. J. Touwslager, M. M. de Kok, S. Schrader, *Chem. Phys. Lett.* **2004**, 394, 339-343.
- [25] S. K. M. Jönsson, W. R. Salaneck, M. Fahlman, *J. Electron Spectrosc., Relat. Phenom.* **2004**, 137-140, 805-809.
- [26] J. Huang, P. F. Miller, J. S. Wilson, A. J. de Mello, J. C. de Mello, D. D. C. Bradley, *Adv. Funct. Mater.* **2005**, 15, 290.
- [27] V. K. S. Shante, C. M. Varma, A. N. Bloch, *Phys. Rev. B* **1973**, 8, 4885.
- [28] P. Sheng, B. Abeles, Y. Arie, *Phys. Rev. Lett.* **1973**, 3, 44.
- [29] P. Sheng, *Phys. Rev. B* **1980**, 21, 2180.
- [30] L. Zuppiroli, M. N. Bussac, S. Paschen, O. Chauvet, L. Forro, *Phys. Rev. B* **1994**, 50, 5196.
- [31] J. Ouyang, Q. Xu, C. W. Chu, Y. Yang, G. Li, J. Shinar, *Polymer* **2004**, 45, 8443.
- [32] S. Ashizawa, R. Horikawa, H. Okuzaki, *Synth. Met.* **2005**, 153, 5.
- [33] X. Crispin, S. Marciniak, W. Osikowicz, G. Zotti, A. W. Denier van der Gon, F. Louwet, M. Fahlman, L. Groenendaal, F. de Schryver, W. R. Salaneck, *J. Polym. Sci B* **2003**, 41, 2561.
- [34] R. M. Hill, *Philos. Mag.* **1971**, 24, 1307.
- [35] M. Pollak, I. Riess, *J. Phys. C* **1976**, 9, 2339.
- [36] A. M. Nardes, M. Kemerink, R. A. J. Janssen, *Phys Rev. B.* **2007**, 76, 085208.
- [37] M. M. Fogler, S. Teber, B. I. Shklovskii, *Phys. Rev. B* **2004**, 69, 035413.
- [38] A. M. Nardes, M. Kemerink, R. A. J. Janssen, J. A. M. Bastiaansen, N. M. M. Kiggen, B. M. W. Langeveld, A. J. J. M. van Breemen, M. M. de Kok, *Adv. Mater.* **2007**, 19, 1196.
- [39] A possible anisotropy in conductivity was not explicitly investigated, but the excellent sample-to-sample reproducibility suggests that if macroscopic anisotropy is present, its net magnitude is very small.
- [40] J. Zhang, B. I. Shklovskii, *Phys. Rev. B* **2004**, 70, 115317.

Modulated-differential scanning calorimetry and direct insert probe mass spectrometry

Modulated-Differential Scanning Calorimetry (MDSC) and Direct Insert Probe Mass Spectrometry (DIP-MS) were used as auxiliary tools to understand the influence that temperature has on pristine PEDOT:PSS and PEDOT:PSS treated with sorbitol. From the analysis and discussion we conclude that the optimal annealing temperature (200 °C) and time (2 min) is enough to remove both water and sorbitol.

A1.1 Introduction: Modulated-differential scanning calorimetry (MDSC)

In comparison to conventional DSC, modulated DSCⁱⁱ has a much higher resolution and since it uses a sinusoidal perturbation on top of the linear rise in temperature. Once the total heat flow and change in heat capacity are acquired, a Fourier Transform treatment allows differentiation of the reversing and non-reversing heat flow. The reversing signal is sensitive to phase transitions like the glass transition, whereas e.g. evaporation shows up in the non-reversing signal.

A1.2 Experimental

MDSC analyses were conducted at *Philips Research Laboratories*, in Eindhoven, by Dr. M. M. de Kok using a TA Instruments model MDSC Q1000. The commercial aqueous solution of PEDOT:PSS (H. C. Starck trade name Baytron P) in its pristine (pure) form and mixed with 5 wt-% sorbitol were examined. Few drops of the solutions were deposited into the MDSC pan and dried under ambient conditions. The lids of the pans were perforated to allow the remaining water to evaporate from sample and to avoid pressure increase inside the pan. The pan is placed inside the oven, which is flushed with dry N₂ and heated according to input programming. The general procedure was to cool down the samples to -10 °C and then heated at 200 °C at a rate of 10 °C/min. This procedure was repeated several times and the temperature raise was modulated by ± 1 °C every 30 s.

A1.3 Results and discussions

Pristine PEDOT:PSS. The total heat flow and the derived reversing and non-reversing heat flow were measured and shown in Figure A1(a). In the first heating step, a decrease of the total and non-reversing heat flow with a minimum around 75 °C was observed. This effect is attributed to the evaporation of water

ⁱⁱ A) M. Reading, D. Elliott, V. L. Hill, *Therm. Anal.* 1993, 40, 931; B) S. R. Sauerbrunn, B. S. Crowe, M. Reading, *Polym. Mater. Sci. Eng* 1993, 68, 269; C) S. R. Syerbrunne, M. Reading, *J. Therm. Anal.* 1993, 40, 949.

that is completed upon reaching 200 °C. The absence of this feature in the following cycles corroborates this assignment.

PEDOT:PSS mixed with 5 wt-% sorbitol. The first heating run showed two non-reversing maxima around 100 °C and 160 °C, as observed in Figure A1(b). In contrast, in the pristine PEDOT:PSS only a single non-reversing effect was found around 75 °C. The melting point of pure sorbitol is ~ 95 °C thus the first feature could be related to melting of sorbitol or, again, to the evaporation of water. The origin of the second phase is not clear in detail, but, given its absence in consecutive cycles, most likely related to the evaporation of sorbitol.

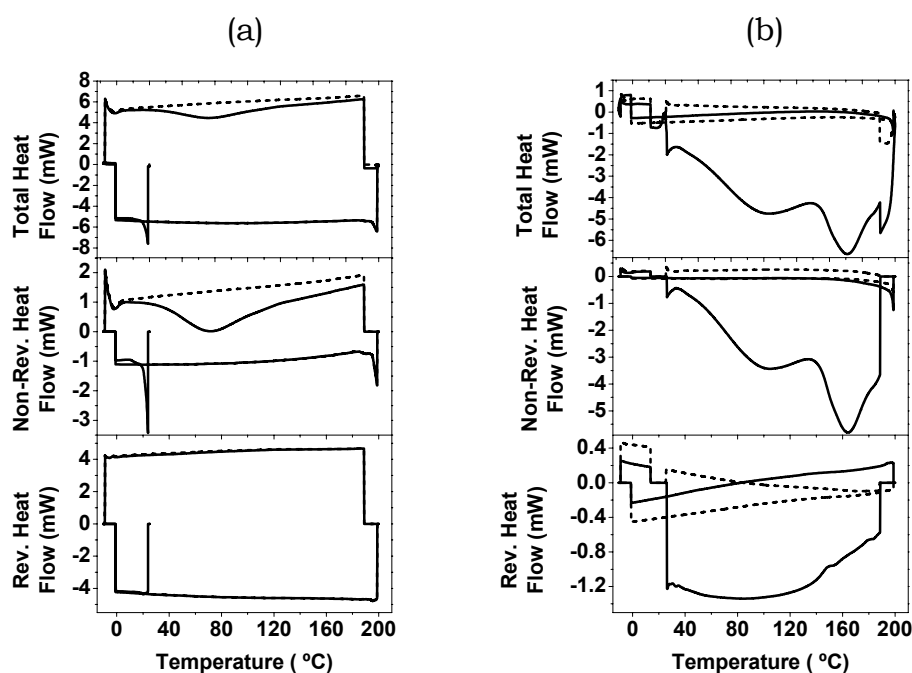


Figure A1: MDSC on (a) pristine PEDOT:PSS and PEDOT:PSS mixed with 5 wt-% of sorbitol. Full and dashed are the 1st and 2nd heating steps, respectively.

A1.4 Conclusions

A non-reversing effect in the temperature range of 50 °C to 100 °C is visible when air-dried PEDOT:PSS is heated to 200 °C. This effect is most likely related to the water evaporation from samples as in consecutive runs this effect is no longer present. When PEDOT:PSS is mixed with sorbitol (5 wt-%) the removal of sorbitol and water is observed in two phases in the temperature ranges of 50 °C – 140 °C and 150 °C – 200 °C. We note that these peaks coincide with DIP-MS experiments shown below.

A2.1 Introduction: Direct insert probe mass spectrometry (DIP-MS)

In order to perform DIP-MS, PEDOT:PSS is deposited from solution into a quartz-microtube in contact with a heating probe which is inserted in the mass spectrometer (MS). During heating, which is performed in high vacuum, it is possible to analyze in real time by mass spectrometry (MS) the products that are set free at the applied temperature. As such, DIP-MS is a very sensitive technique and complementary to TGA and MDSC.

A2.2 Experimental

DIP-MS analyses were carried out using a Shimadzu chromatograph, model GCMS – QP5000 with the assistance of Dr. X. Lou and Mr. J. L. J. van Dongen at the Chemistry Department of the TU/e. Also here, the commercial PEDOT:PSS in its pristine form and with different sorbitol concentrations, 2.5, 5 and 10 wt-%, were measured. All samples were deposited into a quartz microtube, about 1–2 μL , and dried in ambient. For comparison, sorbitol diluted in methanol was also prepared and a blank sample was used as reference. The quartz microtube containing the sample was connected to the heating probe and subsequently inserted into the high vacuum (10^{-6} mbar) chamber for the MS analysis.

A2.3 Results and discussions

The peaks of the relative total ion current (TIC), which is the sum of all mass fragments, as a function of temperature are shown for samples with added sorbitol in Figure A2(a). The 2.5 wt-% sample shows one maximum, with a broadened shoulder that develops into a second maximum at higher sorbitol concentrations. The relative TIC of this sample clearly shows that most evaporation occurs before 200 °C.

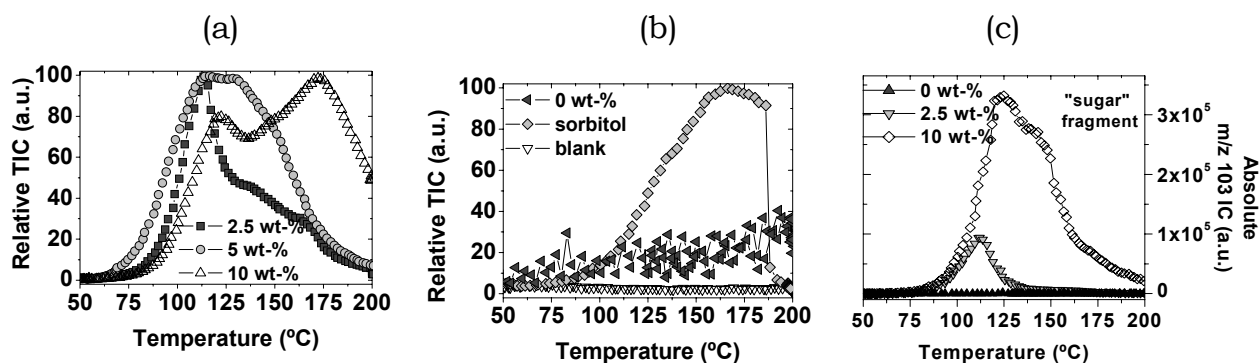


Figure A2: First run of DIP-MS: temperature and relative total ion current (TIC) signal as a function of time for PEDOT:PSS samples with (a) different sorbitol concentration, 2.5, 5 and 10 wt-%; (b) 0 wt-%, pure sorbitol and a blank sample; (c) Absolute m/z 103 ion current ("sugar" fragment) versus temperature. The temperature profile follows a ramp of 10 °C/min up to 200 °C, at 200 °C temperature is kept constant for 2 min and then allowed to cool down.

The pristine (0 wt-%) PEDOT:PSS, Figure A2(b), showed a broadened noise peak, which increases up till 200 °C. The major contributions to this peak are the fragments m/z 32, 44 and 64. The first two fragments are due to O_2 and CO_2 present in air, also observed in the blank sample. The last one is attributed to an SO_2 fragment coming from the PSS. From the two polymers, PSS is most susceptible to degradationⁱⁱⁱ. However, the extremely low intensity of this signal is consistent with the observation that no degradation in the electrical performance occurs upon heating to 200 °C (see Chapter 5).

Figure A2(c) monitors the ion current (IC) of m/z 103, the most relevant fragment in the present investigation, which is related to a sugar fragment coming from the sorbitol. It observed that in the case of sorbitol-added samples the m/z 103 fragment is dominant in the first peak in Figure A2(a) and its magnitude scales with the amount of sorbitol added. The second peak in Figure A2(a), which roughly coincides with the feature at 170 °C observed above in MDSC, consists of multiple, smaller fragments, indicating further decomposition of the sorbitol. Of these, the fragments m/z 57, 69 and 86 are the most intense. The absence of a peak at 75 °C, where a peak is found in MDSC, is consistent with the identification of that peak to evaporation of water, since H_2O is too light to be detected in DIP-MS.

After the first run, each sample was allowed to cool down in vacuum and a second round of measurements was conducted. The same temperature profile

ⁱⁱⁱ M. M. de Kok, *unpublished results*

was employed again. These measurements (not shown) revealed minor traces of the remaining sorbitol, very close to noise level. Therefore, we conclude that basically all the sorbitol is removed in the first annealing step (200 °C, 2 min). Since these analyses are performed on ‘bulk’ samples, we expect the same annealing step to completely remove sorbitol from a ~ 100 nm thick film.

A2.4 Conclusions

It was found from DIP-MS that sorbitol completely evaporates when sample is heated to 200 °C for 2 min, and that no further degradation occurs at this temperature. The characteristic temperatures at which evaporation is observed during DIP-MS are consistent with those found in MDSC. Evaporation of solvents in sorbitol-treated samples occurs in two steps, the first, around 75 °C, is most likely related to water, the latter, around 175 °C, is related to sorbitol.

Curriculum Vitae

Alexandre Mantovani Nardes is a native Brazilian from the city of São Paulo. His primary education was conducted at Colégio Vicente Pallotti when he finished in 1991 and the secondary education at Oswaldo Cruz Technical High School where he got an associate degree in electronics in 1995. After about 2 years working as Electronic Technician, he started his University studies at the São Paulo Faculty of Technology (Fatec-SP, MPCE, BSc in Microelectronics) and at the Polytechnic School of the University of São Paulo (USP). At USP, he got his MSc degree in Electrical Engineering by his work on electrical properties of hydrogenated microcrystalline silicon thin films deposited via PECVD technique at low temperatures, in May 2002. In the same year, in August, he started his PhD project at USP in the field of organic electronics. In September 2004, he moved to the department of Applied Physics at the Eindhoven University of Technology (TU/e) to continue his PhD work under a double-diploma agreement between the two Universities. The main results of his research are described in this thesis.

List of Publications:

A. M. Nardes, E. A. T. Dirani, R. F. Bianchi, J. A. R. Neves, A. M. Andrade, R. M. Faria and F. J. Fonseca, "*Barrier coating for polymer light-emitting diodes using carbon nitride thin films deposited at low temperature by PECVD technique*", **Materials Science and Engineering C** 2004, **24**, 607–610.

A. M. Nardes, M. Kemerink, R. A. J. Janssen, J. A. M. Bastiaansen, N. M. M. Kiggen, B. M. W. Langeveld, A. J. J. M. van Breemen, and M. M. de Kok, "*Microscopic Understanding of the Anisotropic Conductivity of PEDOT:PSS Thin Films*", **Adv. Mater.** 2007, **19**, 1196–1200.

A. M. Nardes, M. Kemerink, R. A. J. Janssen, “Anisotropic hopping conduction in spin coated PEDOT:PSS thin films”, **Phys. Rev. B** **2007**, **76**, **085208-1**.

A. M. Nardes, M. Kemerink, R. A. J. Janssen, “A morphological model describing the solvent-induced conductivity enhancement in PEDOT:PSS thin films”, **Submitted for publication**.

A. M. Nardes, M. Kemerink, M. M. de Kok, E. Vinken, K. Maturova, R. A. J. Janssen, “Conductivity, environmental stability and work function of PEDOT:PSS thin films treated with sorbitol”, **Submitted for publication**.

Acknowledgments

My name appearing alone on the cover of this thesis does not reflect the enormous contributions of a lot of individuals, both directly and indirectly, to the very existence of it.

Chronologically, my PhD project started back in 2002, in São Paulo, Brazil, at the Polytechnic School of the University of Sao Paulo (USP), and thanks to a lot of people there I became involved with the field of organic electronics. I would like to start by thanking my Brazilian supervisor, Prof. Adnei Melges de Andrade, who accepted me as his Ph.D. student without any hesitation. Thereafter, he offered me so much advice, freedom in my work and at the same time guiding me in the right direction. Thank you very much for all the support you gave during my time at USP and abroad.

I also would like to thank Prof. Ely Antonio Tadeu Dirani, who taught me basically all the basis for a research carrier during my MSc project, and most important, I learnt from you that hard work always pays off. It has been always a pleasure to work together with you.

My gratitude goes also to Prof. Fernando Josepetti Fonseca, for all the support on my projects in Brazil and abroad, for the friendship, and for the great enthusiasm.

I have to thank Prof. Rodrigo Bianchi for the help to write the PhD proposal. At that time, the proposal was a challenge and a huge encouragement for a laboratory that had not too much experience with organic devices. I would like to thank you for the support, to teaching me the basics of organic electronics, and for the optimistic point of view that everything is possible.

Thanks also to the colleagues I made in the *grupo de Eletrônica Molecular* (GEM) of the *Laboratório de Microeletrônica* (LME): Prof. Roberto Onmori, Prof.

José Augusto, Dr. Carlos Alberto dos Santos Ramos, José Antonio Rocha das Neves, Emerson Roberto dos Santos, John Paul Hempel Lima, Gerson dos Santos, João dos Santos, Fábio Henrique Pimentel, Helena Libertori Gimaiel, Murilo dos Santos, Juliana Okagawa, Reinaldo Gomes da Silva, Dr. Leonardo Patterno, and Guilherme Braga. I thank you all for the friendship and great work environment during my time at USP. I have also to thank Dr. Edison Motta of GNMD group for his help and discussions about carbon nitride thin films.

Well, 2 years after I started my PhD in Brazil, I was granted with a scholarship by the European Union, the Alþan program, and arrived Eindhoven in the summer of 2004 to continue the project at the Eindhoven University of Technology (TU/e), in the Netherlands.

In the Netherlands, firstly, I would like to thank Prof. Hidde Brongersma, who was my first contact in Eindhoven while I was still looking for an European laboratory to support my Ph.D. project. I am also very grateful to Dr. Arnoud Denier van der Gon, who deceased before my start in Eindhoven, and supposed to supervise me. He had a great influence on the success and approval of my project proposal.

Life has to move on, and I am very proud and lucky to have Prof. René Janssen as my Dutch supervisor. I would like to thank you, René, for all your support since the beginning, for your patience, the freedom you gave me, the opportunity to travel far away to attend conferences, for making me part of the *Molecular Materials and Nanosystems (M2N) group*, and for financially supplementing my scholarship.

Before I met Dr. Martijn Kemerink I thought that research on fundamental issues was somewhat boring and sometimes useless. But, after spending all those years working together my opinion has changed. Martijn, my co-supervisor, trained me well as a researcher and gave me the opportunity to make an impact in the scientific community at large. This thesis would not be like it is, if it wasn't for your careful guidance. You kept my focus and always found some light in the darkness of my results and queries. I learned a lot from you and enjoyed our collaboration. I really appreciated this and I thank you for the teaching, the endless support, the optimistic point of view and the encouragement that I received until the end.

Dr. Margreet de Kok, from Philips Research Laboratories, has contributed to a great extent directly to some studies presented here. It has been an absolute pleasure and honor to have you as a co-author in my papers.

From TNO, I thank Dr. Albert van Breemen, Ms. Nicole Kiggen, Dr. Bea Langeveld, and Ms. Jolanda Bastiaansen for providing so many samples and materials.

From the Chemistry Department of the TU/e, I want to thank Mr. Joost van Dongen and Dr. Xianwen Lou for the assistance with the DIP-MS measurements, and Mrs. Esther Vinken for the TGA measurements.

Sometimes, things simply don't work out like as you expect. However, I really appreciated the enormous efforts of: Mrs. Svetlana van Bavel and Dr. Joachim Loos (Chemistry Dept. of the TU/e) for the TEM measurements on my PEDOT:PSS samples; Dr. Marc Koetse and Mr. Peter Rensing (TNO) for the great time I had at TNO making and characterizing PLEDs; Mrs. Nicole Papen-Botterhuis (Chemistry Dept. of the TU/e) for the contact angle measurements on PEDOT:PSS.

For friendship, fun discussions of crazy ideas and camaraderie throughout my time at the TU/e I want to thank all the M2N group members in the Physics Department: Joris Halegaar, Jiri Cervenka, Rik Laarhoven, Nick Podaru, Ron Willems, Siebe van Mensfoort, Erwin Rossen, Kevin van de Ruit, Friso Wittebrood, Özlan Ipek, Klara Maturova (thanks for your great help with the SKPM, it is really good to work with somebody who knows exactly what she is doing), and the Calipso BV staff. Some past friends: Gheorghe Tanasa, Filipe Pinheiro, Hans Gommans, Jan-Maarten Kramer, Juan Amir, Marzenna Schoutese-Brzezinska, Erwin Timmerman, Marta Fonrodona Turon, Liang Ying-Xin. Special thanks for the people in Spectrum 1.83: Dimitri Charrier, to whom I found a truly friend; Erik Roeling, always ready to give a hand no matter the issue (thanks a lot for your help with the cover of this thesis, the printing process and some other bureaucratic issues); (Prof.) Simon Mathijssen...I thank also Dr. Kees Flipse and Prof. Reinder Coehoorn for many stimulating discussions and helpful suggestions during the group meetings.

I also really appreciated the helpful hand of the skilled professionals of the M2N staff: Mr. Gerard Wijers, I thank you for your help in designing 'my' 4 point probe set-up and making numerous mechanical repairs. Mr. Wijnand Dijkstra, thank you for your assistance with Labview and so many electrical and electronic

repairs. Mr. Rein Rumphorst, thank you very much for your interest in my work, helpful suggestions, and friendship.

In the other side of the campus, in the Chemistry Department, I would like to thank some other M2N group members: Dr. Martijn Wienk, Frank Verbakel, Jan Gilot, Dirk Veldman, for the great help with the chemicals, glove boxes, materials and all the issues related to a chemistry laboratory. Thanks a lot guys!

This work would not be possible without the financial support of the research agencies. In Brazil, this work was supported by ‘*The State of São Paulo Research Foundation*’ (FAPESP) under contract number 02/11941-6 between 2002 and 2004. In the Netherlands, since August 2004 this work has been supported by the European Union High Level Scholarship Programme for Latin America, the ‘*Alban program*’ under contract number E03D19439BR.

Last but not least there are the people in my life who have continuously supported me over these many years. I want to thank my father for advice and support, and my mother for saving my sanity during my home sickness. Thanks to my big family, my two brothers, my girlfriend (and family). You all have supported me over these many years of academia and life experience, never questioning what is undoubtedly a curious career path. Thanks for being so understanding over the years as I have remained too poor and too busy to be in contact with everybody as much as I should and would like.

Sincerely,

Alexandre

Eindhoven, November 2007.

